NASA Technical Paper 2963

April 1990

Spanwise Measurements of Vertical Components of Atmospheric Turbulence

Robert K. Sleeper

NASA

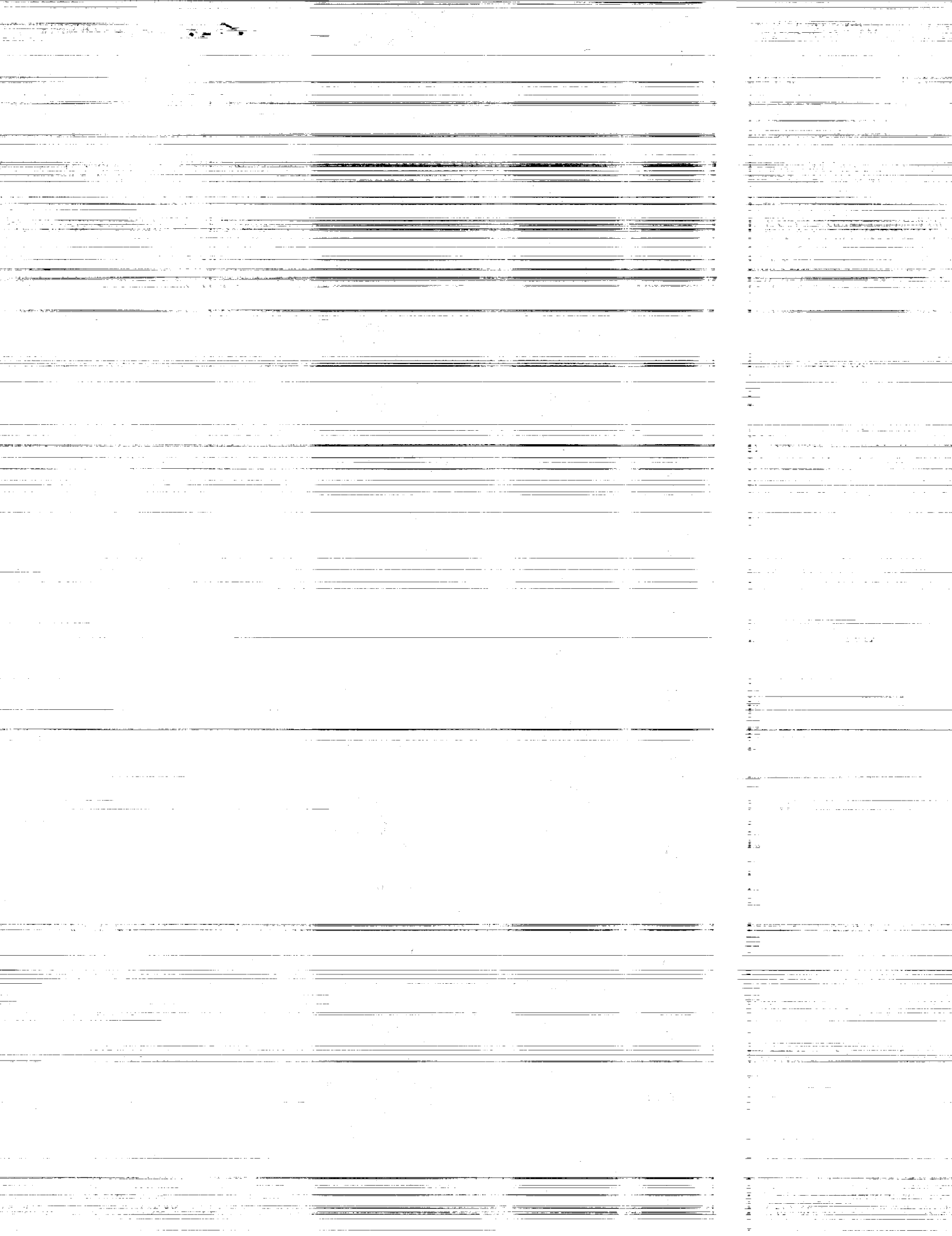

NASA Technical Paper 2963

1990

Spanwise Measurements of Vertical Components of Atmospheric Turbulence

Robert K. Sleeper
Langley Research Center
Hampton, Virginia

National Aeronautics and Space Administration
Office of Management
Scientific and Technical Information Division

Symbols

Values are given in both SI and U.S. Customary Units. The measurements and calculations were made in U.S. Customary Units.

a	speed of sound, m/sec (ft/sec)
b	wing span, m (ft)
c	acoustic velocity computation constant, 20.046333 m/sec-$K^{1/2}$ (65.76881 ft/sec-$K^{1/2}$)
f	frequency, Hz
L	integral scale length, m (ft)
N_l	number of correlation estimation time lags
N_p	number of data points in the record
p	static pressure, N/m^2 (lb/in^2)
$q_{c,C}$	impact pressure at center probe, N/m^2 (lb/in^2)
$q_{c,L}$	impact pressure at left probe, N/m^2 (lb/in^2)
$q_{c,R}$	impact pressure at right probe, N/m^2 (lb/in^2)
R_0^{CC}	no-lag auto-correlation estimate of center probe gust velocity or mean-square value, m^2/sec^2 (ft/sec^2)
R_{LC}^{CC}	auto-correlation estimate of center probe gust velocity for an equivalent lateral left-to-center probe lag distance, m^2/sec^2 (ft/sec^2)
R_{LR}^{CC}	auto-correlation estimate of center probe gust velocity for an equivalent lateral left-to-right probe lag distance, m^2/sec^2 (ft/sec^2)
R_0^{CR}	no-lag cross-correlation estimate of center and right probe gust velocities, m^2/sec^2 (ft/sec^2)
R_0^{LC}	no-lag cross-correlation estimate of left and center probe gust velocities, m^2/sec^2 (ft/sec^2)
R_0^{LL}	no-lag auto-correlation estimate of left probe gust velocity or mean-square value, m^2/sec^2 (ft/sec^2)
R_{LC}^{LL}	auto-correlation estimate of left probe gust velocity for an equivalent lateral left-to-center probe lag distance, m^2/sec^2 (ft/sec^2)
R_{LR}^{LL}	auto-correlation estimate of left probe gust velocity for an equivalent lateral left-to-right probe lag distance, m^2/sec^2 (ft/sec^2)
R_0^{LR}	no-lag cross-correlation estimate of left and right probe gust velocities, m^2/sec^2 (ft/sec^2)
R_0^{RR}	no-lag auto-correlation estimate of right probe gust velocity or mean-square value, m^2/sec^2 (ft/sec^2)
R_{LC}^{RR}	auto-correlation estimate of right probe gust velocity for an equivalent lateral left-to-center probe lag distance, m^2/sec^2 (ft/sec^2)
R_{LR}^{RR}	auto-correlation estimate of right probe gust velocity for an equivalent lateral left-to-right probe lag distance, m^2/sec^2 (ft/sec^2)

T_c	computed free-air temperature, K
t	time, sec
t_t	air total temperature, °C
s	spanwise separation distance between sensors, m (ft)
V, V_C	true airspeed at center probe, m/sec (ft/sec)
V_L	true airspeed at left probe, m/sec (ft/sec)
V_R	true airspeed at right probe, m/sec (ft/sec)
V_{az}	vertical aircraft velocity obtained from integration of vertical acceleration, m/sec (ft/sec)
$w_{g,C}$	measured vertical gust velocity component of center probe, m/sec (ft/sec)
$w_{g,L}$	measured vertical gust velocity component of left probe, m/sec (ft/sec)
$w_{g,R}$	measured vertical gust velocity component of right probe, m/sec (ft/sec)
x_C	longitudinal distance from INS to center angle-of-attack vane, 5.29 m (17.36 ft)
x_L	longitudinal distance from INS to left angle-of-attack vane, −2.43 m (−7.97 ft)
x_R	longitudinal distance from INS to right angle-of-attack vane, −2.43 m (−7.97 ft)
y_C	lateral distance from INS to center angle-of-attack vane, 0.0 m (0.0 ft)
y_L	lateral distance from INS to left angle-of-attack vane, −9.95 m (−32.64 ft)
y_R	lateral distance from INS to right angle-of-attack vane, 9.12 m (29.92 ft)
α_C	angle of attack measured at center probe, rad
α_L	angle of attack measured at left probe, rad
α_R	angle of attack measured at right probe, rad
β_C	angle of sideslip measured at center probe, rad
β_L	angle of sideslip measured at left probe, rad
β_R	angle of sideslip measured at right probe, rad
θ	pitch attitude, rad
$\dot{\theta}$	pitch rate, rad/sec
σ_w	root-mean-square value of vertical gust component
ϕ	roll attitude, rad
$\dot{\phi}$	roll rate, rad/sec
$\phi_{w_{11}}$	auto-spectrum
$\phi_{w_{12}}$	cross-spectrum

Abbreviations:

ACC	auto-correlation of center probe
ACL	auto-correlation of left probe

ACR	auto-correlation of right probe
ASC	auto-spectrum of center probe
ASL	auto-spectrum of left probe
ASR	auto-spectrum of right probe
CC	cross-correlation
CS	cross-spectrum (for full span)
CSL	cross-spectrum for left semispan
CSR	cross-spectrum for right semispan
EU	engineering units
INS	inertial navigation system
SCC	simulated cross-correlation
SCS	simulated cross-spectrum
SVKAS	sampled Von Kármán auto-spectrum
SVKASC	sampled Von Kármán auto-spectrum for center probe
SVKCS	sampled Von Kármán cross-spectrum (for full span)
SVKCSL	sampled Von Kármán cross-spectrum for left semispan
SVKCSR	sampled Von Kármán cross-spectrum for right semispan
sps	samples per second
VKAC	Von Kármán auto-correlation
VKCC	Von Kármán cross-correlation

A bar over a symbol denotes an average for the run.

Summary

Spanwise spectral relationships are derived for vertical gust velocities measured at the nose and wingtips of the NASA B-57B airplane for six level-flight, low-speed, and low-altitude runs for which the results are compared with predicted Von Kármán model characteristics. The distance between the measurement points at the wingtips was 19.1 m (62.6 ft). Airspeeds ranged from about 100 to 122 m/sec (330 to 400 ft/sec), heights above the ground ranged from near ground level to about 1.6 km (5250 ft), and gust velocity standard deviations ranged from 1.25 to 2.70 m/sec (4.10 to 8.86 ft/sec). Integral scale lengths, approximated from the data, ranged from 125 to 625 m (410 to 2050 ft) and were determined by matching measured atmospheric turbulence auto-correlation estimates with those of the model. Auto- and cross-correlation estimates and auto- and cross-spectrum magnitude estimates are computed and compared with predicted values based upon the homogeneous and isotropic turbulence assumptions of the model.

Digital signals derived from piezoelectric sensors provided continuous pressure and airspeed measurements for the data runs. Some directional sensitivity of the sensors to acceleration was encountered but was eliminated by sensor orientation, and performance was spectrally verified for the higher frequencies to be satisfactory with supplemental onboard piezoresistive sensors.

The Von Kármán atmospheric turbulence model appeared to satisfactorily predict the trends of the measured cross-correlations and cross-spectrum magnitudes. This is especially true for the results between the nose and wingtips. However, the measured magnitude estimates of the cross-spectra between the wingtips exceeded the predicted levels at the higher frequencies. Causes for the additional power across the wingtips were investigated. It was determined that the source of the power was the angle-of-attack data, but its cause remains unknown. If it is not a real atmospheric characteristic, a possible cause could be airplane flow interaction (upwash) at the higher frequencies.

An examination of correlation estimates for the vertical gust velocity components evaluated along and lateral to the flight path implied that the frozen-turbulence-field assumption is a suitable approximation.

Introduction

The development of design techniques for airplane gust response and data for airplane simulators require an adequate description of the nature of the atmospheric turbulence. A program to measure atmospheric turbulence (MAT) along a flight path (ref. 1) was conducted by the National Aeronautics and Space Administration in the 1970's which concentrated upon the long wavelength portion of power spectral density functions. This involved development of a rather sophisticated instrumentation system (ref. 2) and data reduction technique (refs. 3 and 4). The need for spanwise measurements became evident (ref. 5) and, upon completion of the MAT program, additional instrumentation was installed and the SPANMAT program (ref. 6) to measure the spanwise gust velocity gradient was initiated. Wingtip probes were installed on the B-57B MAT airplane, supplementing the original probe located at the nose of the airplane. The airplane was instrumented at the Langley Research Center (LaRC) and operated by the Ames Research Center Dryden Flight Research Facility (DFRF) personnel. The author is indebted to L. J. Ehernberger of DFRF for his liaison effort and many helpful suggestions in the course of the flight sampling activity.

The primary objective of the SPANMAT program was to provide estimates of laterally spaced vertical gust velocity spectrum magnitudes for comparison with the corresponding Von Kármán theoretical spanwise spectrum magnitude functions of reference 7, which are based on the assumption of homogeneous and isotropic turbulence. As shown in reference 7 for the dual logarithmic scale display format, cross-spectrum magnitude estimates of the gusts measured across the span, that is, normal to the flight path, are expected to fall off at an increasing rate with frequency from that of the auto-spectrum estimates. Therefore, for this investigation, interest is focused upon the short wavelength or high frequency portion of the power spectrum. As the theoretical treatment of reference 7 indicates, the parameters affecting the gust cross-spectrum magnitude involve the ratio of the spanwise separation distance between the sensors to the integral scale length value for the turbulence. To best demonstrate the diminishing high frequency power trend in the cross-spectrum magnitude, data runs were sought for low airspeeds and also low altitudes, where the integral scale length is expected to be small. The lateral spatial measurement locations also afford tests of the frozen-turbulence-field assumption. (See ref. 8.) The purpose of this report is to present results and analyses of the vertical gust velocity component from several runs of continuous turbulence where the intensity was sufficiently strong to provide reliable spectral estimates. No attempt is made to relate the measurements to meteorological conditions.

Test Features

Airplane

The two-place NASA B-57B atmospheric sampling airplane used in the Measurement of Atmospheric Turbulence (MAT) program described in references 1, 2, 3, and 9 was modified for the SPANMAT (also called the Spanwise Gradient) test program. Figure 1 is a picture of the instrumented test airplane which was manned by a pilot and also an observer who coordinated the flight runs and the recorder operations. The characteristics of this vehicle, namely, the broad flight envelope with a relatively low stall speed and the stiff, moderately large span wing, made the airplane particularly attractive to this program.

Instrumentation

Figure 1 shows the instrumented SPANMAT probes installed at the wingtips which spanned a distance of 19.07 m (62.58 ft). The limited instrumentation space at the wingtips spurred the MAT airspeed measurement system upgrade which included solid-state, full-range piezoelectric and piezoresistive pressure sensors at the wingtips and nose probes. The MAT inertial navigation system (INS) was also replaced with a unit of later design. Otherwise, the MAT instrumentation of references 2 and 3 was employed in these tests.

The instrumentation parameters measured and recorded onboard the airplane are listed in table I. The parameters include airplane geographic position, inertial speed, three components of airplane acceleration, vertical acceleration, normal acceleration at the wingtips, track angle, attitude angles and their rates of change, flow stagnation or total temperature, control surface positions, and static pressure and, at the nose and wingtips, angles of attack, angles of sideslip, and impact pressures. Parameters continuously measured by the INS are indicated in the table. A time code was provided in the airplane instrumentation as well as in the INS.

Data were recorded onboard the airplane in pulse code modulated (PCM) format on a single 1-hour tape for later ground-based processing. Much of the instrumentation was common to the MAT program but, except for the separate digital INS signals, the MAT program employed only analog signals, and the SPANMAT program employed both analog and digital signals. The piezoelectric sensors generated digital signals which required special treatment. The INS unit was treated as an autonomous unit with its slowly varying signals recorded directly onto tape in PCM format at its standard output sample rate of 20 sps; the rate at which the remaining airplane parameters were sampled was selected to be 200 sps. The analog signals allowed traditional onboard filtering to remove frequency components above 20 Hz, but since the sample rate was variable, the provision of onboard digital filters for the piezoelectric signal was deemed impractical. Instead, the higher sample rate was selected and filtering was deferred to the postflight data reduction process where the signals were low-pass filtered to 20 Hz without phase distortion. To provide adequate resolution for the digital signals, however, the piezoelectric signals were recorded in pairs of channels.

When spectral specifications, such as frequency resolution and statistical confidence, are considered, within limits, the data runs need to be as long as possible. Conditions that limited data run duration were weather, turbulence characteristics, or terrain. The terrain was especially limiting since straight, level, low-altitude flights were sought. Otherwise, experience has shown that if the turbulence does not change significantly, runs of 10-minute duration offer the desired statistical confidence.

The static pressure was measured at the nose probe and impact pressures were measured at each of the three probes with the pitot tube design of the MAT program equipped with the new pressure sensors. The piezoelectric sensors generated digital signals from the varying frequency output of the sensors. These sensors were small and offered good sensitivity with a wide dynamic range. The container enclosing the piezoelectric sensor is shown in figure 2, which is a picture of the instrumentation at the base of one of the airspeed measuring probes. One of the sensors located in the nose compartment of the airplane was dedicated to continuous measurements of the atmospheric static pressure, in contrast to the scheme of the MAT program (refs. 2 and 3) which derived perturbed values about the initial pressure measurements for each run. In addition to providing static pressure to the nose or center pitot tube in the SPANMAT program, this pressure was provided to the wingtip pitot tubes through plastic tubing where the impact pressure at each of the pitot tubes was sensed as a differential pressure between the total pressure and the nose static pressure.

Because the piezoelectric sensors were sensitive to acceleration they were specially oriented, and supplemental piezoresistive sensors were installed to verify the high frequency response of the piezoelectric sensor-derived impact pressure. The piezoresistive sensor is shown in figure 2 suspended in the plastic tubing. It provided an analog signal which could be presample filtered and treated as the other analog signals. Because the signal of this sensor exhibited a drifting trend, however, it was not used for static pressure measurements.

All except the piezoelectric pressure sensors were treated as linear devices. The piezoelectric sensors were described by piecewise linear relations.

Test Procedures

Calibration of the airplane sensors was conducted regularly during the test program. The INS signal gains were adjusted at the manufacturer's facility when the unit underwent repair. Static preflight and postflight levels of the airplane instrumentation signals were recorded manually and on tape for each flight.

As indicated in reference 2, the frequency response characteristics of impact pressure for the probes vary with altitude and pitot tube orifice size. The orifice size is varied to effect a flat frequency response within a given altitude range of interest. To facilitate the orifice selection, the system of pitot tubes and static pressure tubing interconnections was subjected to low-amplitude-pressure resonance tests in the laboratory. To test for altitude effects, pitot tubes with different orifice sizes were ground tested at LaRC and DFRF, for which altitudes were near sea level and 0.7 km (2300 ft), respectively. A 1.09-mm-diameter (0.043-in.) orifice was determined to be appropriate for the lower altitudes sought in this test program and each pitot tube was equipped with the orifice. To prevent measurement contamination from moisture ingestion, it was intended that flights through precipitation be avoided.

Before each flight the INS was aligned and the instrumentation signal levels were recorded. Long, straight, level, constant low-speed, low-altitude passes were sought in clear-air turbulence of at least moderate intensity. At the end of the flights, signal levels were again recorded and, when possible, while the airplane was stationary and ground power was supplied, the slowly oscillating INS readings of the inertial velocity were recorded. Such readings, which can be significant, indicate an accrued level of Schuler inertial velocity error (see, for instance, ref. 10) developed by the INS since alignment. For the airplane at rest the error manifests itself as sinusoidally varying inertial velocity components with an 84.4-minute period. The variation of this error during a flight is generally unknown; however, it is thought to increase with time as a result of airplane maneuvers and dynamic loadings.

Data Analysis

Data Processing

The data processing sequence is depicted schematically in figure 3. The flight tape was first copied in counts onto computer tapes according to the two sampling rates. Factory-supplied calibration coefficients were applied to the 20-sps INS data to yield signals in units appropriate to the analysis. The slowly and smoothly varying INS data were eventually interpolated to a higher sample rate, generally 40 sps, in a later process of merging with the other parameters. Calibration coefficients derived from laboratory tests were similarly applied to the 200-sps data to generate values in analysis units after combining the dual piezoelectric signal words and, in the first of two stages of wildpoint or outlier removal, replacing occasional widely spurious values of the combined signals with previous values. In the second wildpoint removal stage, after converting to analysis units, wild total temperature and static and impact pressure values exceeding multiples of the running standard deviation were replaced by running mean values. Because the wildpoints for the normally smoothly varying total temperatures were readily identifiable, the replacement criterion was set for a somewhat arbitrarily large exceedance standard deviation multiple of 40, and for the randomly varying piezoelectrically derived pressures for which the wildpoints were less conspicuous, a multiple of 7 was chosen. The running means and standard deviations were computed from the five leading and five trailing data values exclusive of the central test value. Following these data adjustments a sharp frequency cut-off was imposed on the pressure data by using the digital filtering scheme of reference 11. Next the main data were decimated to merge with the INS data and the merged data were recorded onto a third computer tape. True airspeeds at each probe and other parameters were computed from the merged data before the vertical gust velocity was computed. The equations used to derive the vertical gust velocity components at the three probes are given next.

Gust Velocity Computations

Airspeeds are first computed from the pressures and total temperature by the following equations:

$$T_c = \frac{t_t + 273.15}{\left(\frac{q_{c,C}}{p} + 1\right)^{2/7}} \tag{1}$$

$$a = c\sqrt{T_c} \tag{2}$$

$$V_C = a\left\{5.0\left[\left(\frac{q_{c,C}}{p} + 1\right)^{2/7} - 1\right]\right\}^{1/2} \tag{3}$$

$$V_L = a\left\{5.0\left[\left(\frac{q_{c,L}}{p} + 1\right)^{2/7} - 1\right]\right\}^{1/2} \tag{4}$$

$$V_R = a\left\{5.0\left[\left(\frac{q_{c,R}}{p}+1\right)^{2/7}-1\right]\right\}^{1/2} \quad (5)$$

Vertical gust velocity time histories for the left, center, and right probes were computed in the data reduction process by removing measured rigid-body airplane motions from air velocity measurements. The equations used to compute the velocities are

$$w_{g,L} = V_L(\alpha_L - \overline{\alpha}_L) - V_L(\theta - \overline{\theta}) + V_{az} - \overline{V}_{az} - y_L\left(\dot{\phi} - \dot{\overline{\phi}}\right) + x_L\left(\dot{\theta} - \dot{\overline{\theta}}\right) - V_L(\beta_L - \overline{\beta}_L)\phi \quad (6)$$

$$w_{g,C} = V_C(\alpha_C - \overline{\alpha}_C) - V_C(\theta - \overline{\theta}) + V_{az} - \overline{V}_{az} - y_C\left(\dot{\phi} - \dot{\overline{\phi}}\right) + x_C\left(\dot{\theta} - \dot{\overline{\theta}}\right) - V_C(\beta_C - \overline{\beta}_C)\phi \quad (7)$$

$$w_{g,R} = V_R(\alpha_R - \overline{\alpha}_R) - V_R(\theta - \overline{\theta}) + V_{az} - \overline{V}_{az} - y_R\left(\dot{\phi} - \dot{\overline{\phi}}\right) + x_R\left(\dot{\theta} - \dot{\overline{\theta}}\right) - V_R(\beta_R - \overline{\beta}_R)\phi \quad (8)$$

For best accuracy from the equations, straight and level flights were sought. In preparation for correlation analyses among the probes, the gust velocity time histories are approximately synchronized by adjusting increments of the sampling time to account for the longitudinal positional difference between the nose and tip probes. Linear trends in the time histories are then removed and, as shown in figure 3, the resulting data were recorded onto a computer tape for analysis.

Spectral Analysis

Normalized correlations[1] and spectrum magnitudes of the measured vertical velocities are computed and compared with Von Kármán atmospheric turbulence model functions. The model functions are described in the appendix. Also discussed in the appendix and displayed in figure 4 are correlation and spectrum magnitude families of the model for different ratios of separation distance to integral scale length s/L. Figure 4 also depicts the normalization used in the report in which the correlation ordinate is normalized to yield a unity auto-correlation function peak value, and the abscissa, expressed in terms of the lag-time increments, is multiplied by the normalizing ratio of the center probe airspeed to integral scale length V/L. In addition to normalizing the spectrum magnitudes by the variance, the magnitudes are multiplied and the frequencies divided by the normalizing ratio. (It might be noted that the units of the reduced frequency fL/V are expressed in cycles.) Of particular interest is the rate at which the cross-spectrum magnitude rolls off at the higher frequencies. Flight conditions were selected to verify the cross-spectrum magnitude deviations from the auto-spectrum in the higher frequency region.

For the runs of this study, gust velocity mean-square values are computed from the time histories and an integral scale length is assigned to the measured data by choosing a value for the run that best matches the set of Von Kármán correlation functions to the estimates. Such a selection must also produce satisfactory agreement with the Von Kármán spectral functions and the measured estimates.

Correlation estimates of the measured data are computed directly from the gust velocity time histories for which linear trends have been removed. For statistical independence considerations, the ratio of the number of data values in the record N_p to the number of lag values in the representative segment of the correlation N_l, that is, N_p/N_l, was set to approximately 10, subject to N_l being chosen to satisfy $N_l = 2^p$, where p is a positive integer. Auto-correlation estimates are computed for the vertical gust velocity of each probe and cross-correlation estimates between them are also computed. While the auto-correlation functions and estimates are normalized to unity for display, the cross-correlation estimates are normalized by the square root of the product of the mean-square values appropriate to the probes of the computation. Spectrum magnitude estimates are computed by performing a fast Fourier transform on the correlation estimates after a window has been applied to the estimate magnitudes. In this study, the Hann window (also called Hanning window, as described in ref. 12, for instance) was used.

Aliasing can result when data are sampled at a uniform rate. It generally manifests itself in a spectrum as smoothly increasing power at high frequencies. (See ref. 13 for a discussion on the effect of aliasing on the measured atmospheric turbulence spectrum.) Figure 5 displays the effect of aliasing for a representative Von Kármán auto-spectrum function derived by sampling its auto-correlation function at the sampling rate of the study. The lower curve is the theoretical spectrum function, and the upper curve is the sampled function. As the Nyquist frequency is approached, aliasing in the sampled auto-spectrum power is shown to increase the power up to about three times that of the theory. No similar aliasing effect on the cross-spectrum was discernible.

[1] Inasmuch as the signal means are set to zero, correlation and covariance functions, as shown in reference 12, are equivalent and hence, for simplicity, only the correlation function or correlation will be used in this report.

Power estimates for the sample rate of 40 sps exist to 20 Hz; however, to reduce any potential discretization effect, the spectra are only displayed to 10 Hz in this report.

Statistical confidence in the spectral estimates is manifested by the number of statistical degrees of freedom. With high statistical degrees of freedom, the estimates exhibit a smooth spectral curve. In general, longer runs produce greater confidence but confidence may also be increased by increasing the ratio of the sample rate to the number of correlation lags. Confidence may be expressed in terms of confidence bands, where a band is a range of an estimated spectrum within which the true spectral value is expected to exist (for instance, see ref. 14) and which decreases with increasing statistical degrees of freedom. When the number of lags is limited, for statistical independence considerations to approximately one tenth of the total number of data points of the run, as in this report, the spectra are constrained to about 20 degrees of freedom. With 90 percent confidence, for instance, such degrees of freedom imply an approximate auto-spectrum confidence interval of

$$0.64 \times \text{Estimated auto-spectrum value}$$

$$\leq \text{True auto-spectrum values}$$

$$\leq 1.84 \times \text{Estimated auto-spectrum value}$$

No confidence interval for the cross-spectra is specified herein but its range is expected to be somewhat greater than that of the auto-spectrum. As will be demonstrated later, 20 degrees of freedom imply significant scatter in the estimates. For the studies of this report, as shown later, a frequency resolution of less than 0.04 Hz was maintained.

Spatial homogeneity and momentarily frozen-turbulence-field assumptions are often applied in atmospheric turbulence studies. An implication of the frozen-turbulence-field assumption, also called Taylor's hypothesis, is that atmospheric turbulence cross-correlations for laterally separated sensors can be equivalently expressed in terms of a representative auto-correlation for which the time lag is delayed by the time for the moving airplane to traverse the separation distance. Thus, as indicated in reference 15, cross-correlations between wingtip measurements should approximate the portion of the center auto-correlation for which the time lags exceed the separation distance, i.e., $t \geq b/V_C$. Such simulated cross-correlation function estimates were created to test the hypothesis. This was done by comparing the simulated and measured correlation and spectrum magnitude estimates, where the simulated cross-spectrum magnitude estimates were computed from the simulated correlation estimates.

Discussion of Results

The instrumented airplane provided simultaneous recordings from which gust velocity time histories were computed along, and at left and right lateral positions from, the airplane centerline. Only the more significant vertical velocity component is treated in this report.

To determine potential effects of wing vibration on the measurements, a coherency test between a wingtip vertical gust velocity and wingtip flow-vane angle of attack for one of the flight runs was performed. The "standard wing" of reference 16 which is representative of the airplane of this program was shown to have a first bending mode frequency of about 5 Hz. In the coherency a small distinct reduction near 5 Hz could be seen but because the effect was very small and no effects of wing flexibility or any other resonances were evident in the spectral estimates the effect of wing flexibility was deemed insignificant.

In general, the airspeed measurement system performed well during the program. High frequency spectral comparisons of piezoelectric- and piezoresistive-derived impact pressures for a turbulent run confirmed that there was no significant corruption of the piezoelectric sensor signal due to acceleration.

Wind vectors derived from the data were examined in reference 13 and were found to change after large airplane maneuvers. This change, primarily attributed to the airplane velocity error of the INS, precluded the measurement of accurate wind descriptions but since the velocity error varies so slowly and only velocity perturbations are considered, the errors were not expected to significantly affect the gust velocity measurement accuracy computed herein.

Flight Descriptions

Six of the longest runs with the most intense continuous turbulence from three different flights were selected for analysis. The runs are designated 2619, 3113, 7105, 7108, 7109, and 7111, where the first two digits denote the flight number and the last two denote the run number of the flight. All runs except run 2619 were conducted in southern California near DFRF. Run 2619 was conducted near Denver, Colorado, during the Joint Airport Weather Studies (JAWS) project (ref. 17). Straight-line flight paths of these runs are shown on contour maps in figure 6. The maps indicate that runs 2619, 7105, and 7111

and much of 7108 and 7109 were conducted over relatively smooth terrain. Run 3113, which was also analyzed in reference 13, was flown over rough terrain. The flight path of run 7111 is shown to cross the paths of runs 7105, 7108, and 7109 which are near each other and essentially parallel. These four runs were made within a period of 45 minutes.

Gust Velocity Descriptions

Table II contains a summary of the basic data for the runs. The data consist of the average altitude as derived from the static pressure, an approximate range of airplane heights above the terrain elevation, the average airspeed, the duration of the run, a deduced Von Kármán integral scale length, and the turbulence intensities derived from time histories for the runs measured at the three probes. The airplane height range was determined by subtracting the average run altitude from the range of terrain elevations derived from straight-line trajectories superimposed on contour maps. The table indicates the low heights and low speeds achieved during the flights, for which the speeds were maintained relatively constant. Airplane flight heights ranged from near the ground level to 1.65 km (5400 ft). Runs 7108, 7109, and 7111, which were shown to have crossing flight paths, are also found to have been flown at similar mean altitudes. However, the records indicate that almost 15 minutes elapsed between the start times of runs 7109 and 7111 and, as previously mentioned, 45 minutes between runs 7105 and 7111. Runs 2619 and 3113 are flown at the lowest airspeed of the runs, near 100 m/sec (328 ft/sec). The other runs are conducted near 120 m/sec (394 ft/sec). Record durations were shorter than the desired 10 minutes with the longest of them of less than 5 minutes duration. Run 2619, which is only 2 minutes long, is included because of its greater turbulence intensity as indicated by the gust intensities included in the table. The integral scale length, the characteristic parameter of the Von Kármán atmospheric turbulence model which for low altitudes is thought to vary with the airplane height above the terrain, is included here and determined subsequently from correlation and spectral characteristics of the run. Gust intensity measurements, which ranged from 1.25 to 2.70 m/sec (4.10 to 8.85 ft/sec), in the table agree with the findings in reference 13, which consistently show the intensity measurements at the center probe to be slightly less than at the tips. This behavior may be attributed to a flow characteristic at the wingtips or possibly to reliance upon a single static pressure source.

Time histories of the vertical gust velocity for each flight run measured at the right, center, and left probes are shown in figures 7 through 12. The figures not only depict the run duration but also provide visible features of some of the turbulence characteristics. Figure 7 presents time histories for run 2619, which is the shortest and most intense run of the report. The time histories of run 3113 in figure 8 are somewhat less intense and show a visible reduction in turbulence intensity beginning about 140 seconds. Most of the time histories, especially figures 10, 11, and 12 which, respectively, correspond to runs 7108, 7109, and 7111, show a more nonstationary turbulence characteristic of short, rather quickly changing periods of relatively constant intensity. Figure 9 shows run 7105 to have the least intensity but the most uniform turbulence.

Figures 13 through 18 show the velocity distribution patterns for the set of runs together with the normal distributions appropriate to the standard deviations of the runs. The lighter gust velocities of run 7105 shown in figure 15 exhibit a near Gaussian distribution. The velocities for runs 2619, 3113, and 7111 displayed in figures 13, 14, and 18 also approach Gaussian distributions. Whereas the distributions of runs 7108 and 7109, shown respectively in figures 16 and 17, have similar magnitudes of occurrences, they exhibit a common skew or asymmetric shift of the velocity range with the number of occurrences. The uniform range shift of the center of the range to more negative values with increasing occurrences is denoted by a positive skew. Inasmuch as the mean is zero, the positive skew indicates more intense but fewer upward directed gusts than downward ones in the time histories, a characteristic that can be verified from figures 10 and 11.

Correlation and Spectral Analysis

Table III contains the primary data processing parameters used to generate the correlation and spectral function estimates for the runs of this report. They include the number of points in the record N_p, the number of leading data points truncated from the wingtip signals to synchronize the longitudinally separated nose and wingtip gust velocity measurements, the number of lags N_l used to describe the correlations, the resulting frequency resolution, the maximum spectral frequency, and the attendant statistical degrees of freedom. The table shows that for the sample rate of 40 sps and the airspeeds of each of the runs, approximate synchronization in increments of the sample period could be achieved for all runs by truncating three data points. All runs, except run 2619, were long enough to describe the correlations using 1024 lags and yielded a fine spectral resolution of 0.020 Hz. The brevity of run 2619 only permitted 512 lags for a resolution of 0.039. The

statistical degrees of freedom for the runs, which indicate rather poor statistical confidence, ranged from 18 to 23.

Before showing comparisons of the measured and theoretical correlations and spectra, the effect of the integral scale length normalization on the measured correlations and spectra in their normalized forms will be illustrated. Figure 19(a) displays a stacked arrangement of normalized auto- and cross-correlation pairs; figure 19(b), the spectral estimate auto- and cross-spectrum pairs for run 7105. Correlations and spectra for an integral scale length chosen to match the Von Kármán model and also for halving and doubling the chosen length value are shown in the figures. The corresponding theoretical correlation functions appropriate to the selected length value are similarly displayed. The correlation pairs for which the scale length is one half the selected value are displayed at the top; below it are the pairs for the selected scale length, the model and, at the bottom, the doubled scale length. The curves show the similarity of the model and estimate correlation shapes for the selected scale length and also show how varying the scale length alters the horizontal scale of the correlation description. Specifically, increasing the scale length has the effect of compressing the abscissa scale of the estimated correlation function. The measured auto- and cross-spectrum estimates of figure 19(b), specified in terms of $\phi_{w_{12}} V/\sigma_w^2 L$, are displayed as vertically displaced pairs, differing by multiplicative factors of 10. Model spectrum functions are also superimposed. The halved scale-length spectra are shown at the top and the selected and doubled scale-length spectrum pairs are shown below them. The figure shows the effects of the normalized display. Increasing the integral scale length L shifts the relative position of the estimates downward and to the right. Also, increasing the intensity σ_w^2 simply shifts the estimates downward.

Figures 20 through 25 show normalized correlations and spectra for runs 2619, 3113, 7105, 7108, 7109, and 7111, respectively. Figures 20(a), 21(a), 22(a), 23(a), 24(a), and 25(a) show theoretical functions and measured estimates for the auto-correlation at the center probe and the cross-correlation for the greatest separation distance, that is, between the tip probes. Corresponding auto- and cross-spectra are also shown. Integral scale lengths, which ranged from 125 to 625 m (410 to 2050 ft), of the theoretical functions have been varied until the correlations best match the estimates. The cross-spectrum magnitude estimates are shown below the auto-spectrum estimates, shifted by an order of magnitude for clarity, and the theoretical auto-spectrum function is repeated with the theoretical cross-spectrum magnitude function to provide spectral envelopes. The slight aliasing effect discussed previously which is caused by discretization is included in the theoretical spectral functions. Figures 20(b), 21(b), 22(b), 23(b), 24(b), and 25(b) show enlarged views of the normalized correlation functions and estimates in the region of few lags. It might be noted that this region ideally defines the high frequency asymptotic behavior of the spectra and a place where the cross-correlation estimates can typically be seen to be nonsymmetric.

In the past, the assignment of an integral scale length has at times been determined by matching the measured spectral estimates with those of the Von Kármán model. When low frequency components in the measured spectrum inadequately define the knee or the slope change of the curve displayed in the dual logarithmic scale format, a match was difficult. On the other hand, for a sufficiently long atmospheric turbulence record, the correlation functions always possess their key pulse-shaped correlation attributes, and since correlations relate closely to the measured data, the functions can help identify data characteristics that enhance matching to the model. The scale lengths for this report are determined from the normalized correlations and the resulting spectra are superimposed on the spectrum of the model appropriate to the length and the mean-square value supplied in table II.

The correlation functions in this study, as shown in figure 26, are examined in terms of three regions: the central region of few lags where the function has the greatest magnitude, the intermediate region containing the characteristic slope, and the outer low magnitude region of the higher lags. After normalizing the auto-correlations to unity, matching of the estimates with the Von Kármán function is primarily sought for the intermediate region of the auto-correlation functions with some consideration for matching the region of fewest lags. Each correlation estimate exhibits the characteristic atmospheric-turbulence pulse shape in the central and at least part of the intermediate regions. The estimates in figures 20, 22, and 25 appear to match the model function shape best. The correlation estimates of run 7108 given in figure 23(a) do not fit the Von Kármán model well because the correlation exhibits more than a single characteristic slope in the intermediate region. The scale length for this run was chosen to best match the slope where the lags are less. It is suggested in reference 18 that the shallow slope in the intermediate region that extends into the higher lag region results from the presence of very low frequency components in the signal. The correlations of figure 24(b) show undulations having

a normalized period of about 0.5, which corresponds to a power increment in the spectra of figure 23(a) at a reduced frequency of 2.0 or nonnormalized frequency of approximately 0.4 Hz. However, the time history of figure 10 is too short to accurately confirm any such period for the shallow sloping portion of the correlation.

As shown in figures 20 through 25, all the measured auto-spectrum estimates in the figures exhibit the general form of the sampled, finite-duration Von Kármán spectrum magnitude functions appropriate to the assumed integral scale lengths of table II where the functions have been superimposed for comparison in the figures. Although the spectra of run 7108 depicted in figure 24(a), which contained the shallow slope in the correlation, exhibit no knee, it has been possible to assign a scale length to the run using the correlations such that the spectral estimates and model spectrum functions satisfactorily overlay. The measured cross-spectrum estimate magnitudes of the runs of figures 20 through 25 also appear to generally match the theoretical cross-spectrum function form up to a normalized frequency of about 2 cycles; beyond it, however, the cross-spectral magnitudes exceed the predicted rate of roll-off.

Potential sources for the excessive cross-spectrum intensity at the higher frequencies were sought. First, signs of aliasing in the spectrum estimates were checked by increasing the sampling rate. Figure 27 shows the correlation and spectrum magnitude estimates together with the related functions for run 2619 sampled at a rate of 200 sps and processed for 4096 lags. When compared with figure 20(a), the spectral estimates for the 40 sps sample rate of figure 20(a) are only perceptibly greater; this indicates a slight amount of aliasing is present but the amount of change does not account for the 2-orders-of-magnitude difference between the theoretical spectral function and measured estimates near 10 Hz. Furthermore, with regard to possible aliasing from the airspeed measurement which lacked onboard filtering, the gust velocity equations show that small airspeed errors have only a secondary impact on the computation of the vertical velocities and, hence, the spectral estimates. Whereas the Von Kármán model does not rely upon the assumption of signal stationarity, the significance of a unique power spectrum for the data does require the assumption. Reference 19 indicates that the effect of nonstationarity on the spectrum is to smooth the spectral knee. Nevertheless, to confirm that the additional high frequency power was not due to stationarity, one of the runs, run 7105, which exhibited the additional power was found to satisfy the tests for stationarity as given in reference 12. Thus, it is concluded that the high frequency power increment is not attributed to a lack of stationarity.

Next, the constituents of the gust velocities were examined for evidence of the additional high frequency spectral power. The primary component of the vertical gust velocities as specified in equations (6) to (8), which is the product of the true airspeed and the angle of attack, was synthesized for each probe from the product of the angle of attack and the average airspeed for the run. Auto- and cross-correlation and auto- and cross-spectrum magnitude estimates of the synthesized components for the center probe and between the wingtip probes, respectively, are shown for run 2619 in figure 28. The figure depicts very similar high frequency spectral estimates as those of figure 20(a) and, hence, since the angle-of-attack measurements are the only variables in the synthesized components, the flow-vane measurements must contain the questionable high frequency signal content. Unpublished frequency response data on the flow vanes have confirmed that for the impact pressures and altitudes of the tests, the natural frequency of the vanes is above 25 Hz and the damping is above 70 percent of critical. For an assumed second-order system, these specifications should imply a vane response below 10 Hz that responds quite directly to a disturbance and, hence, would not introduce spurious signal frequency content. In addition, since the theoretical and measured auto-spectra agree well up to 10 Hz, it is concluded that the high frequency cross-spectral behavior may properly describe the measurement.

The effect of the sensor separation distance on the spectrum magnitude estimates was also examined. Figure 29 displays the two nose-to-wingtip and wingtip-to-wingtip cross-spectrum magnitude estimates for run 7105 in the normalized form. These, together with the center probe auto-spectrum estimates, are plotted in figure 29(a) for the customary 1023 lags and, for greater confidence, they are shown for 127 lags in figure 29(b). The order of the curves from top to bottom is: the center auto-spectrum estimates and the cross-spectrum magnitude estimates between the center and the left probes, the center and the right probes, and the wingtip probes, respectively. Von Kármán spectral functions are included for comparison and clarification, where the cross-spectrum magnitude estimates between the wingtip probes, or the lower curve, have twice the separation distance, and hence, as indicated in reference 7, depict the greater roll-off rate compared with the two center-to-wingtip probe curves. The measured cross-spectra across the semispan show good

agreement with the model for the full frequency range while those across the span exhibit the additional high frequency power. The additional power suggests some correlation between the wingtip measurements that does not exist in the semispan computations. This phenomenon, and hence, the additional power in question, may be due to interaction with the airplane flow at the wingtips, although it is not understood why the power only exists at the higher frequencies. Figure 29(c) shows an enlarged view of the measured estimates and theoretical functions of the cross-correlations and center probe auto-correlations for the three separation relationships of the cross-spectra for the region of few lags. As expected, the correlation peaks are diminished and more rounded as the separation distance increases.

Figures 30 through 35 show stacked sets of normalized correlation and spectrum magnitudes with vertically displaced figure origins for the six runs of this report. The normalized correlation and spectrum magnitude are displayed for the integral scale lengths given in table II. The order of display of the curves in the correlation set from top to bottom is the Von Kármán auto-correlation function, the left probe auto-correlation estimates, the center probe auto-correlation estimates, the right probe auto-correlation estimates, the simulated cross-correlation estimates constructed from the center probe estimates, the measured estimates, and the Von Kármán function of the cross-correlation between the wingtips. The spectra are similarly arranged.

Except for the characteristic difference between the auto- and cross-correlations in the region of few lags, the normalized correlation estimates are similar. Of particular note are the similarities of the auto-correlation estimates and, hence, the auto-spectrum estimates for the three probes that result across the 19-m (63-ft) probe-separation distance. The cross-correlation estimates are shown to have reduced and more rounded peaks and exhibit slight unsymmetrical features. The absence of marked differences among the auto-correlation and the auto-spectrum estimates in these figures suggests that the probe-separation distance is short compared with the integral scale length.

The likeness of the simulated cross-correlation and cross-spectrum magnitude estimates to their true counterparts suggests validity to the frozen-turbulence-field assumption. Table IV was compiled to numerically examine the hypothesis for the lag argument of zero for the cross-correlation estimates. As implied earlier, the cross-correlation values should be approximated by the auto-correlation values appropriate to the measurement separation distance of the sensor signals used in the cross-correlation. The zero-lag auto-correlation estimates, or the mean-square values, of the left, center, and right probes, respectively, are denoted by R_0^{LL}, R_0^{CC}, and R_0^{RR} and are displayed in the first three data columns for reference. Since they are the peak auto-correlation estimates, they are the correlation normalizing factors. The zero-lag cross-correlation estimates between the left and center and the center and right probes, respectively denoted R_0^{LC} and R_0^{CR}, are contained in the next two columns. For the hypothesis to be valid the values in these two columns should and do roughly approximate the auto-correlation estimates of the left, center, and right probes for which the equivalent lag time is $t = b/2V_C$ and is respectively denoted in the next three columns by R_{LC}^{LL}, R_{LC}^{CC}, and R_{LC}^{RR}. Similarly, the zero-lag estimate of the cross-correlation function between the wingtips, R_0^{LR}, given in the next column compares favorably with the left, center, and right auto-correlation estimates, R_{LR}^{LL}, R_{LR}^{CC}, and R_{LR}^{RR}, appropriate to the wing span b. In view of the agreements of the true and simulated cross-correlation and cross-spectrum magnitudes and the satisfactory numerical correlation comparisons, the frozen-turbulence-field assumption appears to be essentially true.

Concluding Remarks

Vertical gust velocities measured at three spanwise locations across a 19.07-m (62.58-ft) wing span are spectrally analyzed for six level flights. Integral scale lengths associated with the Von Kármán atmospheric turbulence model are approximated from the data. Normalized auto- and cross-correlation estimates and auto- and cross-spectrum magnitude estimates are computed and compared with predicted model values derived assuming homogeneous, isotropic turbulence.

Airspeeds ranged from about 100 to 122 m/sec (330 to 400 ft/sec), heights above the ground ranged from near ground level to about 1.65 km (5400 ft), and standard deviations of gust velocity ranged from 1.25 to 2.70 m/sec (4.10 to 8.85 ft/sec). Integral scale lengths, which ranged from 125 to 625 m (410 to 2050 ft), were determined by matching the measured atmospheric turbulence auto-correlation estimates with the Von Kármán model; the matching of correlations yielded more satisfying results than by matching spectra.

Digital signals derived from piezoelectric sensors provided sensitive and continuous pressure and airspeed measurements in the program. A slight sensitivity to acceleration discovered for the sensors was essentially eliminated by sensor orientation. For a

turbulent run, little or no differences were found in the impact pressure spectra between the piezoelectric and supplemental piezoresistive sensors at high frequencies.

The Von Kármán atmospheric turbulence model, spatially extended to yield cross-correlations and cross-spectrum magnitudes, appeared to satisfactorily predict the trends of the atmospheric turbulence correlations and spectrum magnitudes. This is especially true for the results between the nose and wingtips. However, the measured magnitude estimates of the cross-spectra between the wingtips exceeded the predicted levels at the higher frequencies. Causes for the additional power across the wingtips were investigated. It was determined that the source of the power was the angle-of-attack data, but its cause remains unknown. If it is not a real atmospheric characteristic, a possible cause could be airplane flow interaction (upwash) at the higher frequencies.

Similar correlation estimates for the vertical gust velocity component at positions along and normal to the flight path implied that the frozen-turbulence-field assumption is essentially true.

NASA Langley Research Center
Hampton, VA 23665-5225
January 16, 1990

Appendix

Von Kármán Atmospheric Turbulence Spectral Model for Vertical Gust Component

Atmospheric turbulence has been spectrally described in terms of the Von Kármán atmospheric turbulence model. Parameters which specify the model auto-correlation and auto-spectrum functions are its variance, or mean-square value of the gust velocity, and an integral scale length. The description of the cross-correlation and cross-spectrum functions also incorporates a spacing parameter to account for the separation distance between measuring sensors. The variance specifies the intensity, and the scale length relates to the frequency content or distribution.

The basis for the auto-spectral model was presented in reference 20, and its application in airplane design is described in references 21 and 22. The model was extended for cross-spectral applications in reference 7.

In reference 7, the cross-correlation function $R_{w_{12}}(t)$ for the vertical gust component is given by

$$R_{w_{12}}(t) = \sigma_w^2 \frac{2^{2/3}}{\Gamma(1/3)} (u)^{1/3} \left[K_{1/3}(u) - \frac{1}{2} u \, K_{2/3}(u) \right] \tag{A1}$$

where

$$u = \frac{1}{1.339} \sqrt{\sigma^2 + \left(\frac{V_t}{L} \right)^2}$$

$$\sigma = \frac{s}{L}$$

t is lag time, Γ is the gamma function, L is the integral scale length, s is the lateral distance between the sensors, V is the airspeed, σ_w^2 is the mean-square value of the vertical gust component, and $K_{1/3}(u)$ and $K_{2/3}(u)$ are the modified Bessel functions of the second kind for orders one third and two thirds, respectively. The auto-correlation function $R_{w_{11}}(t)$ results from equation (A1) when the lateral distance s is zero.

The cross-spectrum $\phi_{w_{12}}(f)$, normalized such that $\int_0^\infty \phi_{w_{11}}(f)/\sigma_w^2 \, df$ is unity, is given by

$$\phi_{w_{12}}(f) = \sigma_w^2 \frac{2^{7/6} L}{V \Gamma(1/3)} \sqrt{\pi} \left(\frac{1}{1.339} \right)^{8/3} \left[\frac{8}{3} (1.339)^2 \left(\frac{\sigma^2}{z} \right)^{5/6} K_{5/6}(z) \left(\frac{\sigma^2}{z} \right)^{11/6} K_{11/6}(z) \right] \tag{A2}$$

where the auto-spectral function $\phi_{w_{11}}(f)$, corresponding to equation (A2) with $s = 0$, is

$$\phi_{w_{11}}(f) = 2L\sigma_w^2 \frac{1 + 8(2.678\pi f L/V)^2/3}{V \left[1 + (2.678\pi f L/V)^2 \right]^{11/6}} \tag{A3}$$

$$z = \frac{\sigma}{1.339} \sqrt{1 + (2.678\pi f L/V)^2}$$

f is frequency, and $K_{5/6}(z)$ and $K_{11/6}(z)$ are the modified Bessel functions of the second kind for orders five sixths and eleven sixths, respectively.

Graphs of general forms of these functions are shown in figure 4 in terms of normalizing ratios σ and V/L. Figure 4(a) shows a family of the normalized Von Kármán auto- and cross-correlation functions and auto- and cross-spectrum magnitude functions in a dual logarithmic scale format for a range of spacing parameter values σ and a unity mean-square value σ_w^2. Both the correlation and spectrum functions are displayed for values of the parameter σ of 0, 0.01, 0.05, 0.2, and 1, where the zero σ value correlation and spectrum functions correspond to the

auto-correlation and auto-spectrum functions, respectively. The spectrum magnitude function ordinate values are also multiplied by the ratio L/V, and the frequencies along the abscissa of their display are divided by the same ratio to yield reduced frequencies. The correlation function magnitudes are normalized to yield a unity auto-correlation function peak ordinate value and the correlation function abscissa, derived in terms of the lag-time increments, is normalized by multiplying the lag-time increments by the normalizing ratio V/L, where the lag time is the time between the two shifted time histories in the correlation computation process. (A sampled lag time may also be specified in terms of the number of sample-time increments or lags.) Figure 4(b) is an enlarged view of the correlation functions.

For a large number of lags or large lag time, the figures show that the cross-correlation and auto-correlation functions are equivalent. In the region of few lags the cross-correlation function magnitudes are less than those of the auto-correlation functions and have rounded peaks. The differences between the peak values of the auto- and cross-correlation functions and the slopes of the functions change with the spacing parameters. For the known separation distance between the airplane probes, the peak difference relates inversely to the scale length of the flight run.

The cross-spectra are shown to have less power than the auto-spectra, decreasing with sensor separation distance and smaller integral scale lengths. The noticeable characteristic of the cross-spectra, however, is the reduced power at the higher frequencies where the slope becomes steeper with frequency.

References

1. Murrow, Harold N.; and Rhyne, Richard H.: The MAT Project—Atmospheric Turbulence Measurements With Emphasis on Long Wavelengths. *Proceedings of the Sixth Conference on Aerospace and Aeronautical Meteorology of the American Meteorological Society*, Nov. 1974, pp. 313–316.
2. Meissner, Charles W., Jr.: *A Flight Instrumentation System for Acquisition of Atmospheric Turbulence Data.* NASA TN D-8314, 1976.
3. Rhyne, Richard H.: *Flight Assessment of an Atmospheric Turbulence Measurement System With Emphasis on Long Wavelengths.* NASA TN D-8315, 1976.
4. Keisler, Samuel R.; and Rhyne, Richard H.: *An Assessment of Prewhitening in Estimating Power Spectra of Atmospheric Turbulence at Long Wavelengths.* NASA TN D-8288, 1976.
5. Houbolt, John C.: Effect of Spanwise Gust Variations. *Proceedings: Third Annual Workshop on Meteorological and Environmental Inputs to Aviation Systems,* Dennis W. Camp and Walter Frost, eds., NASA CP-2104, FAA-RD-79-49, 1979, pp. 72–79.
6. Camp, Dennis; Campbell, Warren; Frost, Walter; Murrow, Harold; and Painter, Wenneth: NASA's B-57B Gust Gradient Program. *J. Aircr.*, vol. 21, no. 3, Mar. 1984, pp. 175–182.
7. Houbolt, John C.; and Sen, Asim: *Cross-Spectral Functions Based on Von Kármán's Spectral Equation.* NASA CR-2011, 1972.
8. Taylor, Geoffrey Ingram: The Spectrum of Turbulence. *Proc. Royal Soc. (London),* ser. A, vol. 164, Feb. 18, 1938, pp. 476–490.
9. Davis, Richard E.; Champine, Robert A.; and Ehernberger, L. J.: *Meteorological and Operation Aspects of 46 Clear Air Turbulence Sampling Missions With an Instrumented B-57B Aircraft. Volume I—Program Summary.* NASA TM-80044, 1979.
10. Rhyne, Richard H.: *Accuracy of Aircraft Velocities Obtained From Inertial Navigation Systems for Application to Airborne Wind Measurements.* NASA TM-81826, 1980.
11. Graham, Ronald J.: *Determination and Analysis of Numerical Smoothing Weights.* NASA TR R-179, 1963.
12. Bendat, Julius S.; and Piersol, Allan G.: *Random Data—Analysis and Measurement Procedures,* Second ed. (Revised and Expanded). John Wiley & Sons, Inc., c.1986.
13. Frost, Walter; Chang, Ho-Pen; and Ringnes, Erik A.: *Analyses and Assessments of Span Wise Gust Gradient Data From NASA B-57B Aircraft.* NASA CR-178288, 1987.
14. Otnes, Robert K.; and Enochson, Loren: *Digital Time Series Analysis.* John Wiley & Sons, Inc., c.1972.
15. Mark, William D.: *Some Implications of the Isotropic Momentarily Frozen Assumptions for the SPAN-MAT Program.* NASA CR-181937, 1986.
16. Pastel, Robert L.; Caruthers, John E.; and Frost, Walter: *Airplane Wing Vibrations Due to Atmospheric Turbulence.* NASA CR-3431, 1981.
17. National Center for Atmospheric Research; and Univ. of Chicago: *The JAWS Project—Operations Summary 1982.* Feb. 1983.
18. Murrow, Harold N.; McCain, William E.; and Rhyne, Richard H.: *Power Spectral Measurements of Clear-Air Turbulence to Long Wavelengths for Altitudes up to 14 000 Meters.* NASA TP-1979, 1982.
19. Mark, William D.; and Fischer, Raymond W.: *Investigation of the Effects of Nonhomogeneous (or Nonstationary) Behavior on the Spectra of Atmospheric Turbulence.* NASA CR-2745, 1976.
20. Von Kármán, Theodore: Progress in the Statistical Theory of Turbulence. *J. Mar. Res.,* vol. VII, no. 3, 1948, pp. 252–264.
21. Houbolt, John C.: *Design Manual for Vertical Gusts Based on Power Spectral Techniques.* AFFDL-TR-70-106, U.S. Air Force, Dec. 1970. (Available from DTIC as AD 879 736.)
22. Houbolt, John C.; Steiner, Roy; and Pratt, Kermit G.: *Dynamic Response of Airplanes to Atmospheric Turbulence Including Flight Data on Input and Response.* NASA TR R-199, 1964.

Table I. Aircraft Instrumentation Parameters

Parameter	Application
Inertial position (INS)	Earth longitude and latitude
Inertial speed (INS)	Earth longitude and latitude speeds
Acceleration	Vertical (INS), normal (cg, wingtips), longitudinal (cg), and lateral (cg)
Track angle (INS)	
Attitude angle (INS)	Pitch (θ), yaw, roll (ϕ)
Attitude rate	Pitch ($\dot{\theta}$), yaw, roll ($\dot{\phi}$)
Angle of attack	Nose (α_C), left (α_L), and right (α_R) wingtips
Angle of sideslip	Nose (β_C), left (β_L), and right (β_R) wingtips
Static pressure (pitot tube, digital)	Nose only (p)
Impact pressure (pitot tube, digital)	Nose ($q_{c,C}$), left ($q_{c,L}$), and right ($q_{c,R}$) wingtips
Temperature	Total (t_t)
Control position	Engine throttles, ailerons, elevator, rudder, stabilizer, flaps, and speed brakes
Time code (aircraft and INS)	

Table II. Basic Run Characteristics

	Altitude		Approximate height range		Airspeed			Integral scale length		Left probe gust intensity (std. dev.)		Center probe gust intensity (std. dev.)		Right probe gust intensity (std. dev.)	
Run	km	ft	m	ft	m/sec	knots	Duration, sec	m	ft	m/sec	ft/sec	m/sec	ft/sec	m/sec	ft/sec
2619	1.81	5938	140–340	460–1110	103.0	200.2	121.1	125	410	2.67	8.75	2.51	8.23	2.70	8.85
3113	1.53	5019	20–1520	50–4980	101.4	197.1	268.8	175	570	2.41	7.90	2.30	7.54	2.43	7.97
7105	0.89	2920	20–510	50–1670	119.1	231.5	231.9	100	330	1.36	4.46	1.25	4.10	1.43	4.69
7108	1.28	4199	200–1500	660–4920	121.5	236.1	295.0	625	2050	2.12	6.95	2.02	6.62	2.16	7.08
7109	1.29	4232	440–1640	1440–5380	121.2	235.6	274.1	470	1540	2.04	6.69	1.95	6.39	2.10	6.88
7111	1.29	4232	840–1640	2760–5380	121.8	236.7	291.0	510	1670	2.03	6.66	1.96	6.43	2.08	6.82

Table III. Data Processing Run Characteristics

Run	Number of points, N_p	Number of truncated points	Number of lags, N_l	Spectral frequency resolution, Hz	Maximum spectral frequency, Hz	Degrees of freedom
2619	4 848	3	512	0.039	20	19
3113	10 756	3	1024	.020	20	21
7105	9 280	3	1024	.020	20	18
7108	11 804	3	1024	.020	20	23
7109	10 968	3	1024	.020	20	21
7111	11 645	3	1024	.020	20	23

Table IV. Correlation Values

Run	Zero-lag auto-correlation estimates			Zero-lag cross-correlation estimates across semispan		Auto-correlation estimates for semispan			Zero-lag cross-correlation estimates across semispan	Auto-correlation estimates appropriate to wing span		
	R_0^{LL}	R_0^{CC}	R_0^{RR}	R_0^{LC}	R_0^{CR}	R_{LC}^{LL}	R_{LC}^{CC}	R_{LC}^{RR}	R_0^{LR}	R_{LR}^{LL}	R_{LR}^{CC}	R_{LR}^{RR}
2619	7.1285	6.2961	7.2906	5.9199	5.9315	6.2276	5.4100	6.2601	5.8627	5.4767	4.8718	5.3596
3113	5.8243	5.2818	5.9164	4.8214	4.7791	5.0219	4.5267	5.0452	4.6139	4.3412	4.0535	4.3136
7105	1.8575	1.5597	2.0537	1.3566	1.4168	1.4924	1.2160	1.6577	1.3776	1.2214	1.0219	1.3658
7108	4.5026	4.0843	4.6650	4.0585	4.1164	4.2544	3.8499	4.4102	4.2122	4.0313	3.6973	4.1832
7109	4.1664	3.7996	4.3908	3.7135	3.7827	3.8877	3.5357	4.0986	3.7983	3.6348	3.3652	3.8389
7111	4.1262	3.8441	4.3236	3.7315	3.8173	3.8712	3.6017	4.0359	3.8371	3.6562	3.4437	3.7868

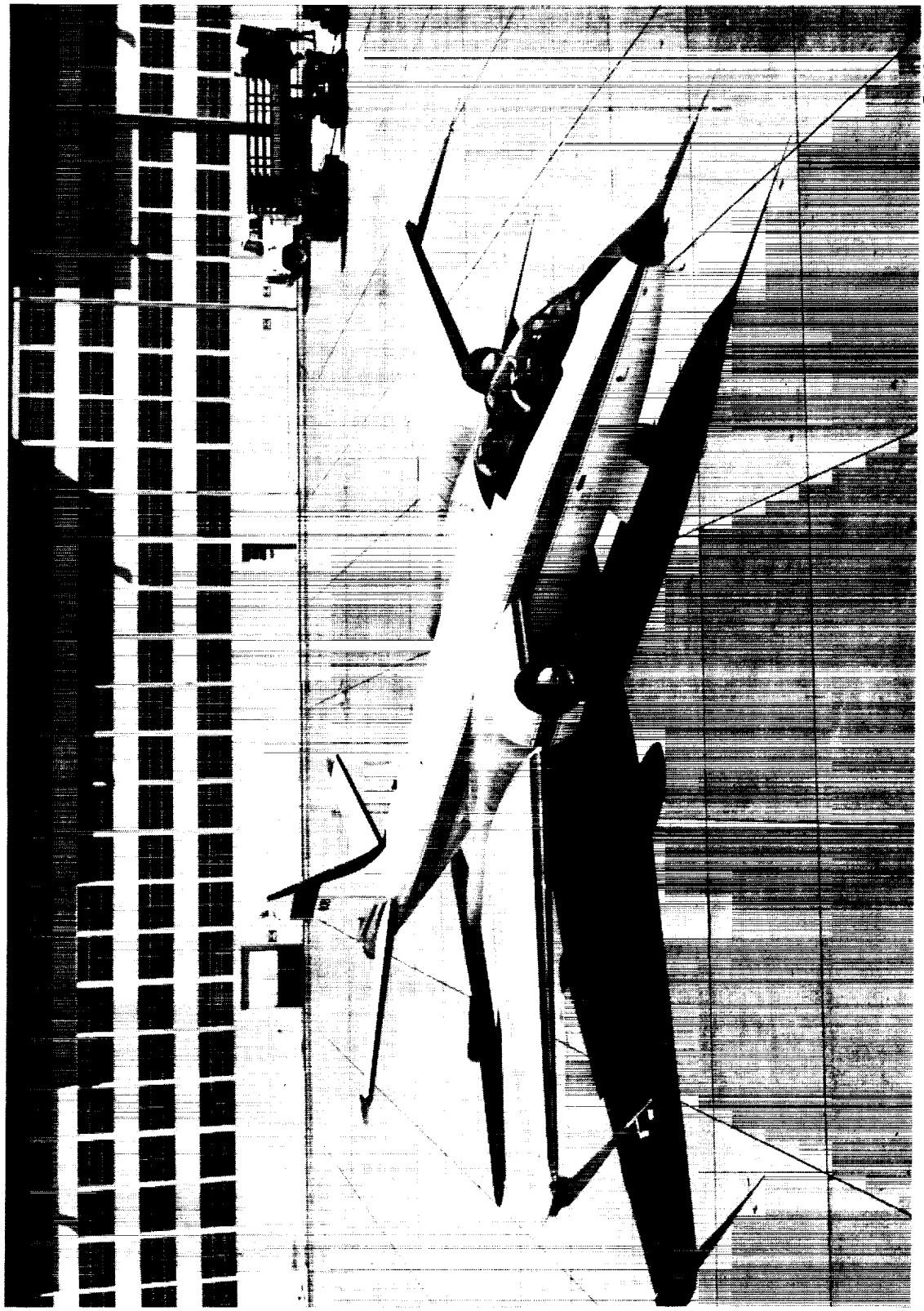

L-82-2612

Figure 1. NASA B-57B SPANMAT test airplane.

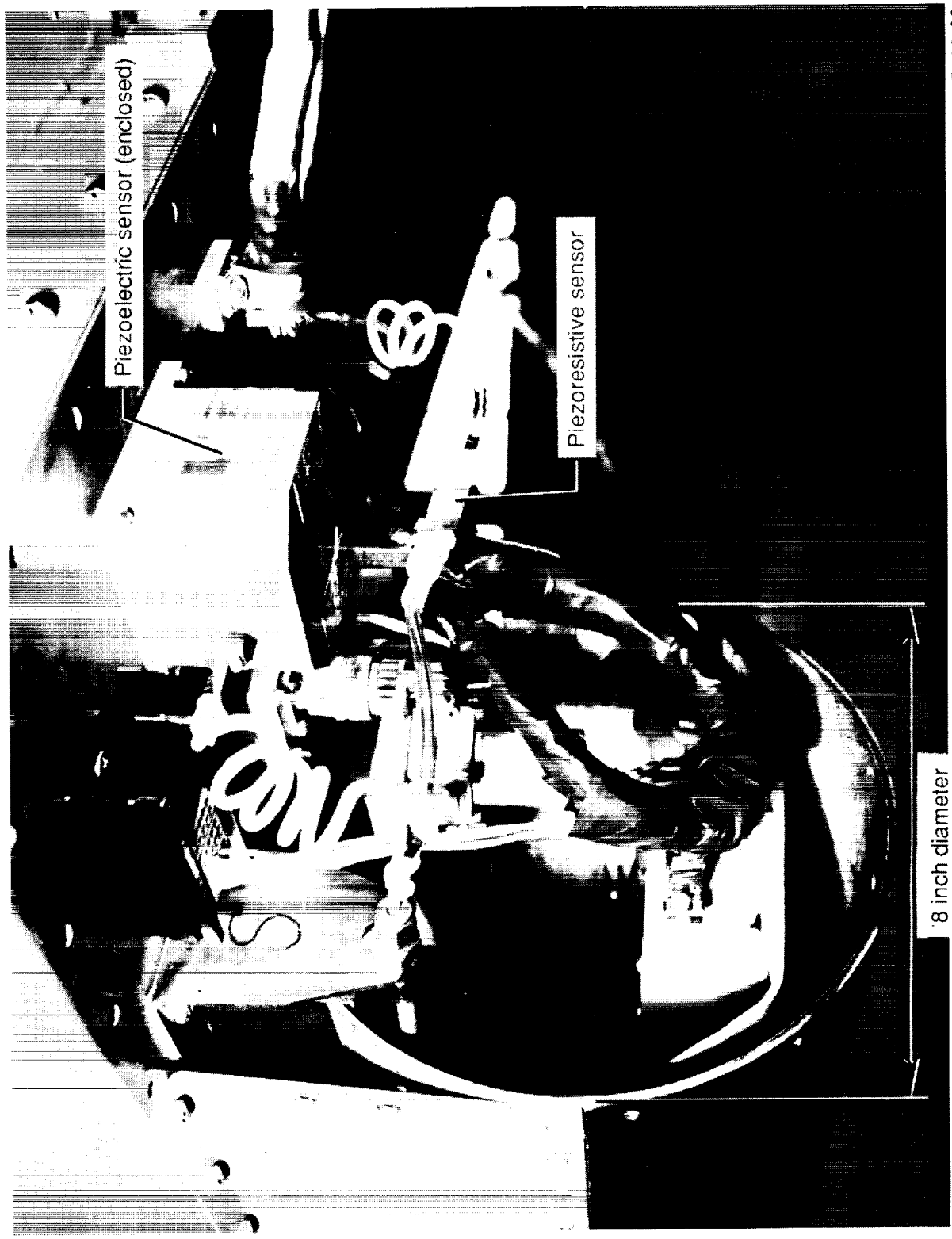

Figure 2. Instrumentation at base of airspeed measuring probe.

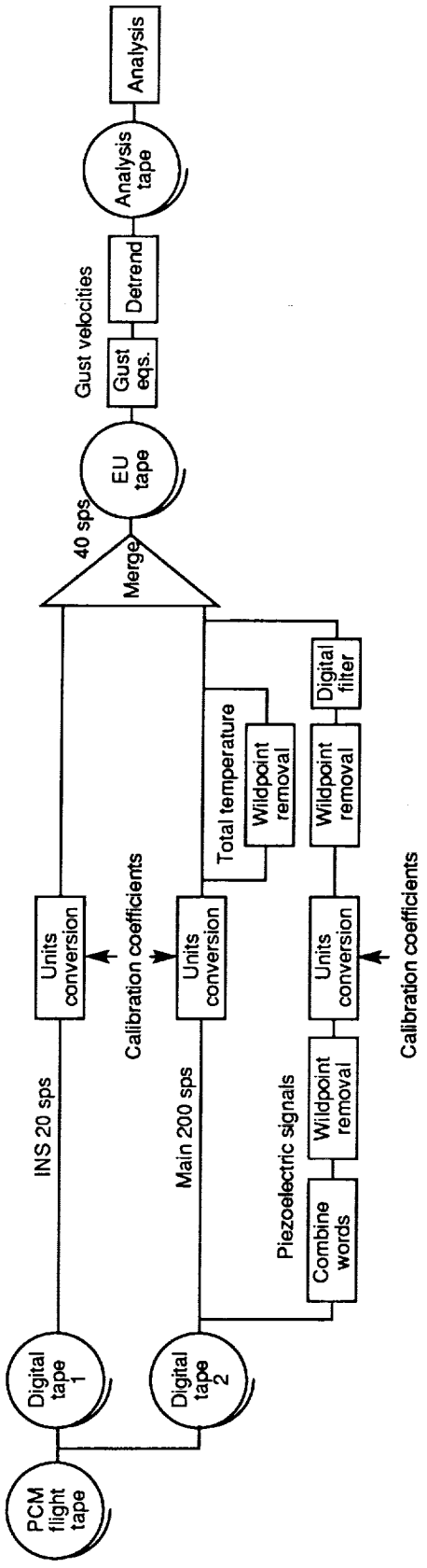

Figure 3. Data reduction schematic.

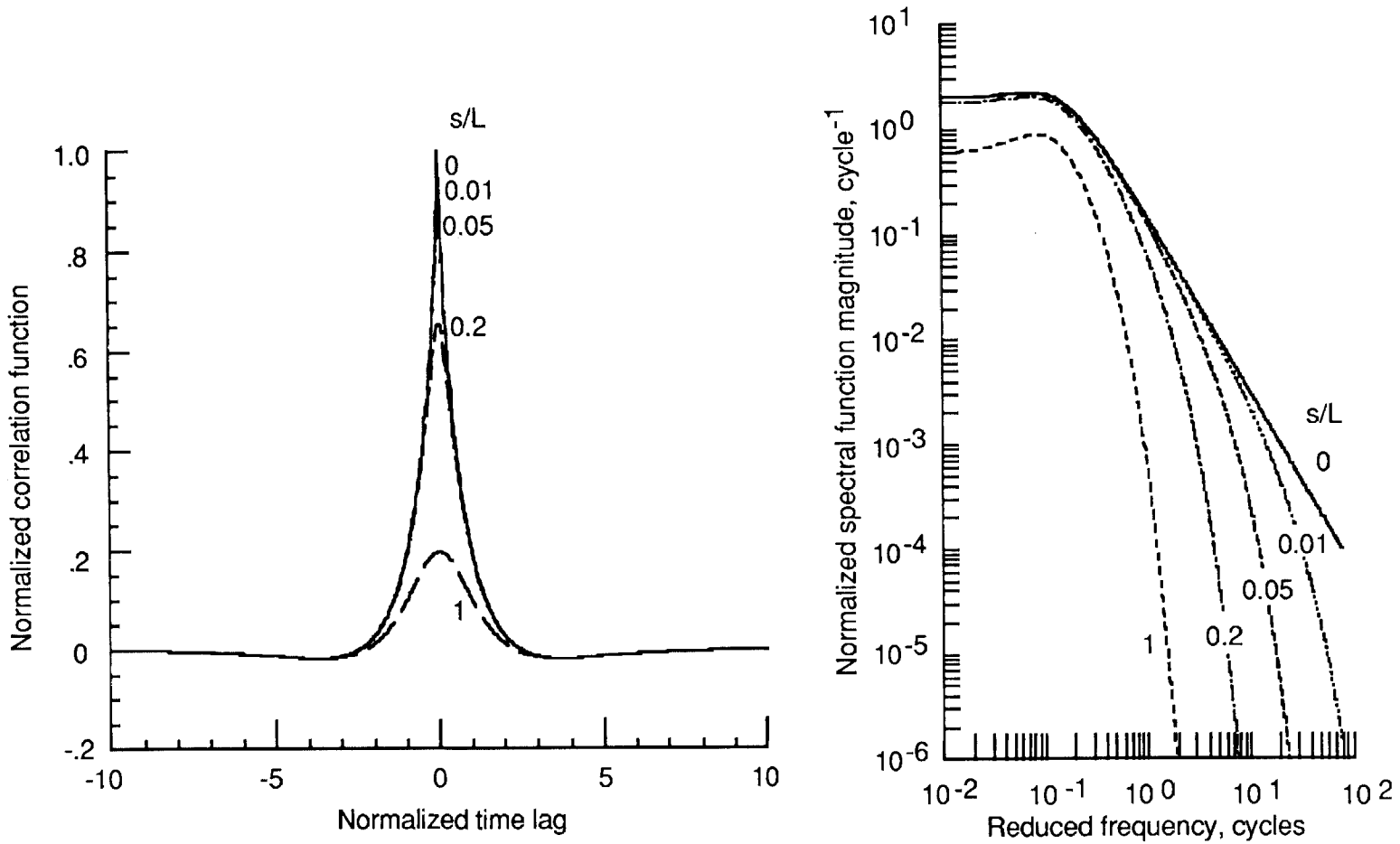

(a) Correlation and spectral function families.

Figure 4. Von Kármán atmospheric turbulence model changes with lateral sensor spacing parameters.

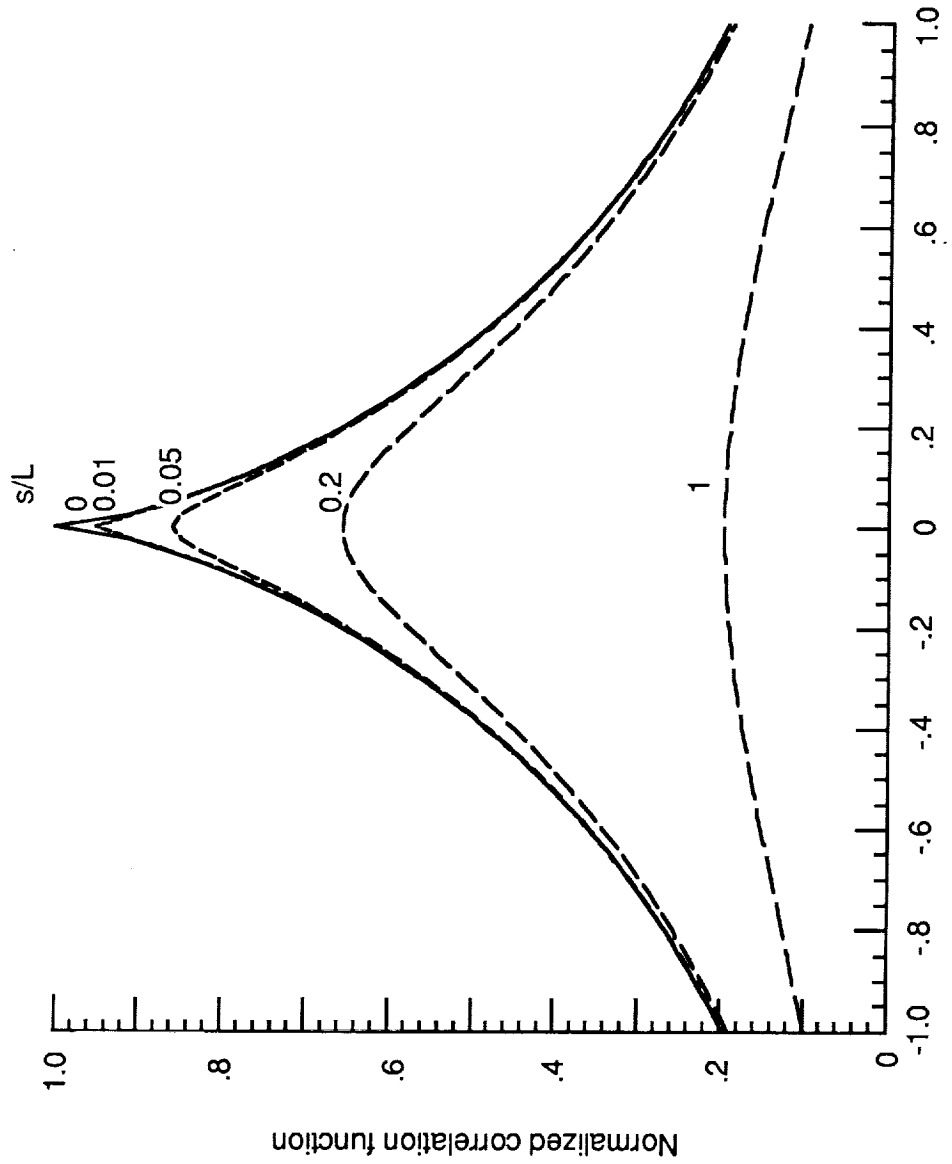

(b) Enlarged view of correlation function family.

Figure 4. Concluded.

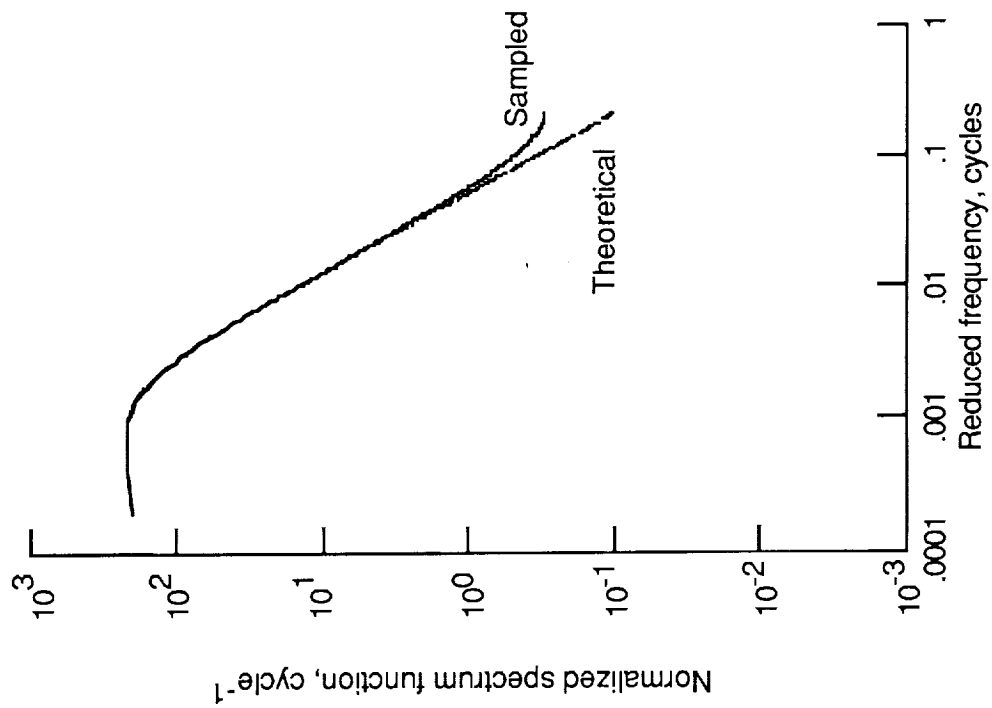

Figure 5. Von Kármán auto-spectrum function showing effect of sampling.

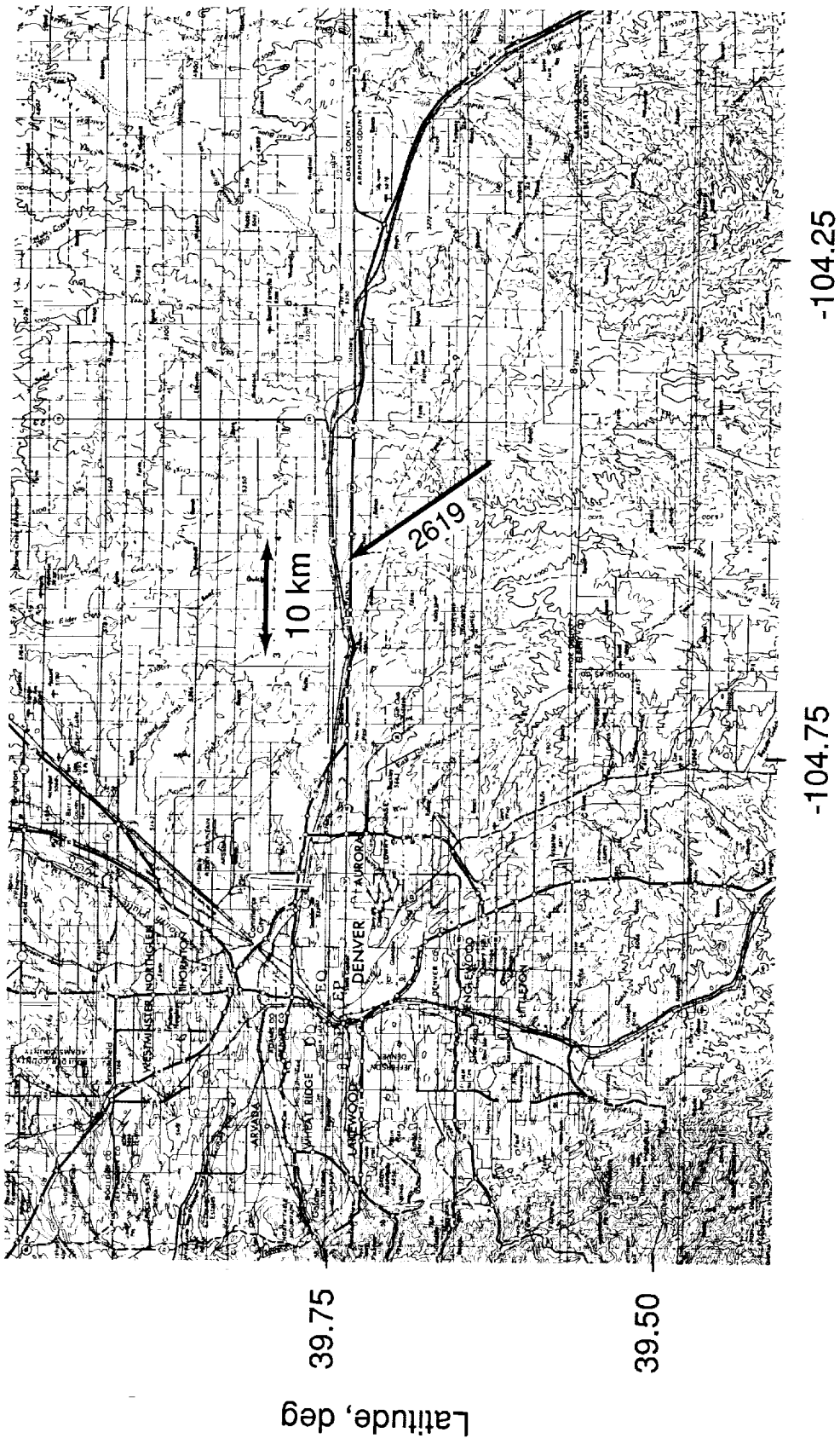

(a) Run 2619 near Denver, Colorado.

Figure 6. Maps showing flight tracks.

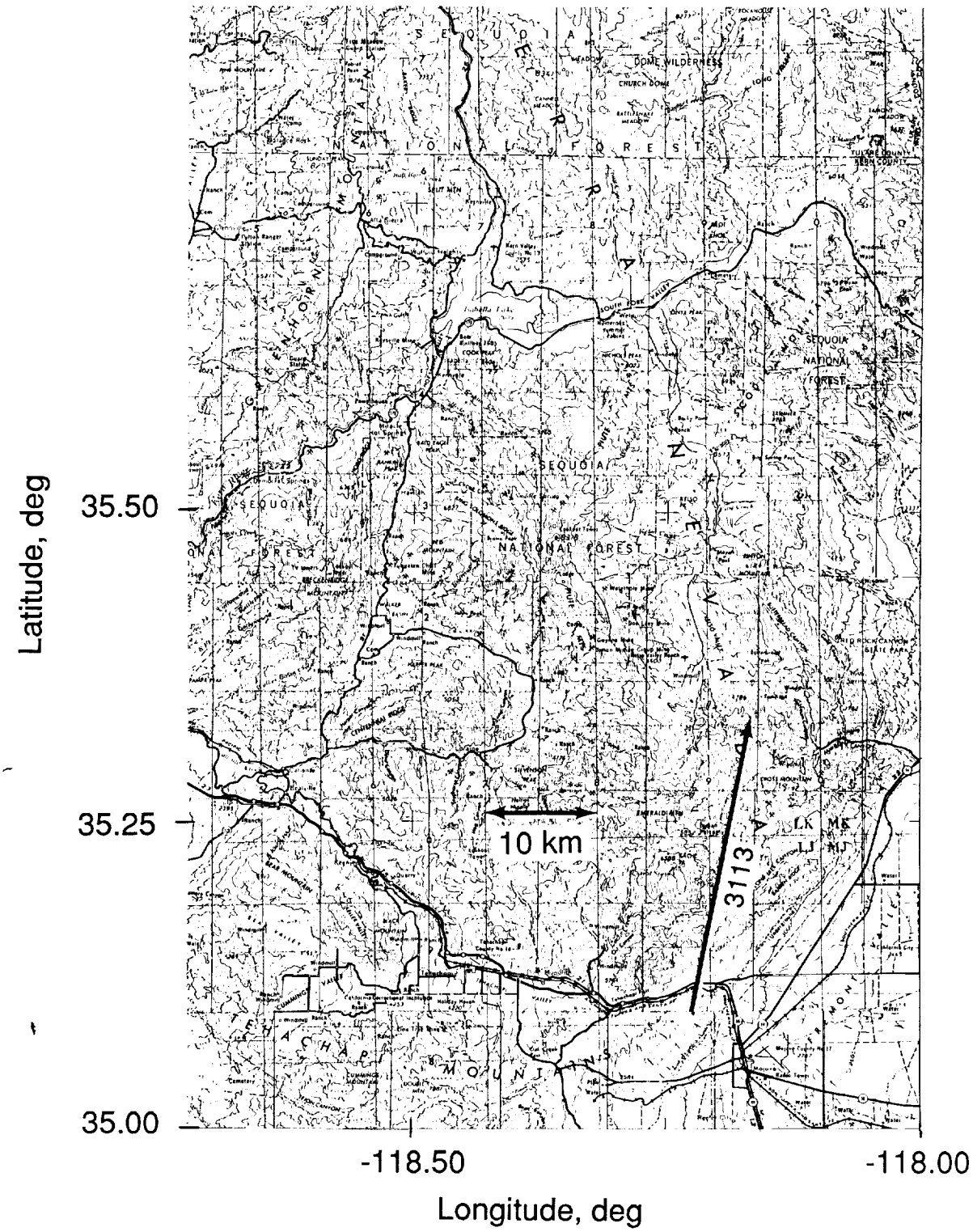

(b) Run 3113 near Mojave, California.

Figure 6. Continued.

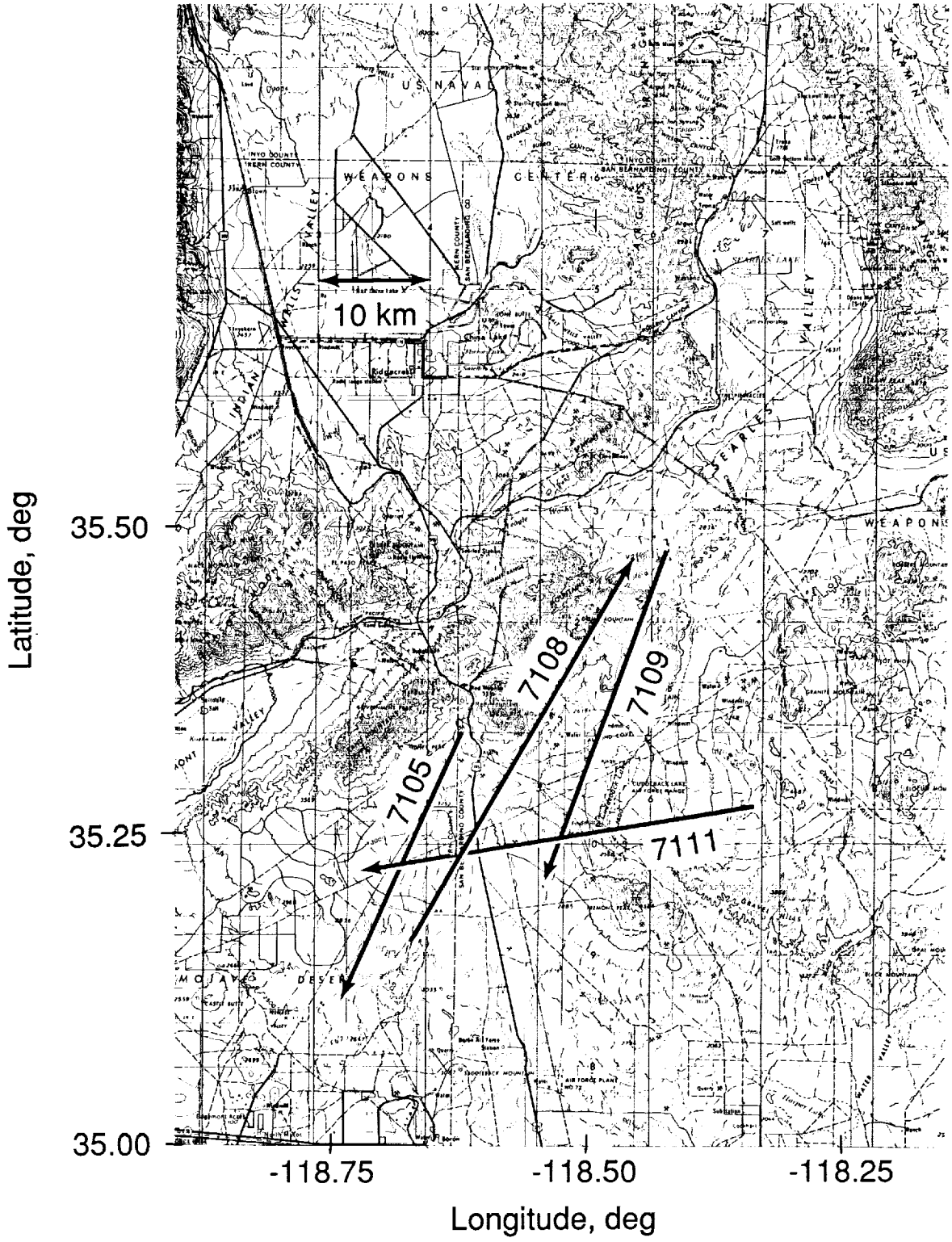

(c) Runs 7105, 7108, 7109, and 7111 near the Mojave Desert in California.

Figure 6. Concluded.

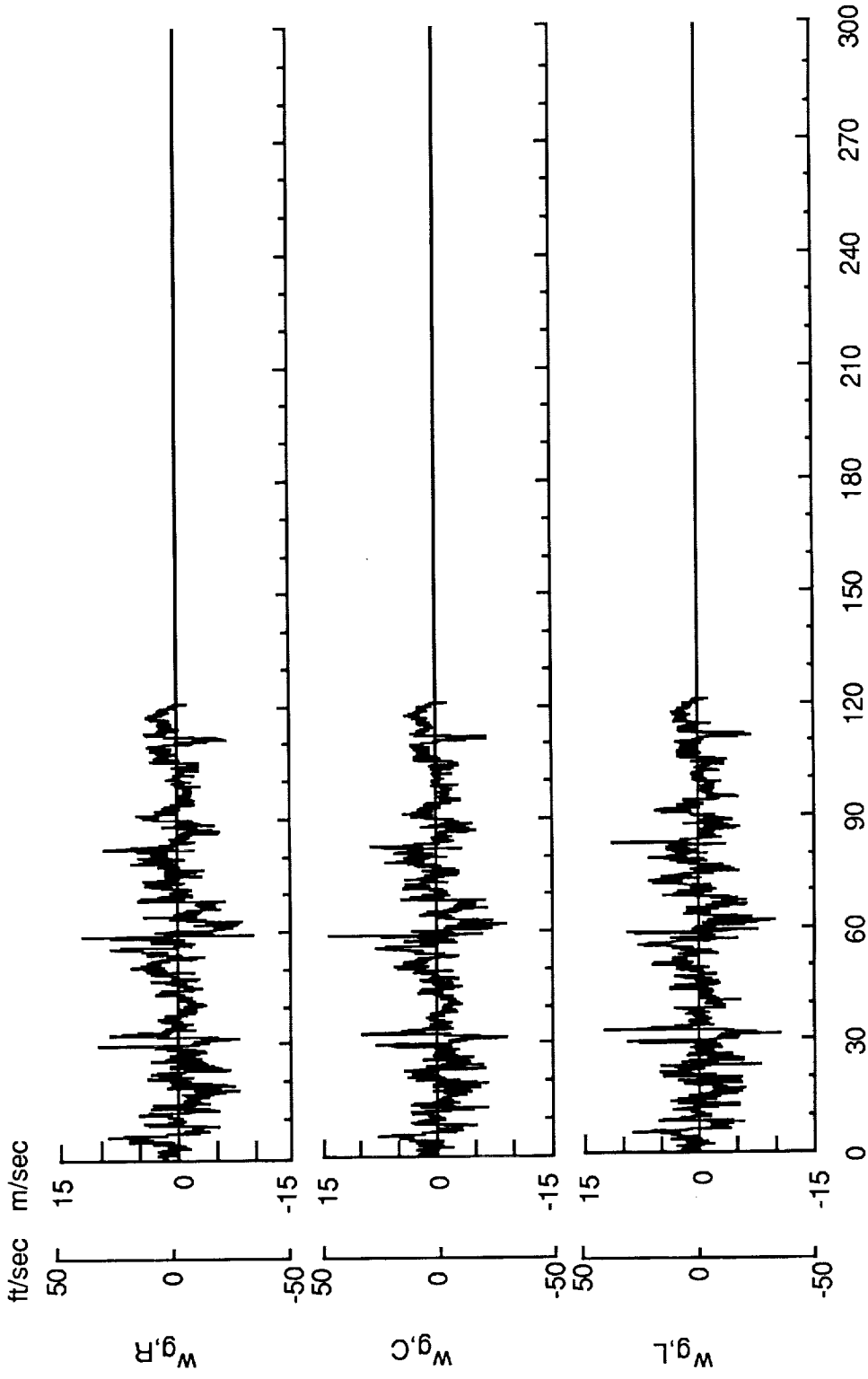

Figure 7. Vertical gust velocity time histories at right, center, and left probes for run 2619.

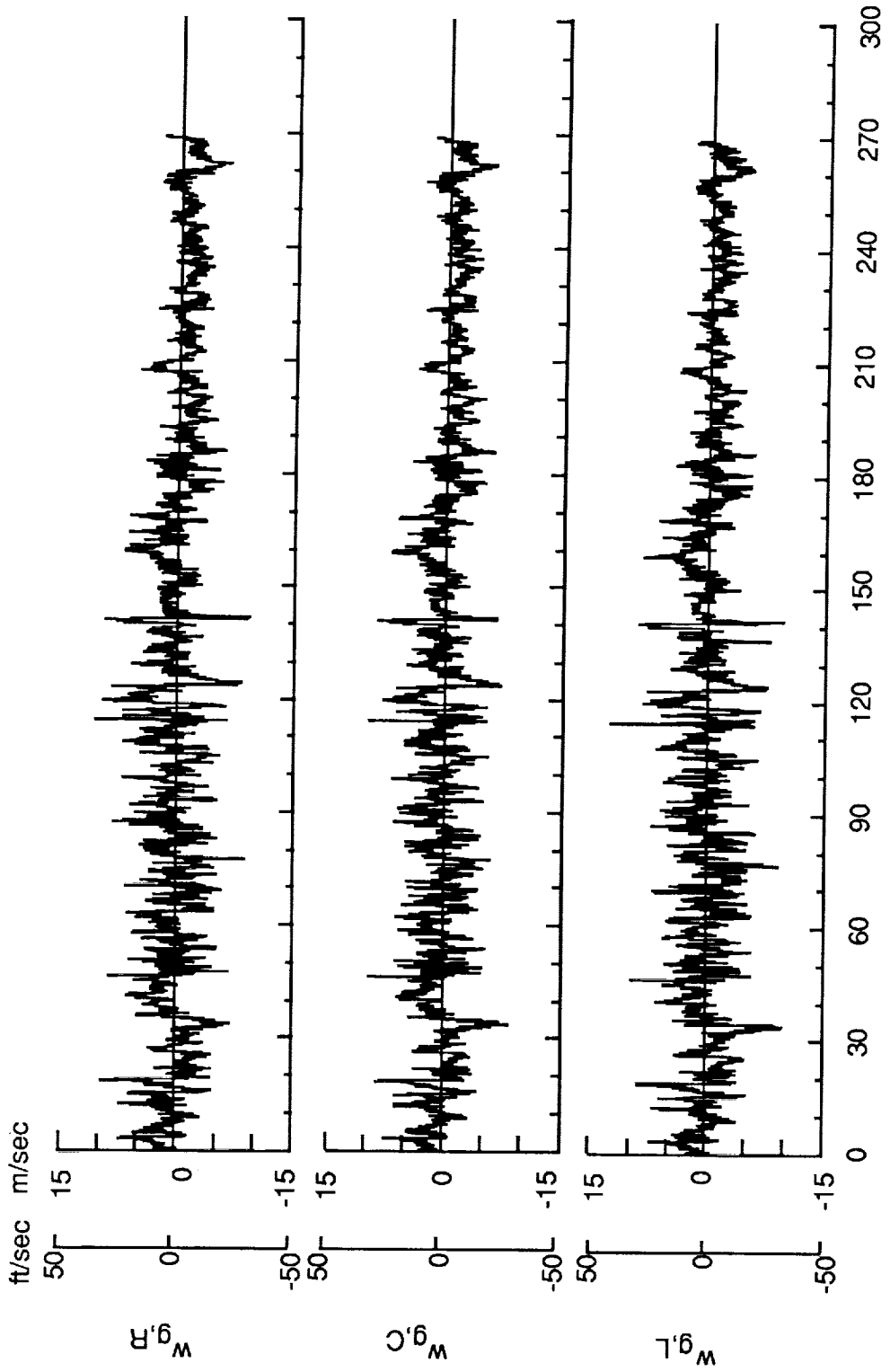

Figure 8. Vertical gust velocity time histories at right, center, and left probes for run 3113.

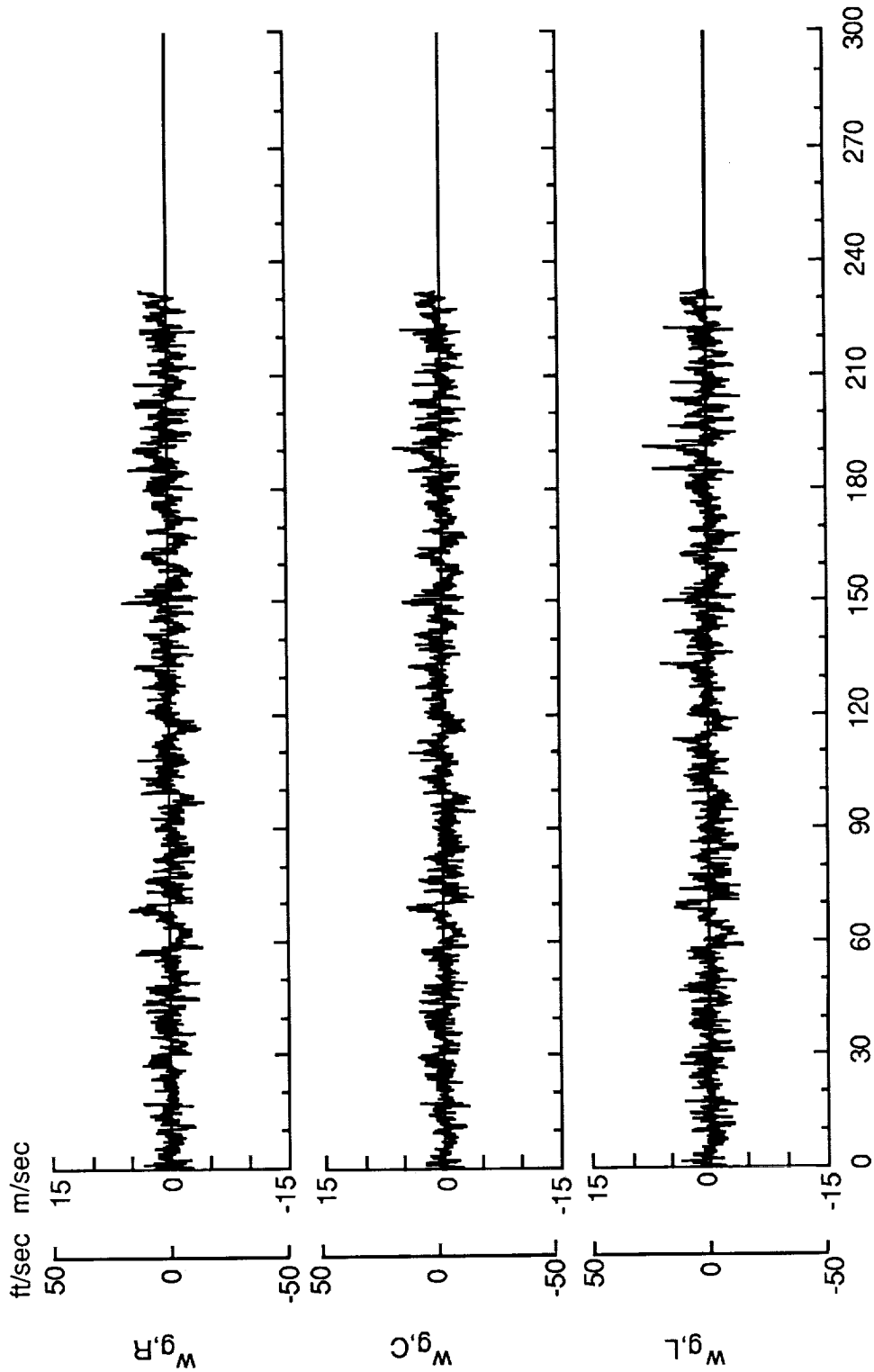

Figure 9. Vertical gust velocity time histories at right, center, and left probes for run 7105.

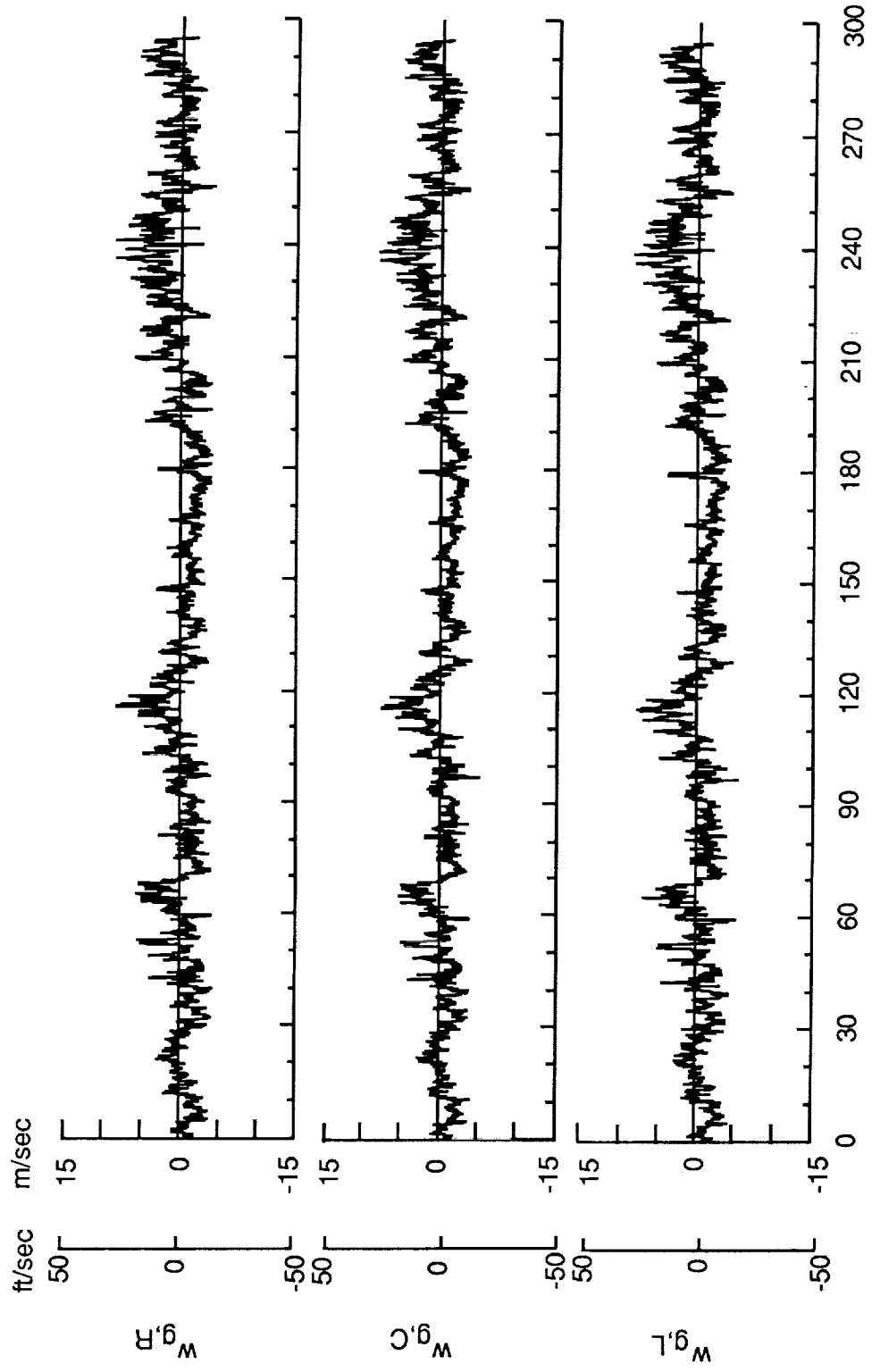

Figure 10. Vertical gust velocity time histories at right, center, and left probes for run 7108.

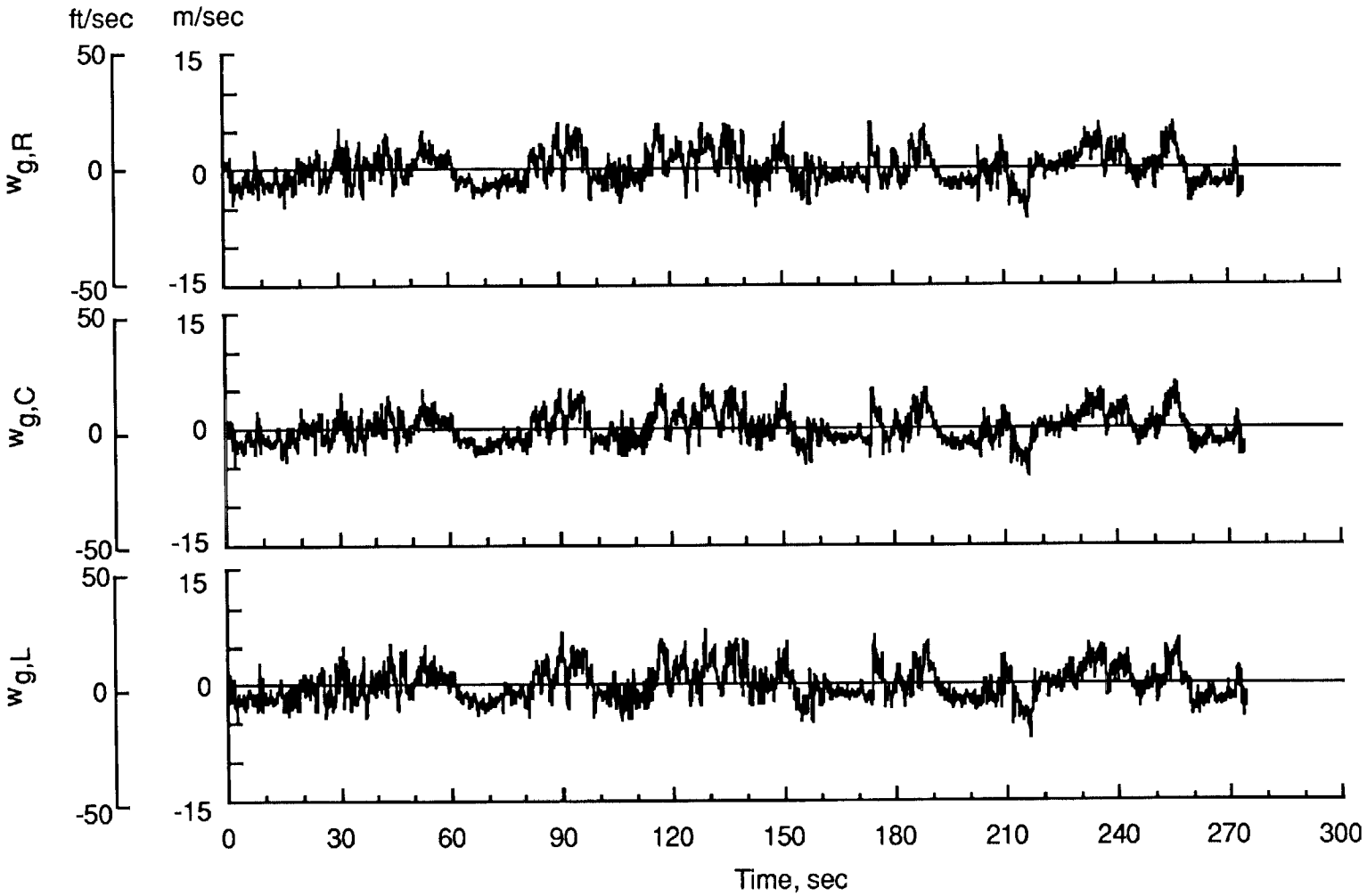

Figure 11. Vertical gust velocity time histories at right, center, and left probes for run 7109.

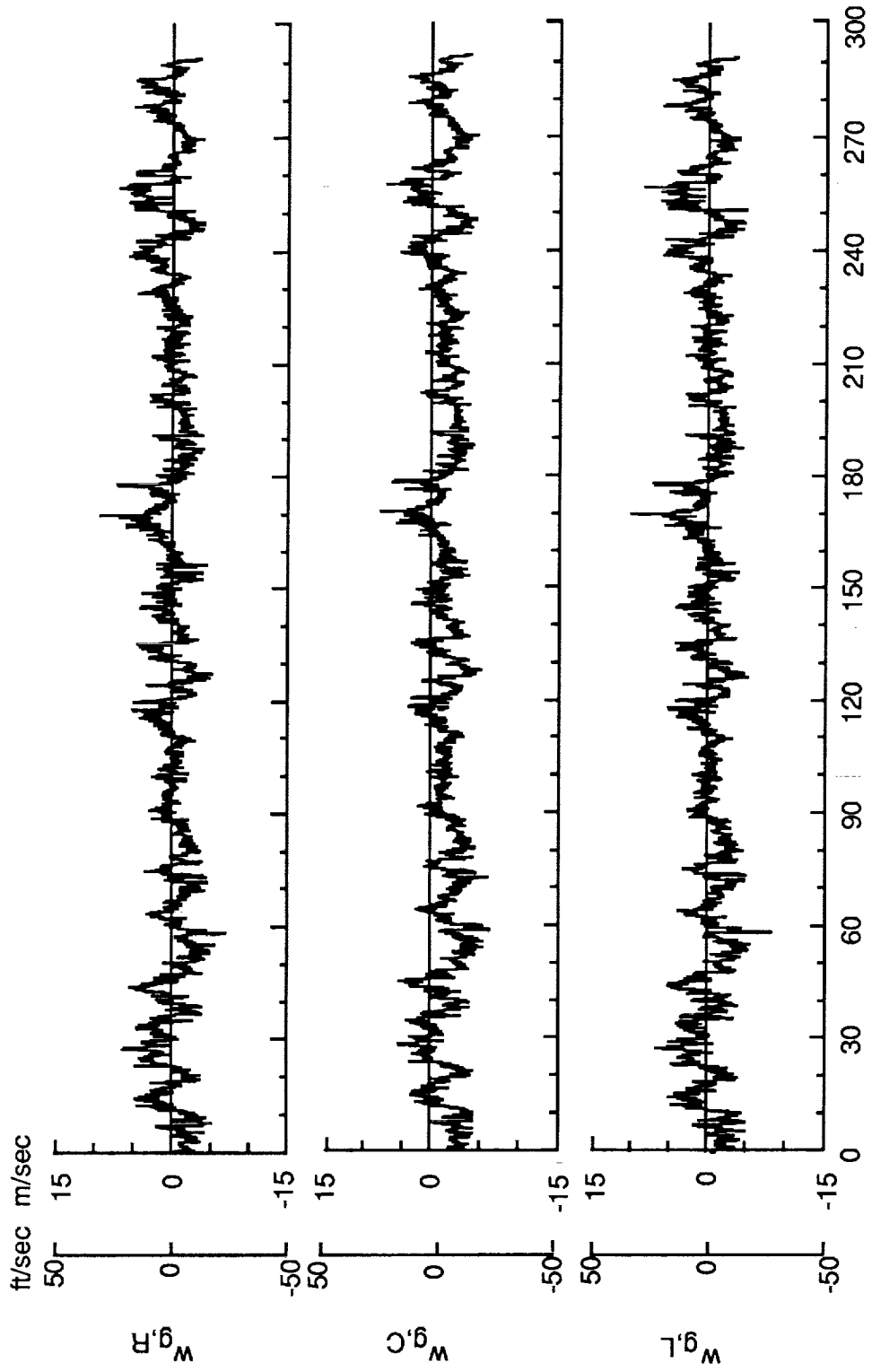

Figure 12. Vertical gust velocity time histories at right, center, and left probes for run 7111.

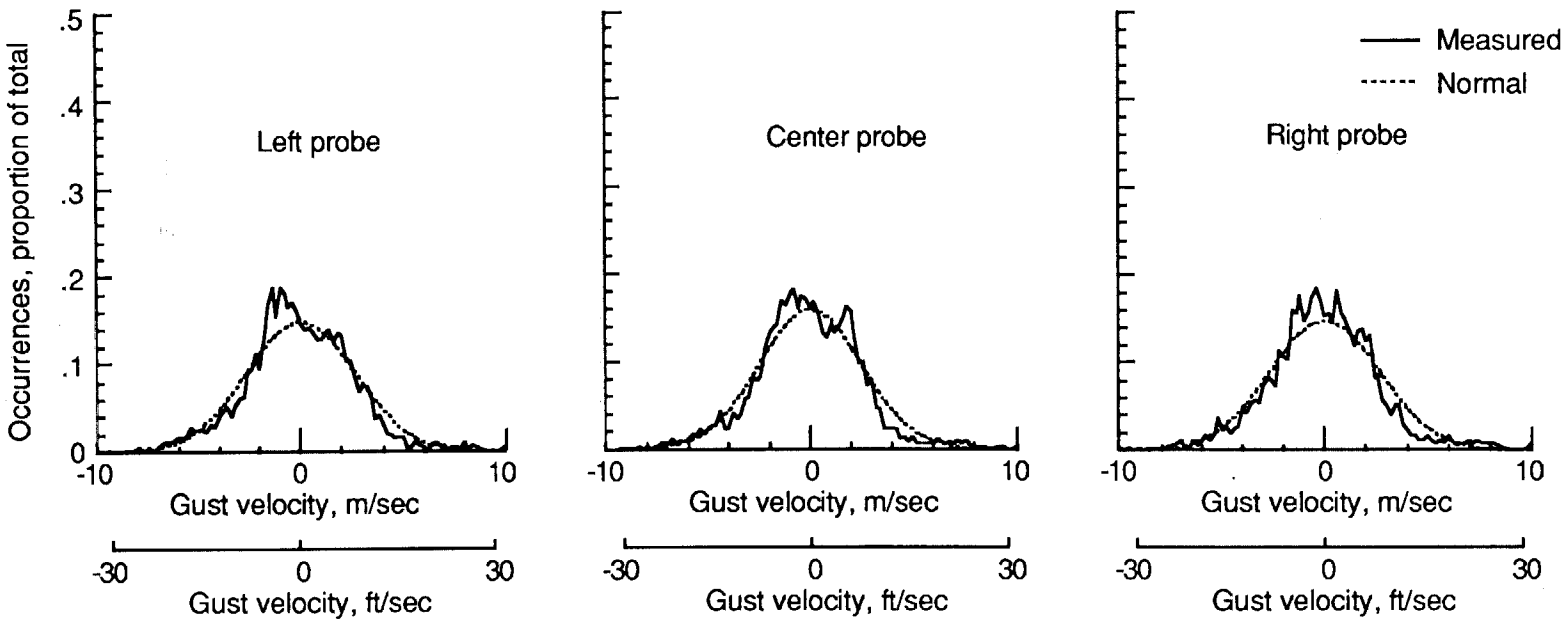

Figure 13. Vertical gust velocity distributions for left, center, and right probes for run 2619.

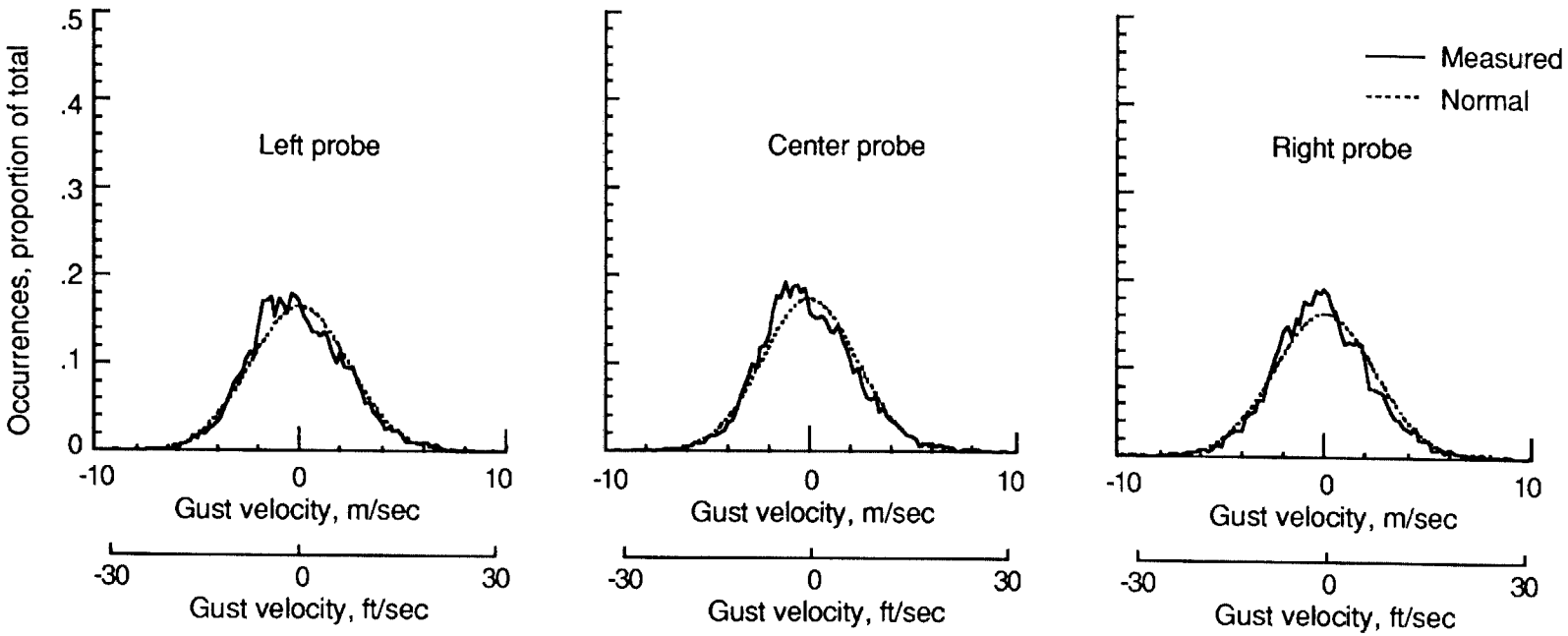

Figure 14. Vertical gust velocity distributions for left, center, and right probes for run 3113.

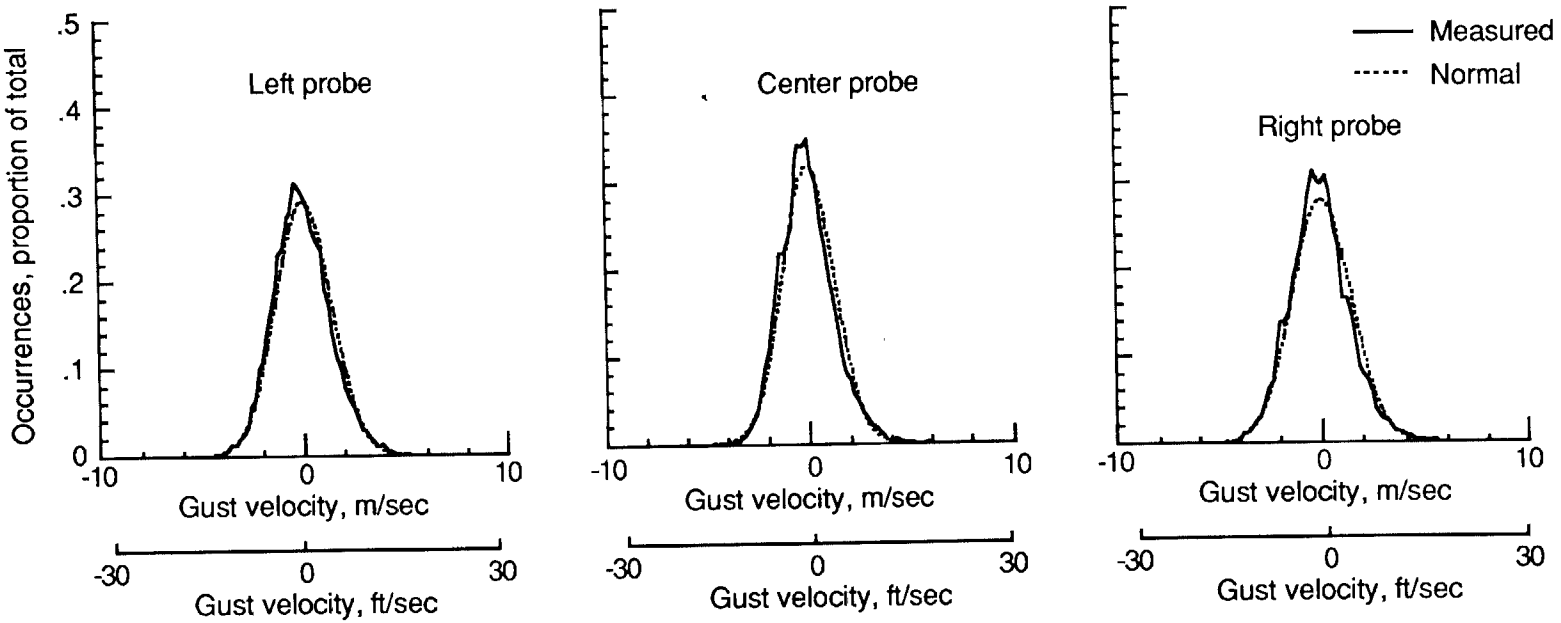

Figure 15. Vertical gust velocity distributions for left, center, and right probes for run 7105.

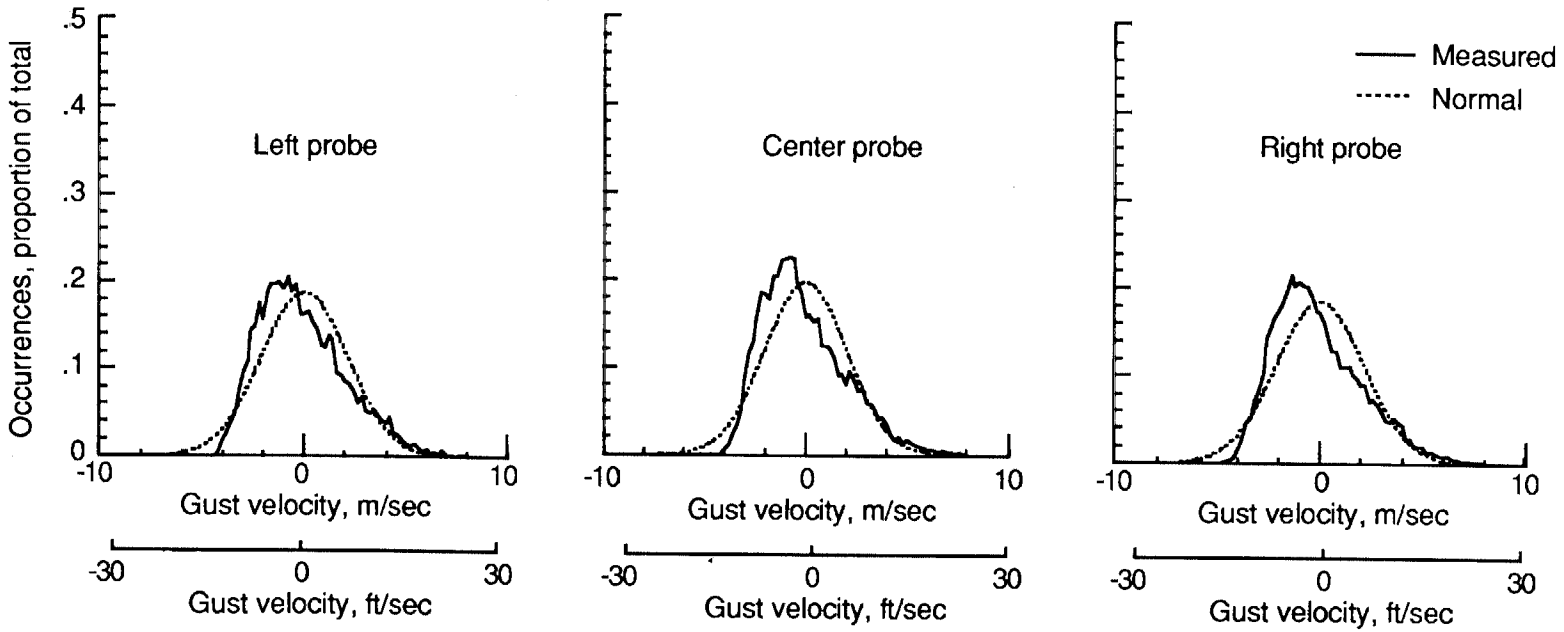

Figure 16. Vertical gust velocity distributions for left, center, and right probes for run 7108.

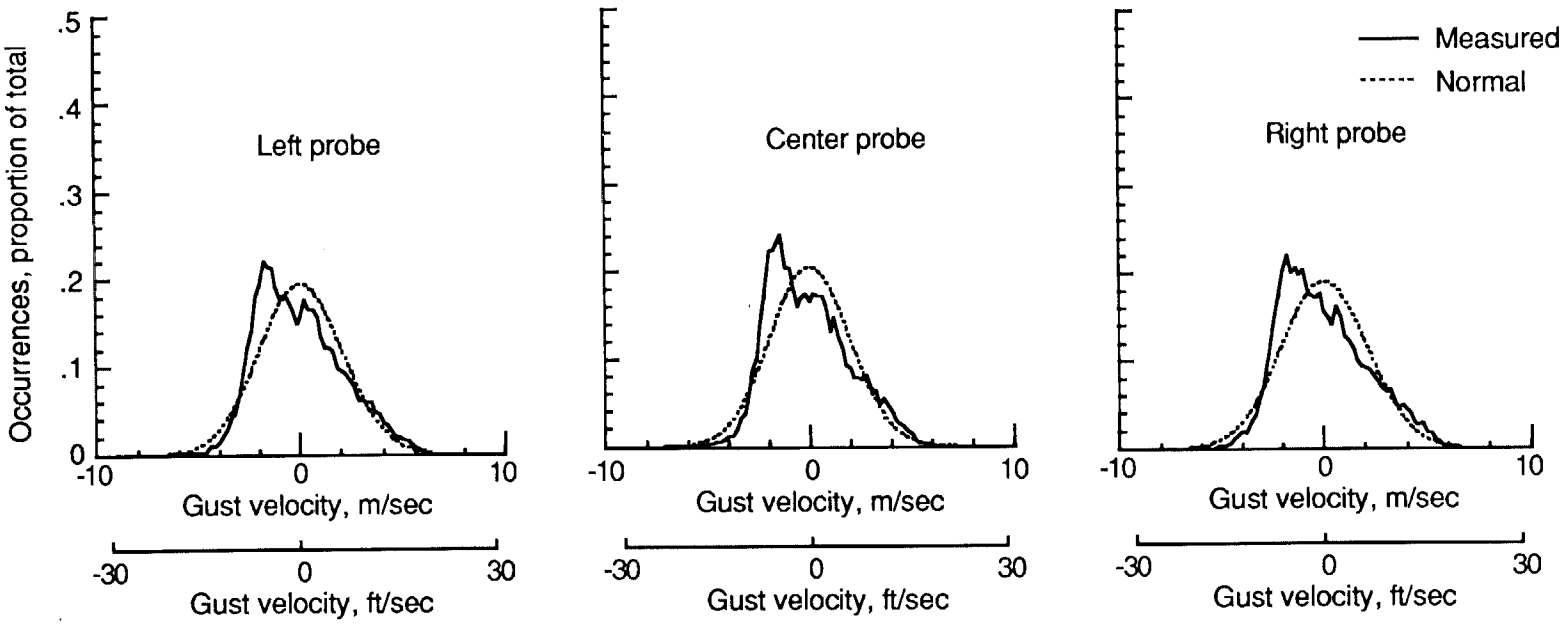

Figure 17. Vertical gust velocity distributions for left, center, and right probes for run 7109.

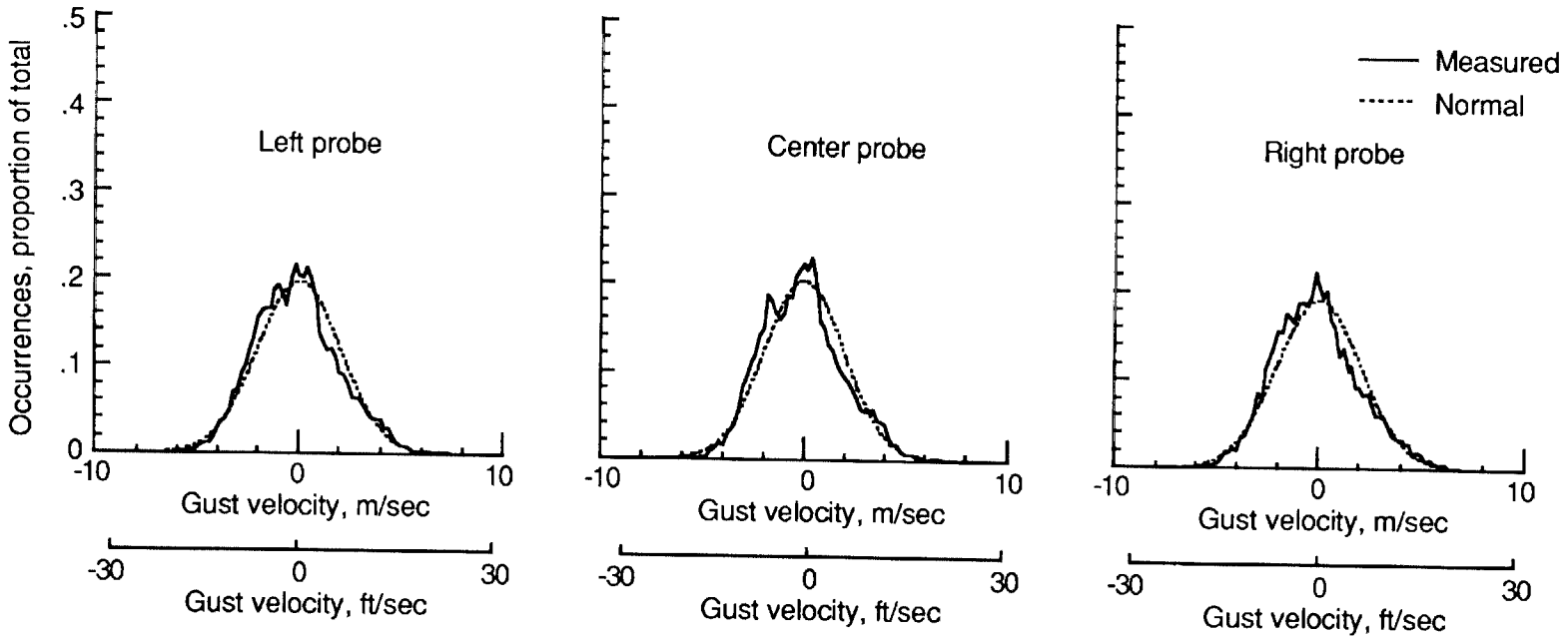

Figure 18. Vertical gust velocity distributions for left, center, and right probes for run 7111.

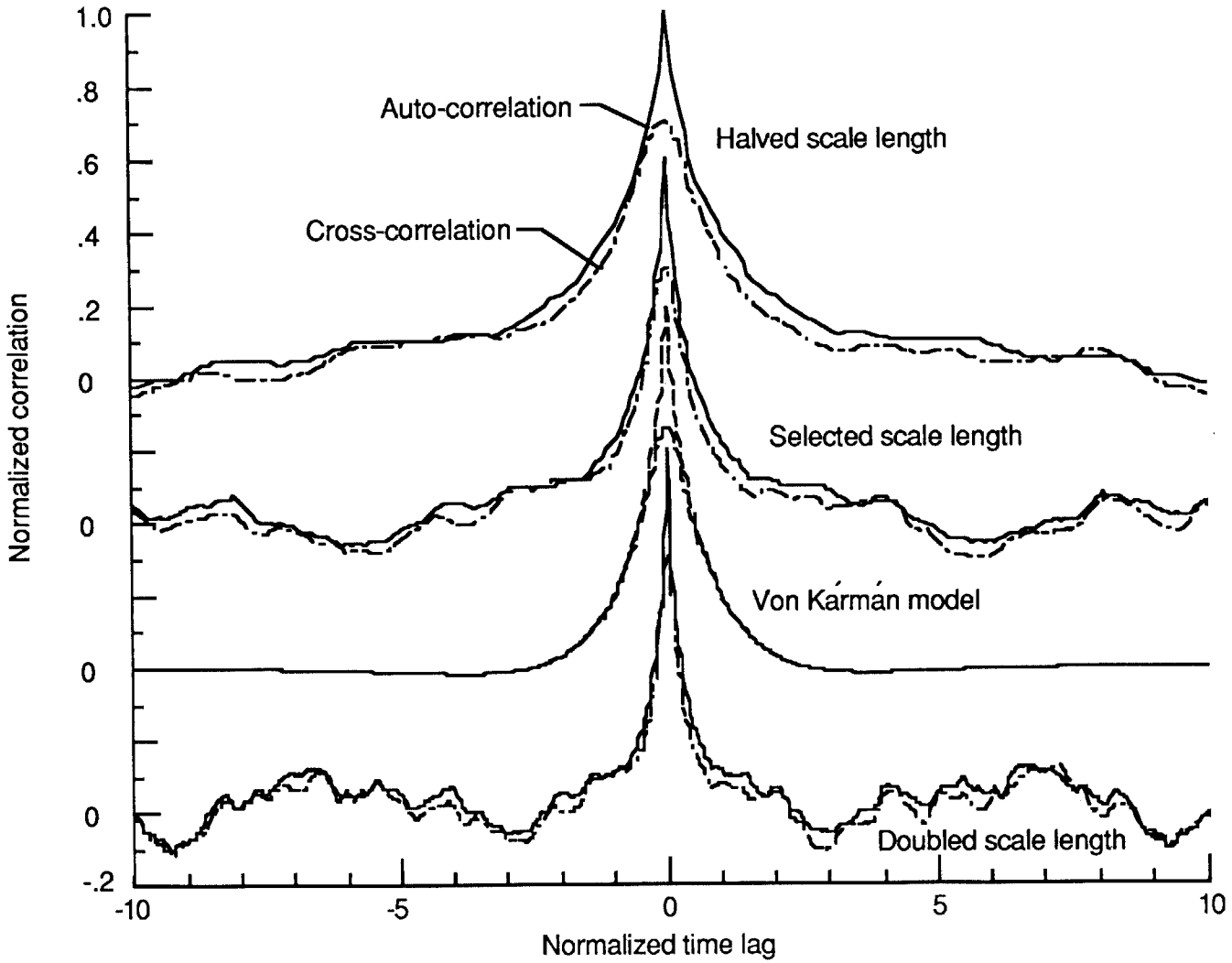

(a) Correlations.

Figure 19. Correlation and spectral estimates for three integral scale lengths for run 7105.

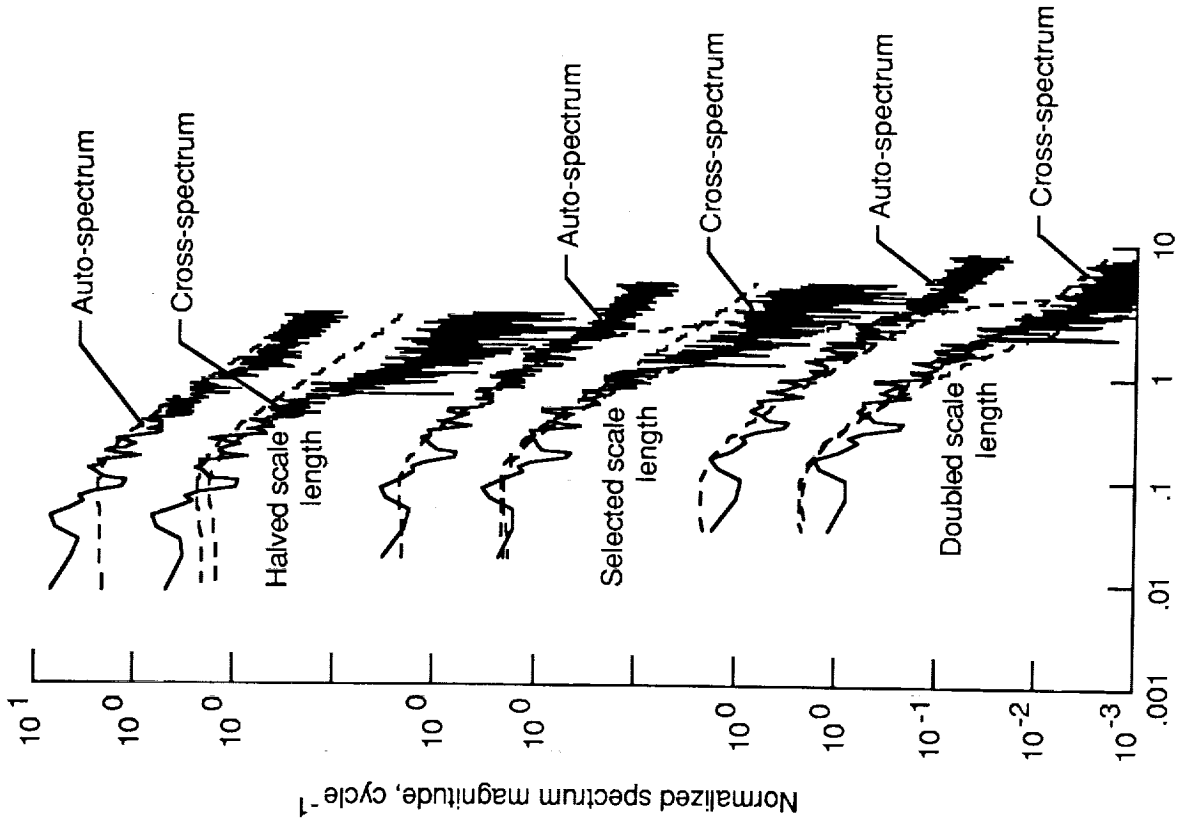

(b) Spectra.

Figure 19. Concluded.

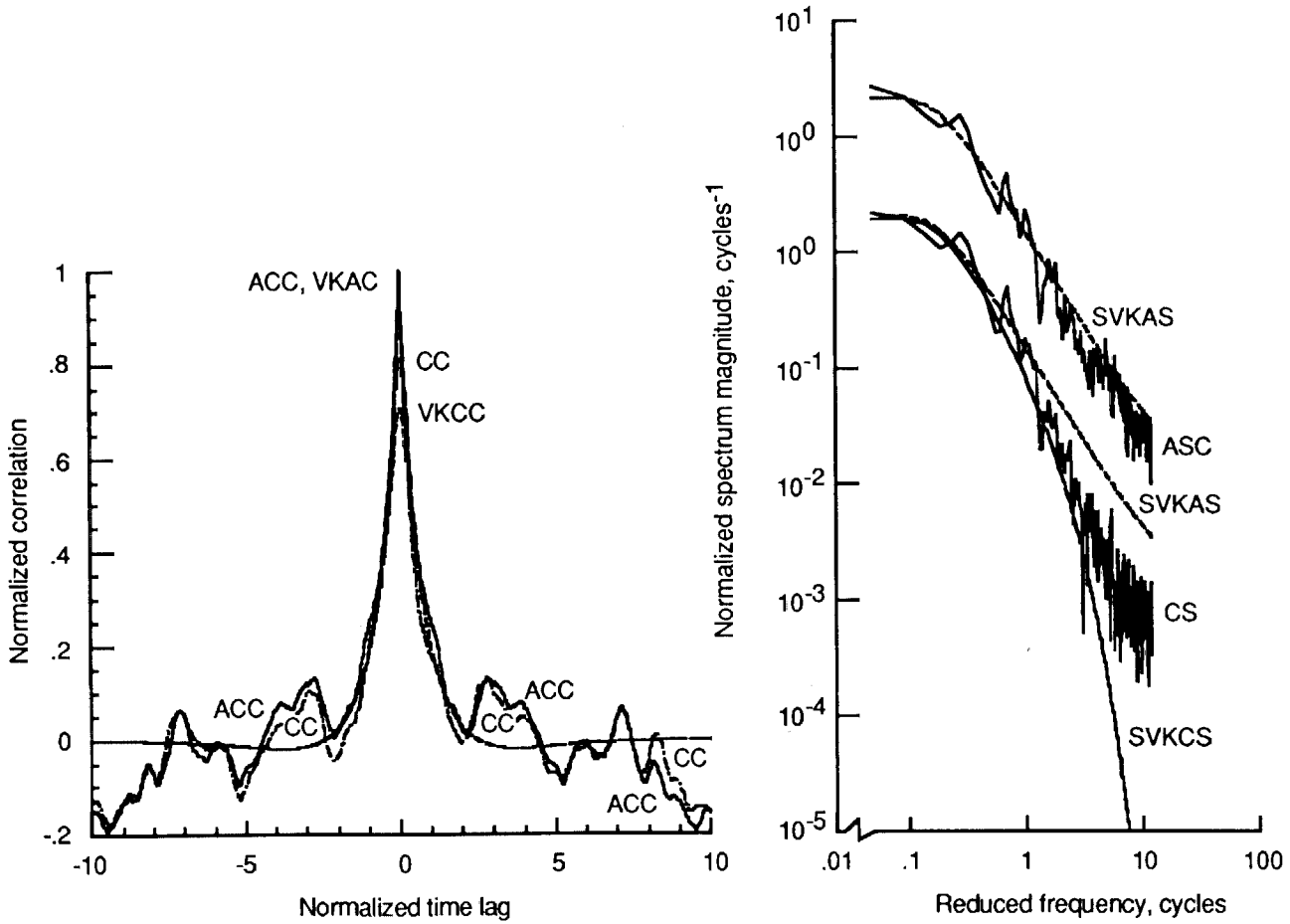

(a) Correlations and spectrum magnitudes at center and across span.

Figure 20. Spectral estimates and functions for run 2619.

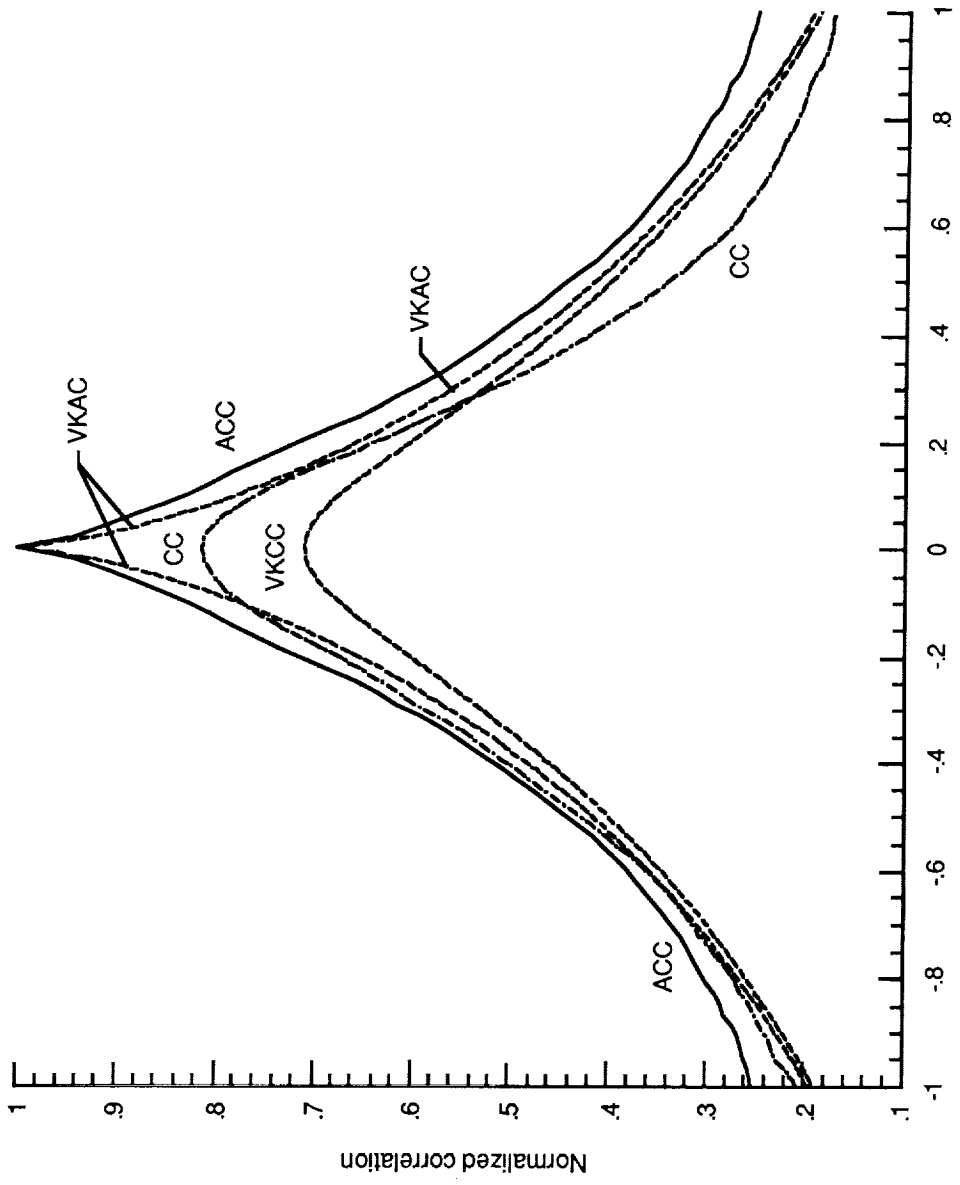

(b) Enlarged view of correlation estimates and functions.

Figure 20. Concluded.

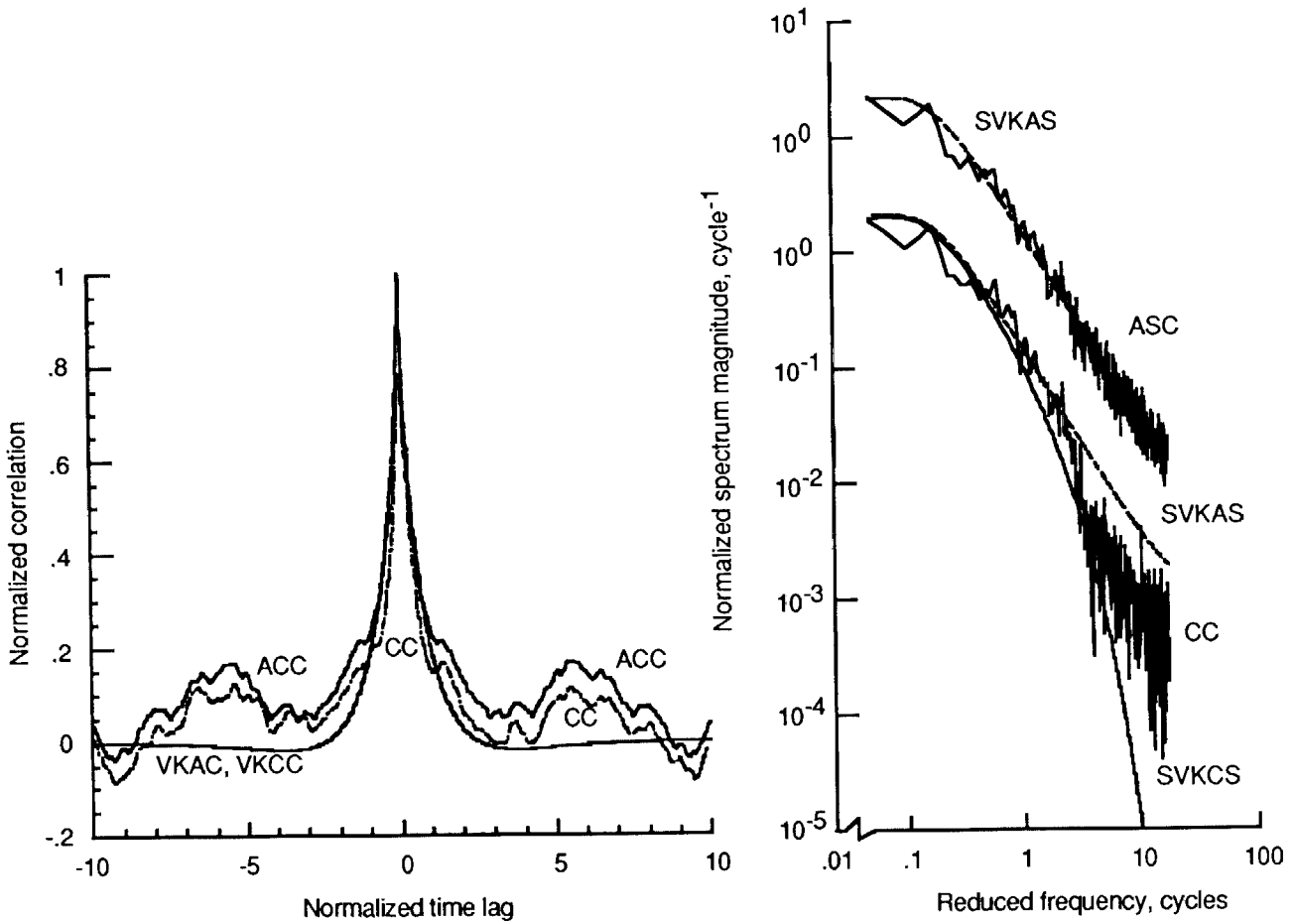

(a) Correlations and spectrum magnitudes at center and across wing span.

Figure 21. Spectral estimates and functions for run 3113.

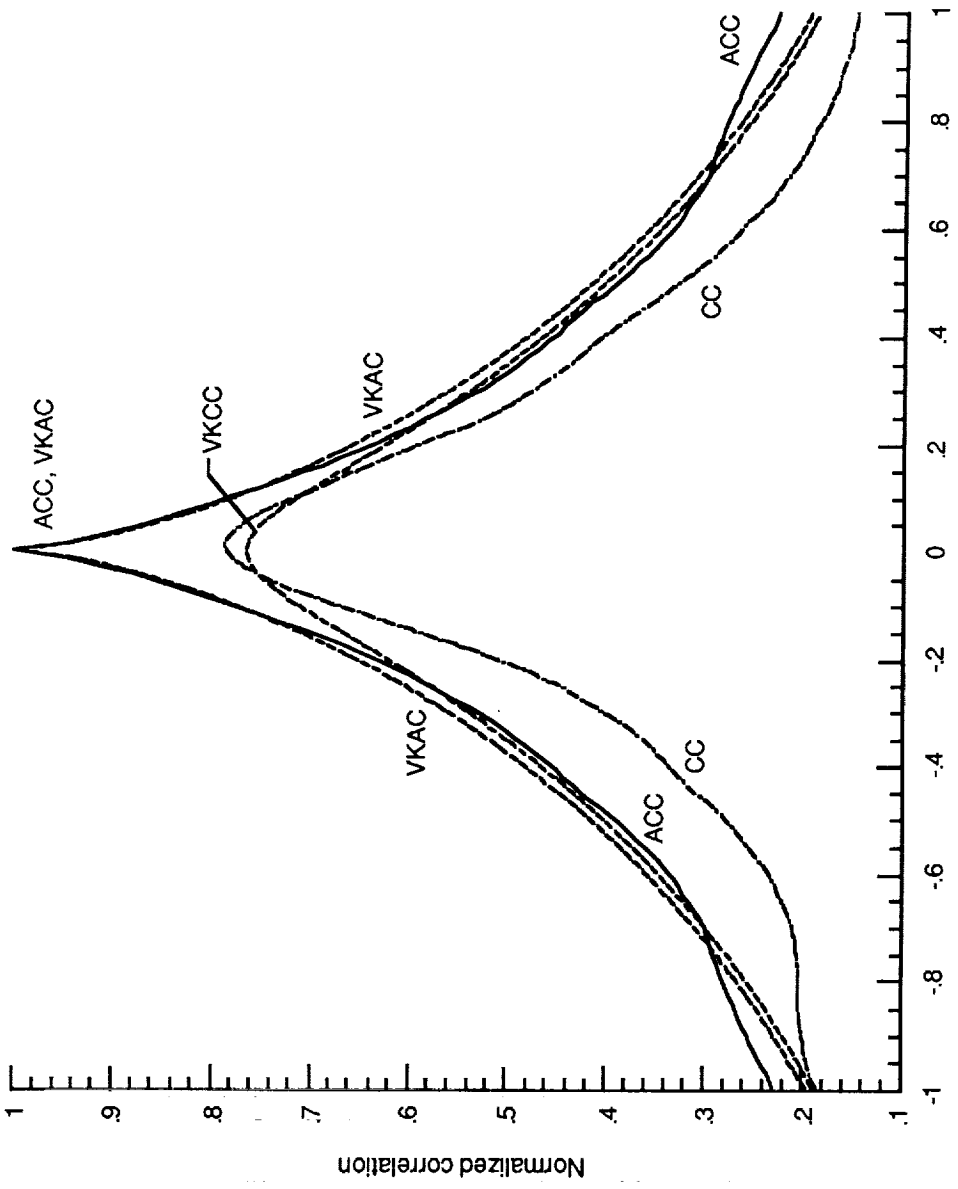

(b) Enlarged view of correlation estimates and functions.

Figure 21. Concluded.

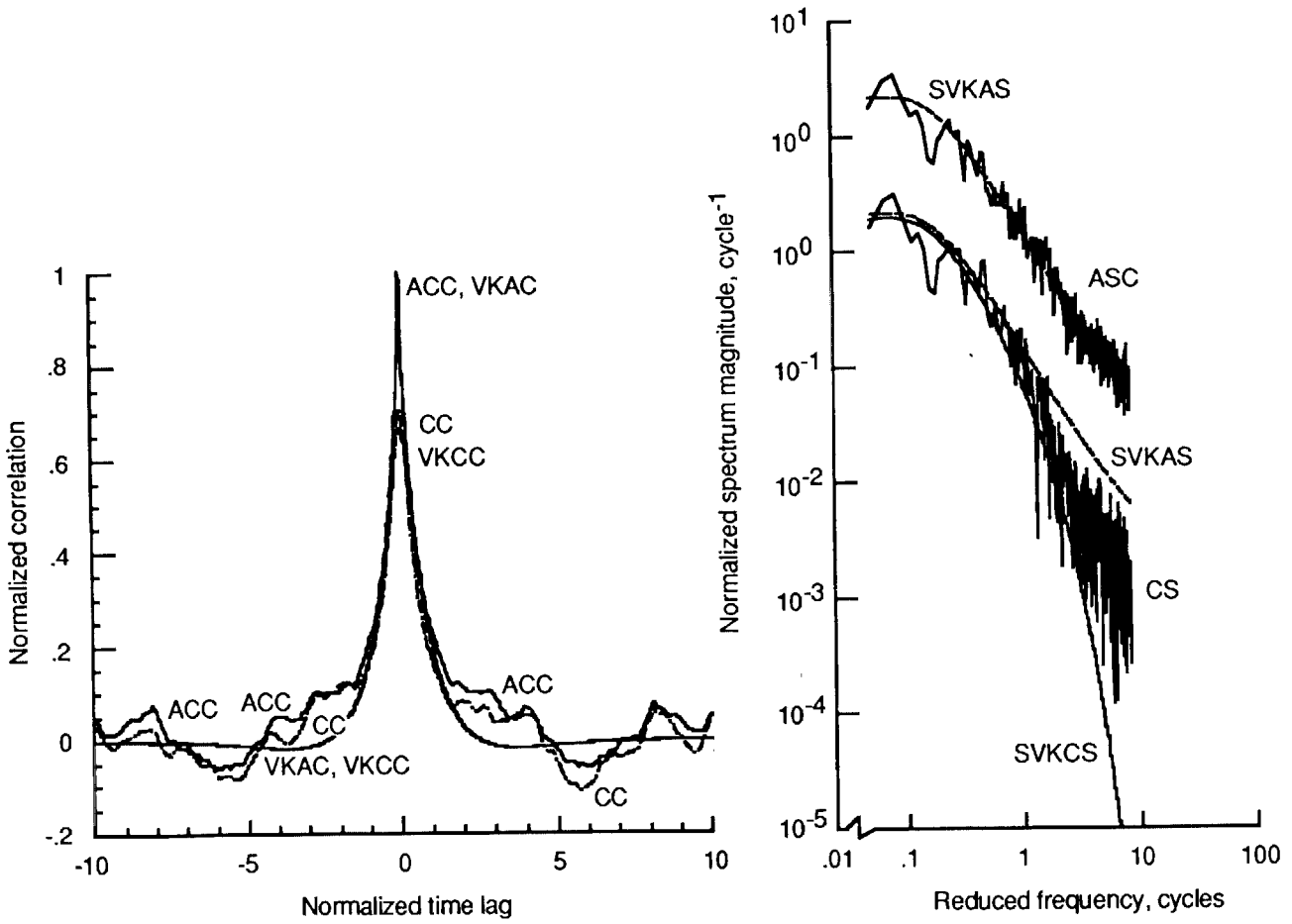

(a) Correlations and spectrum magnitudes at center and across wing span.

Figure 22. Spectral estimates and functions for run 7105.

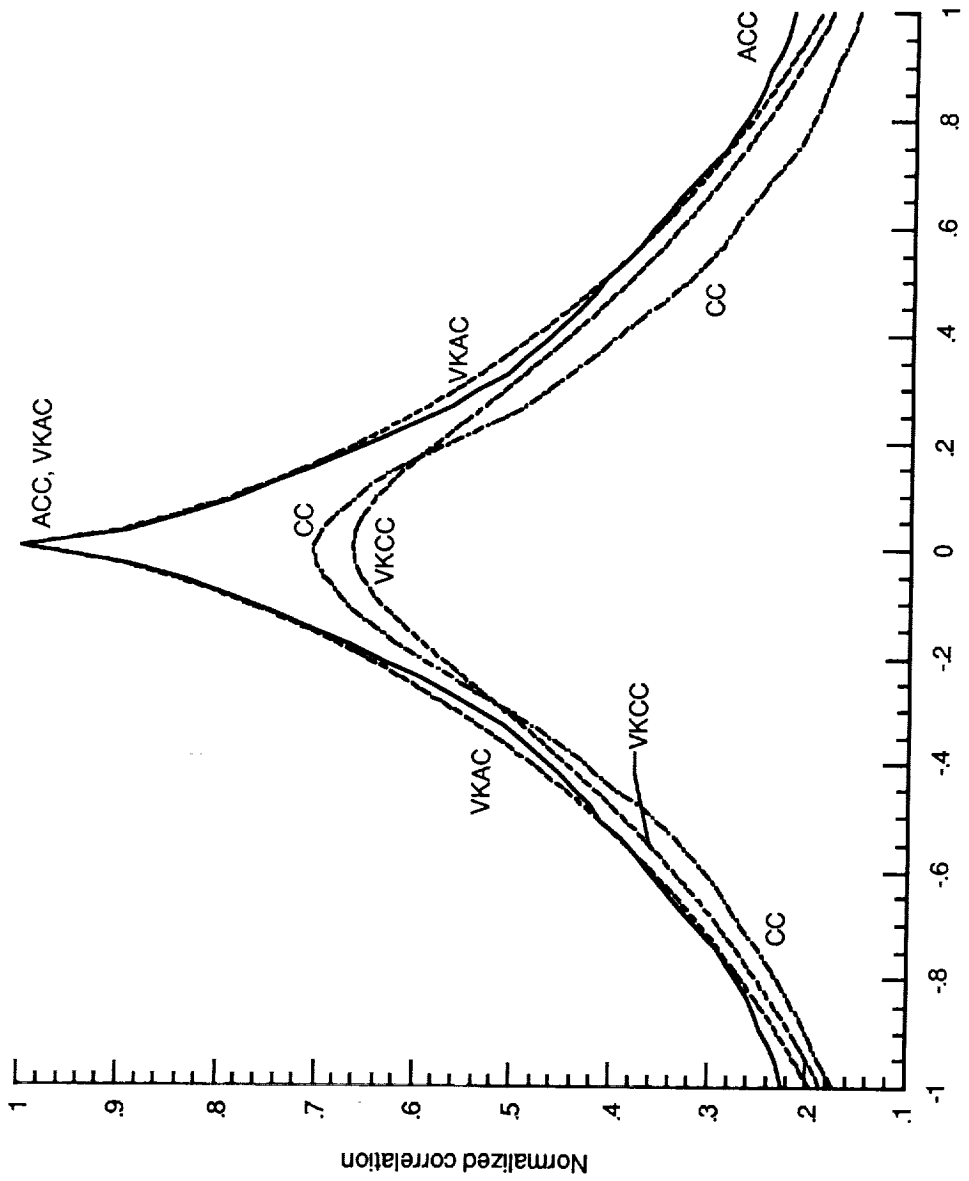

(b) Enlarged view of correlation estimates and functions.

Figure 22. Concluded.

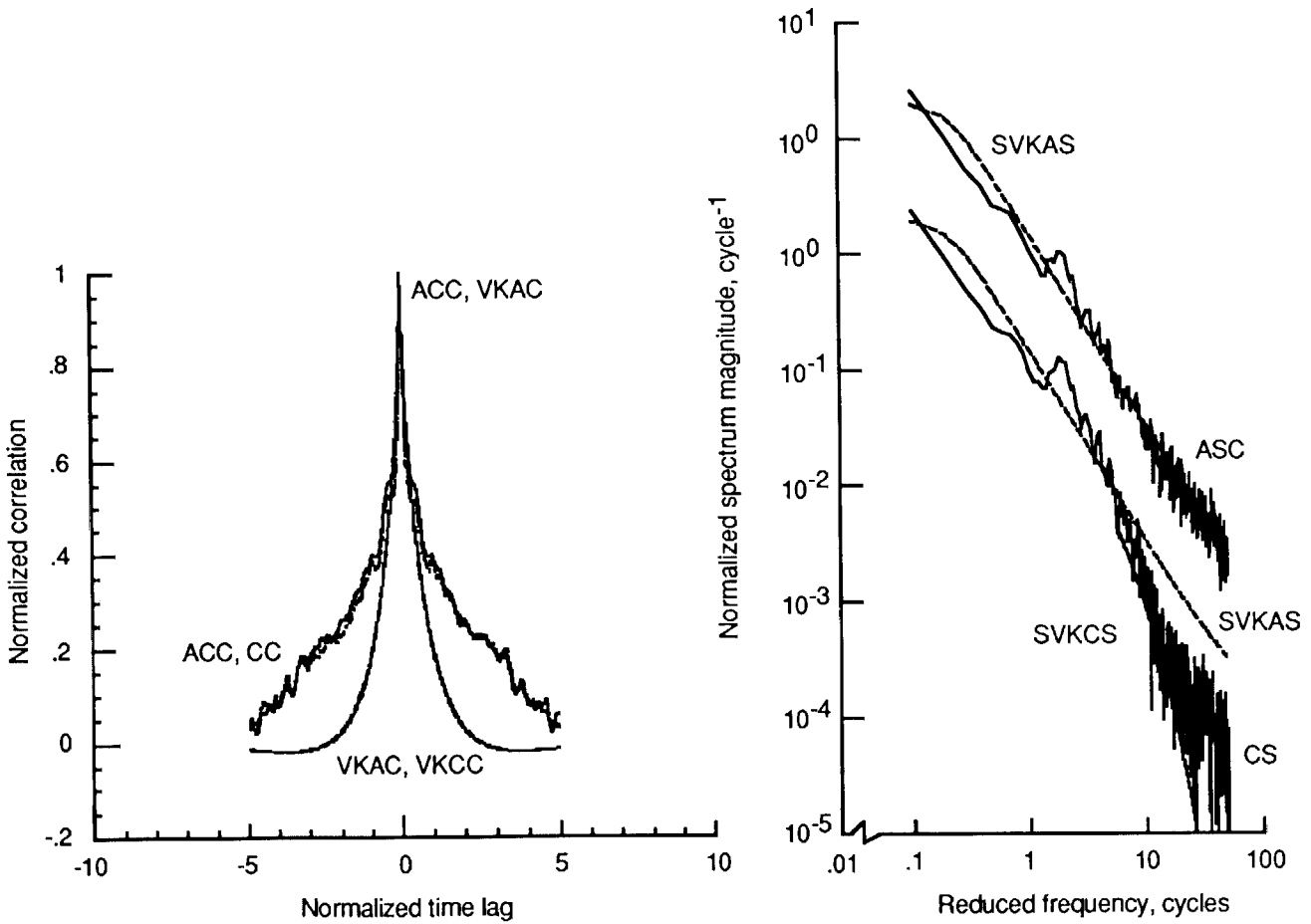

(a) Correlations and spectrum magnitudes at center and across wing span.

Figure 23. Spectral estimates and functions for run 7108.

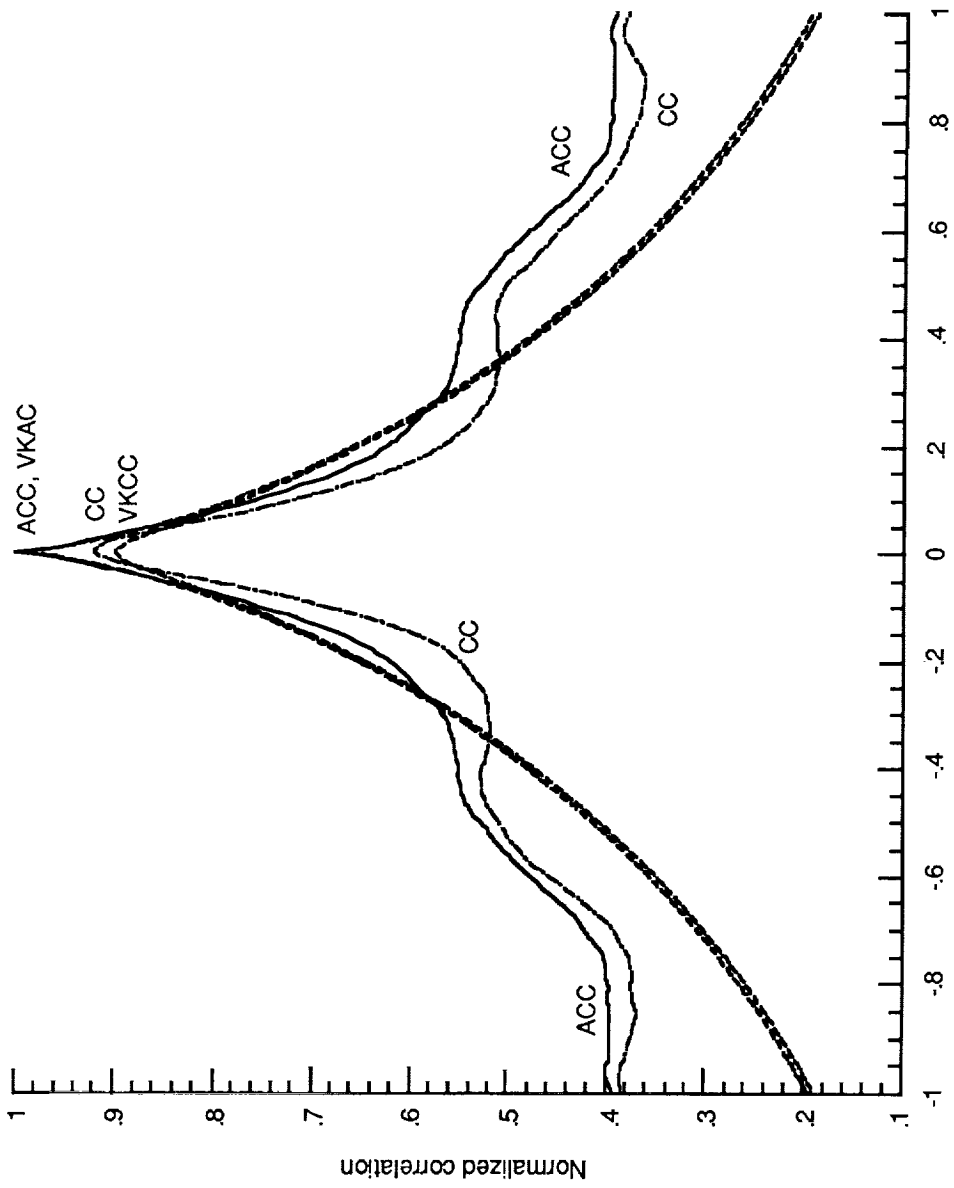

(b) Enlarged view of correlation estimates and functions.

Figure 23. Concluded.

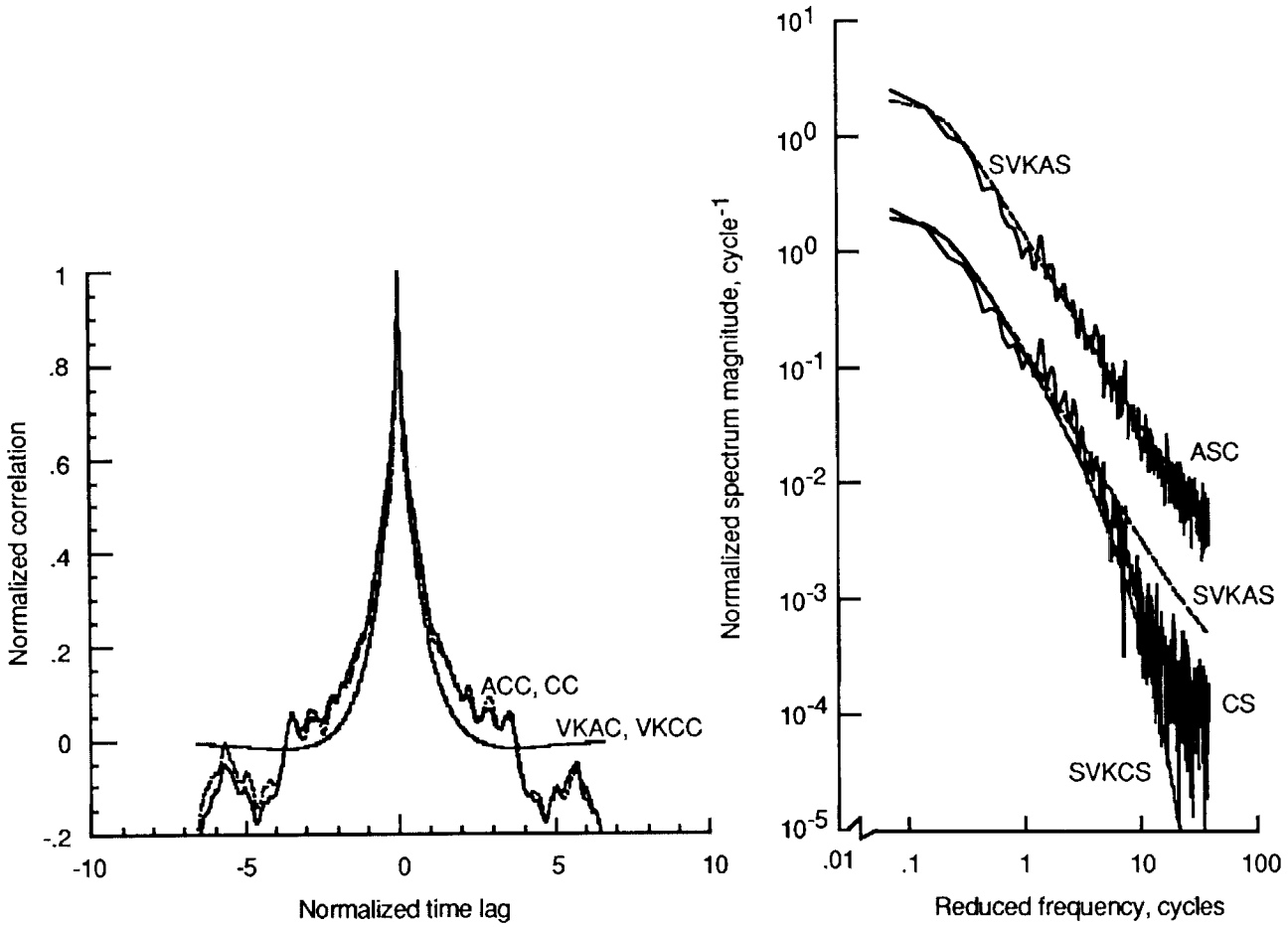

(a) Correlations and spectrum magnitudes at center and across wing span.

Figure 24. Spectral estimates and functions for run 7109.

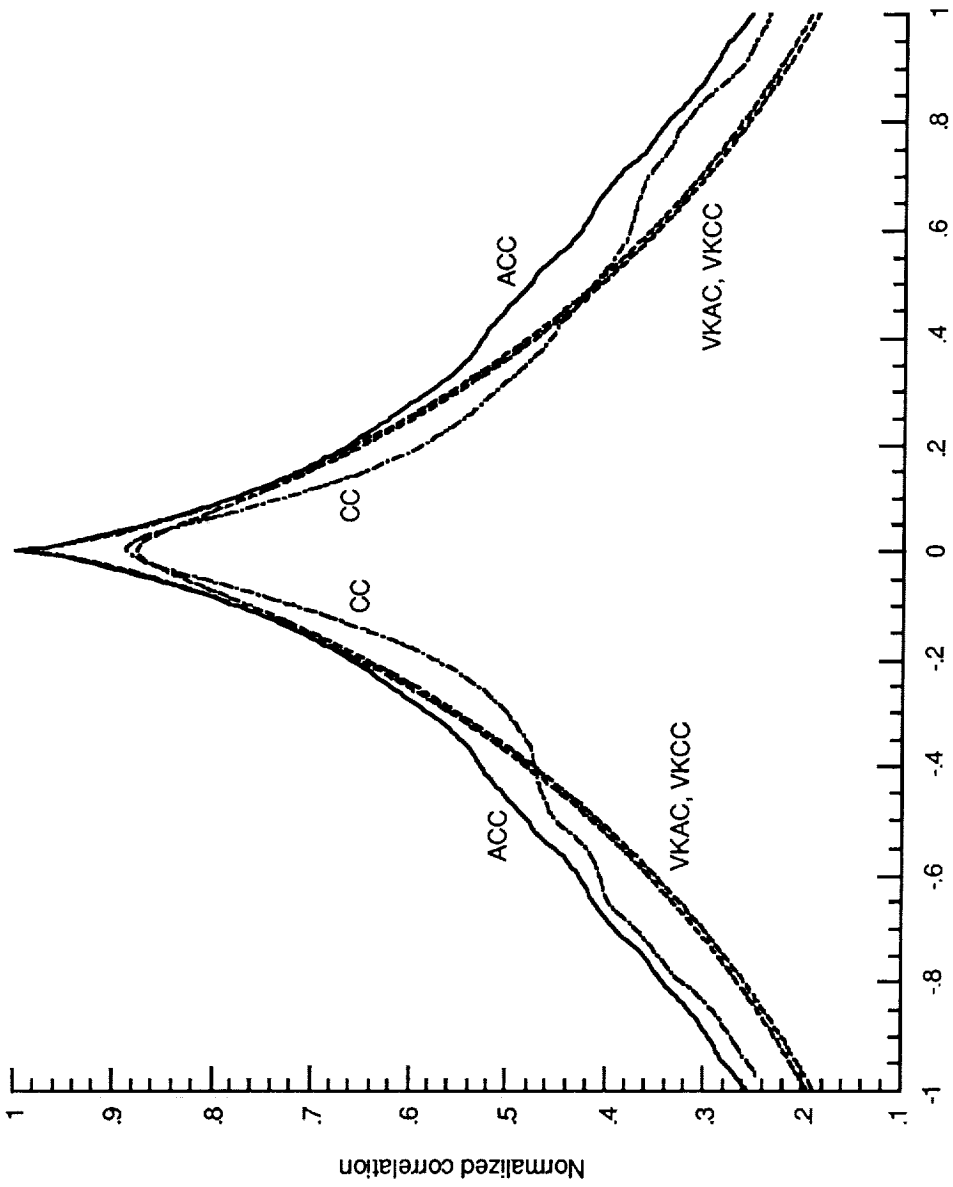

(b) Enlarged view of correlation estimates and functions.

Figure 24. Concluded.

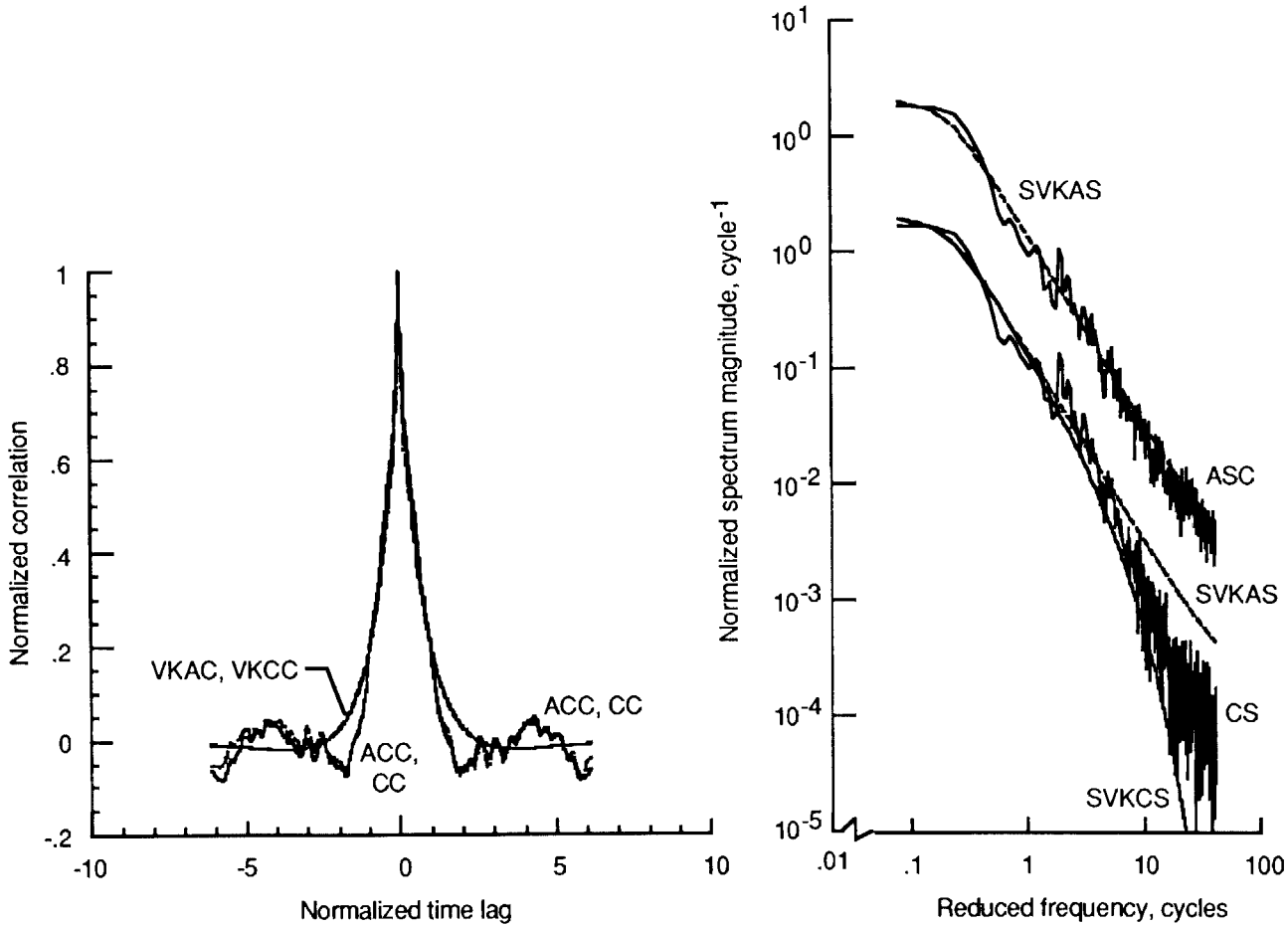

(a) Correlations and spectrum magnitudes at center and across wing span.

Figure 25. Spectral estimates and functions for run 7111.

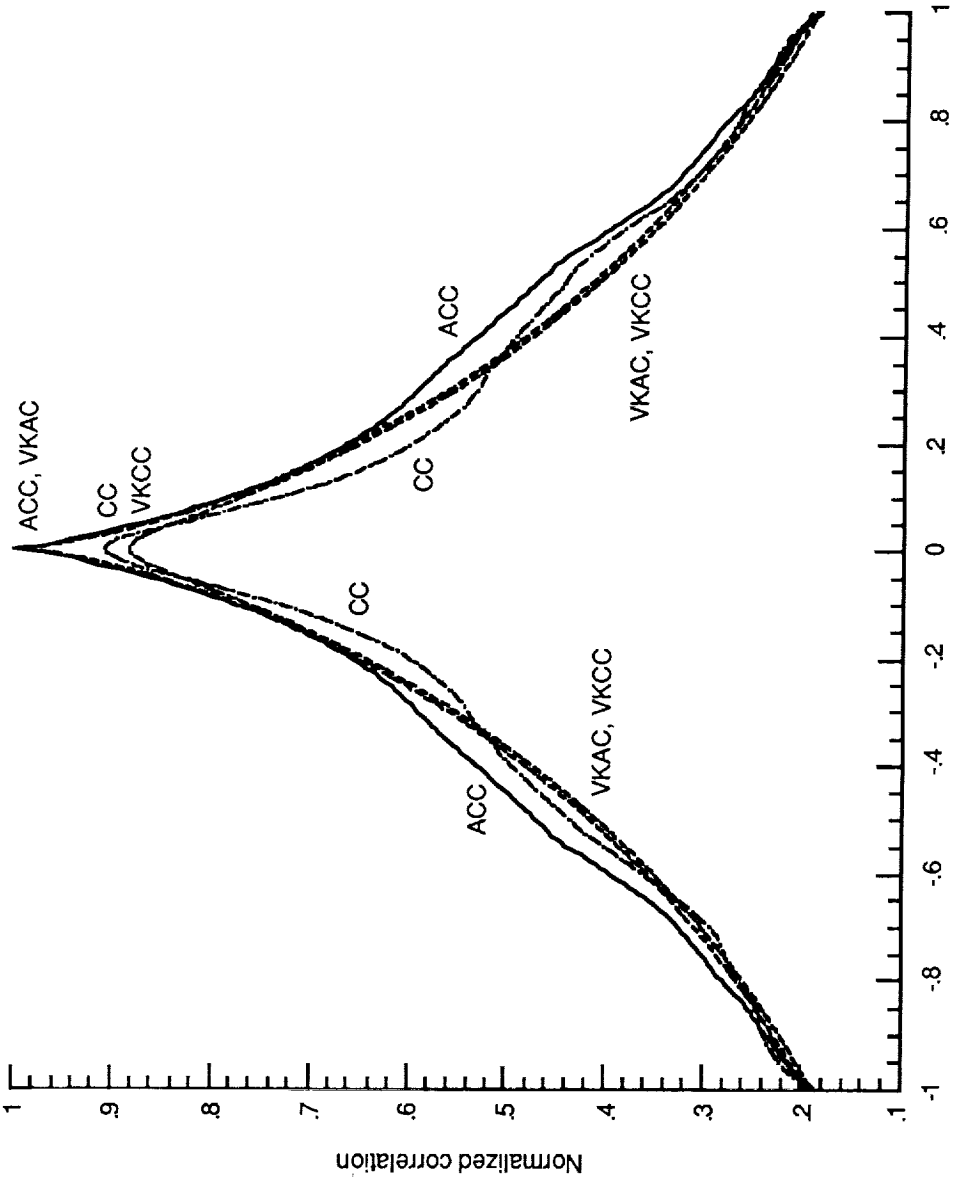

(b) Enlarged view of correlation estimates and functions.

Figure 25. Concluded.

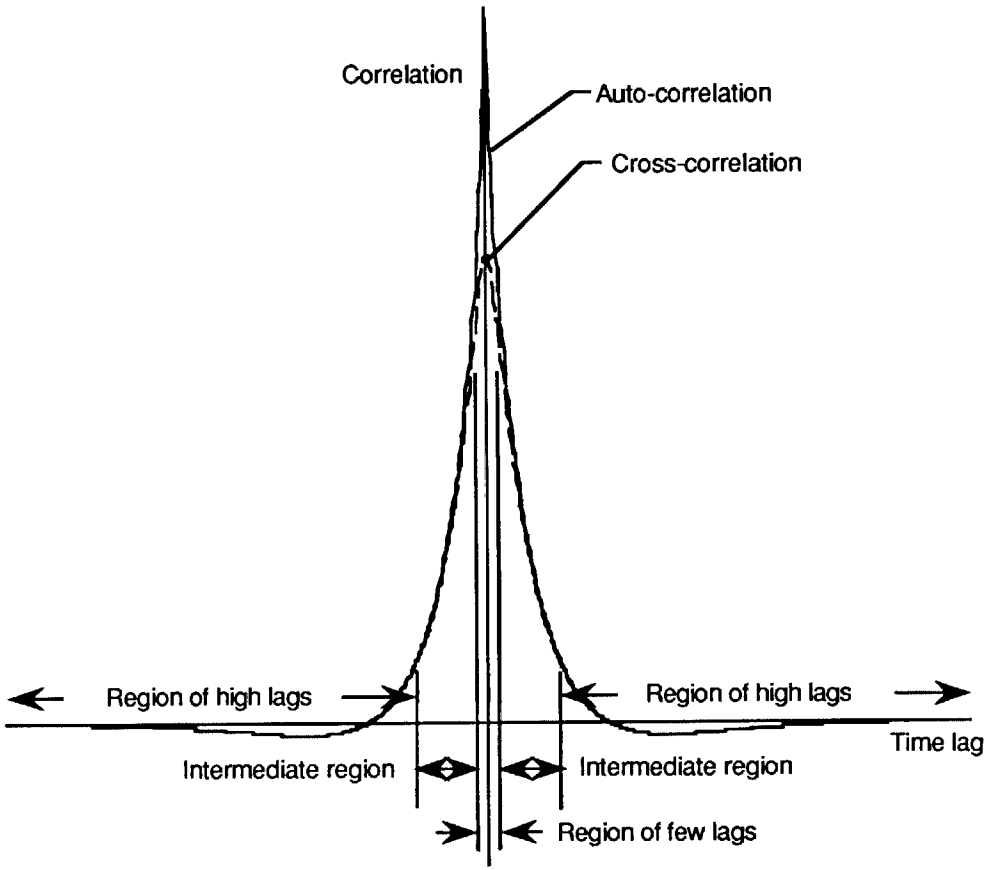

Figure 26. Regions of correlation characteristics used for matching to experiment.

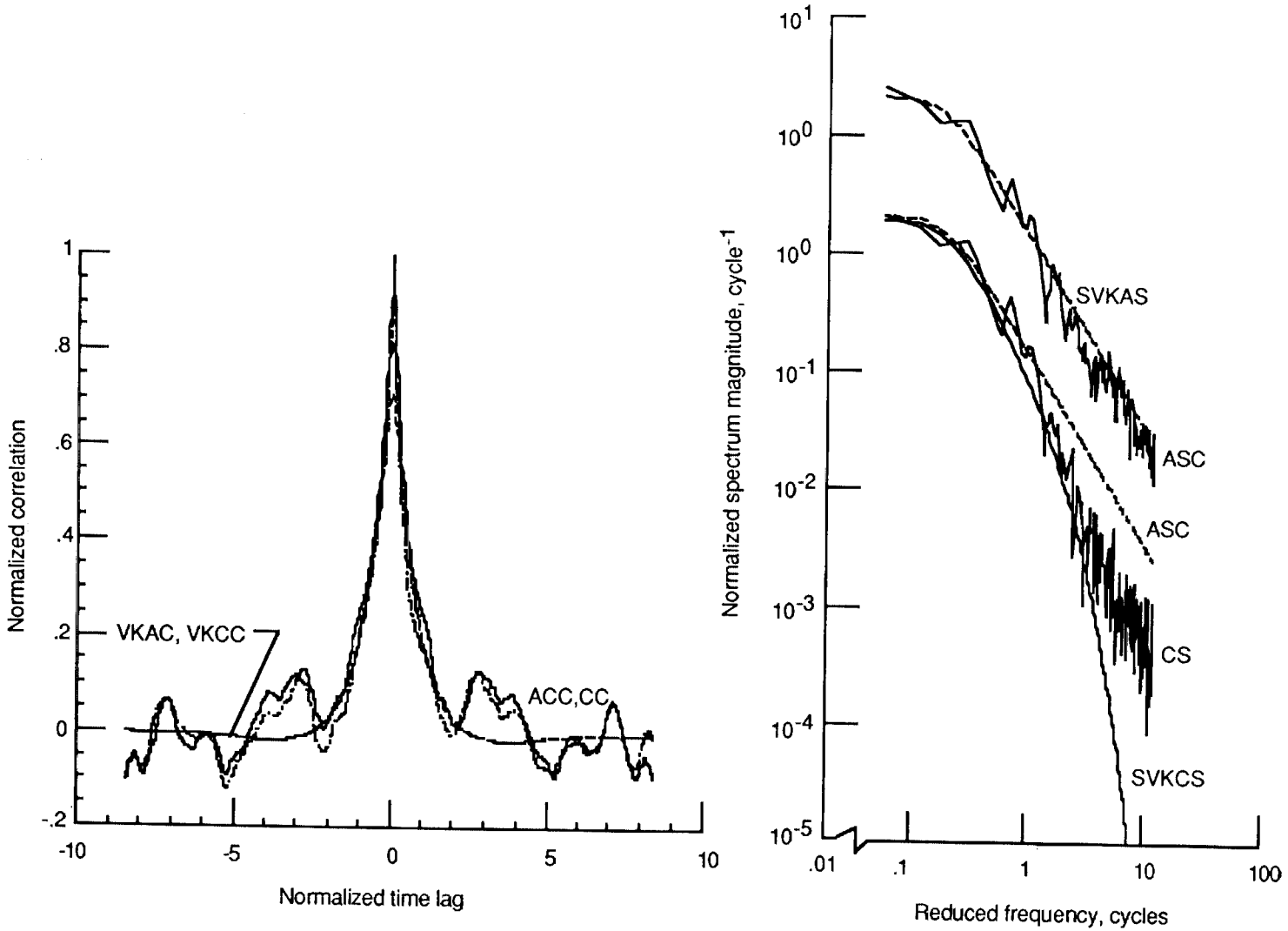

Figure 27. Spectral estimates and functions of correlations and spectrum magnitudes for run 2619 with sample rate of 200 sps.

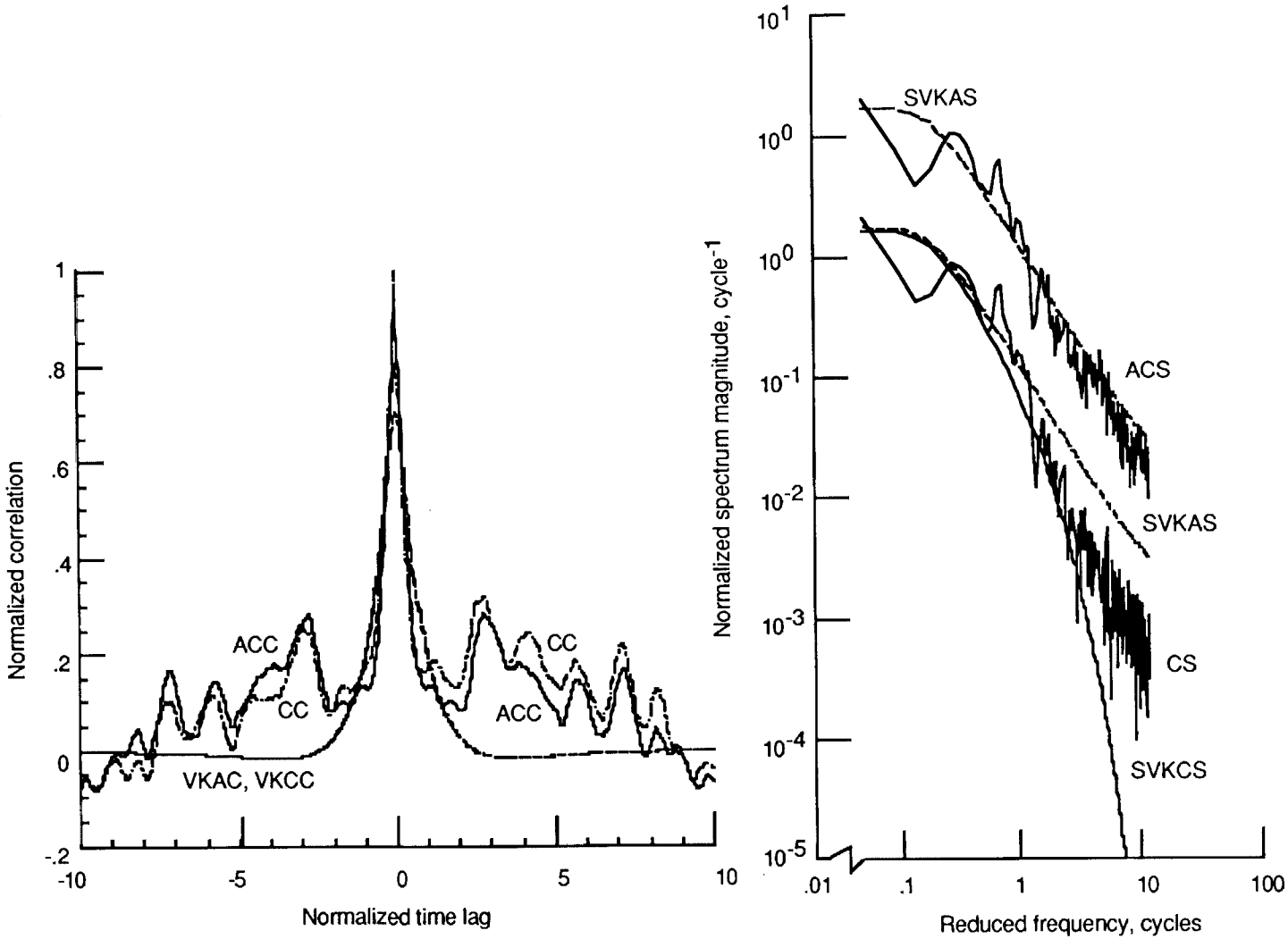

Figure 28. Correlation and spectrum magnitude estimates for synthesized angle-of-attack component of vertical gust velocity for run 2619.

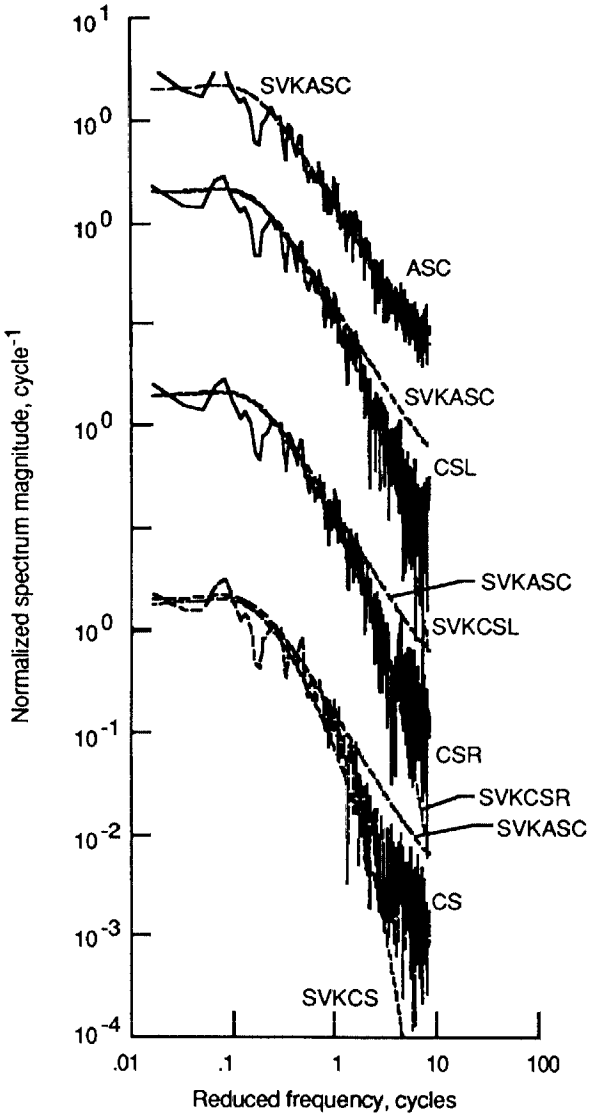

(a) For 1023 lags.

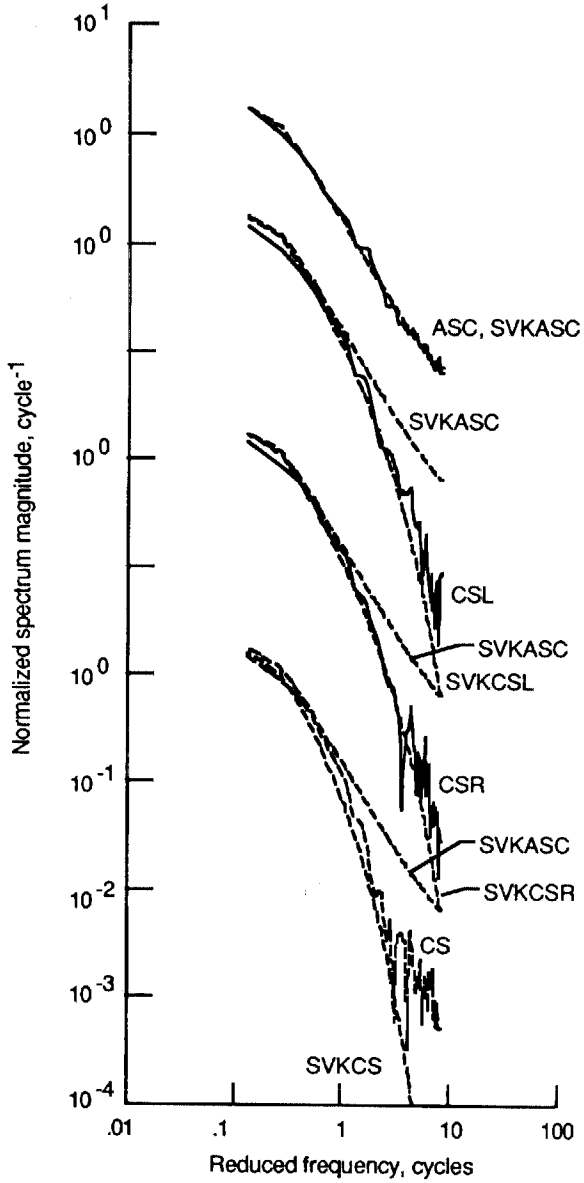

(b) For 127 lags.

Figure 29. Center spectra and correlation estimates and cross-spectrum magnitude estimates across wing span and semispans for run 7105.

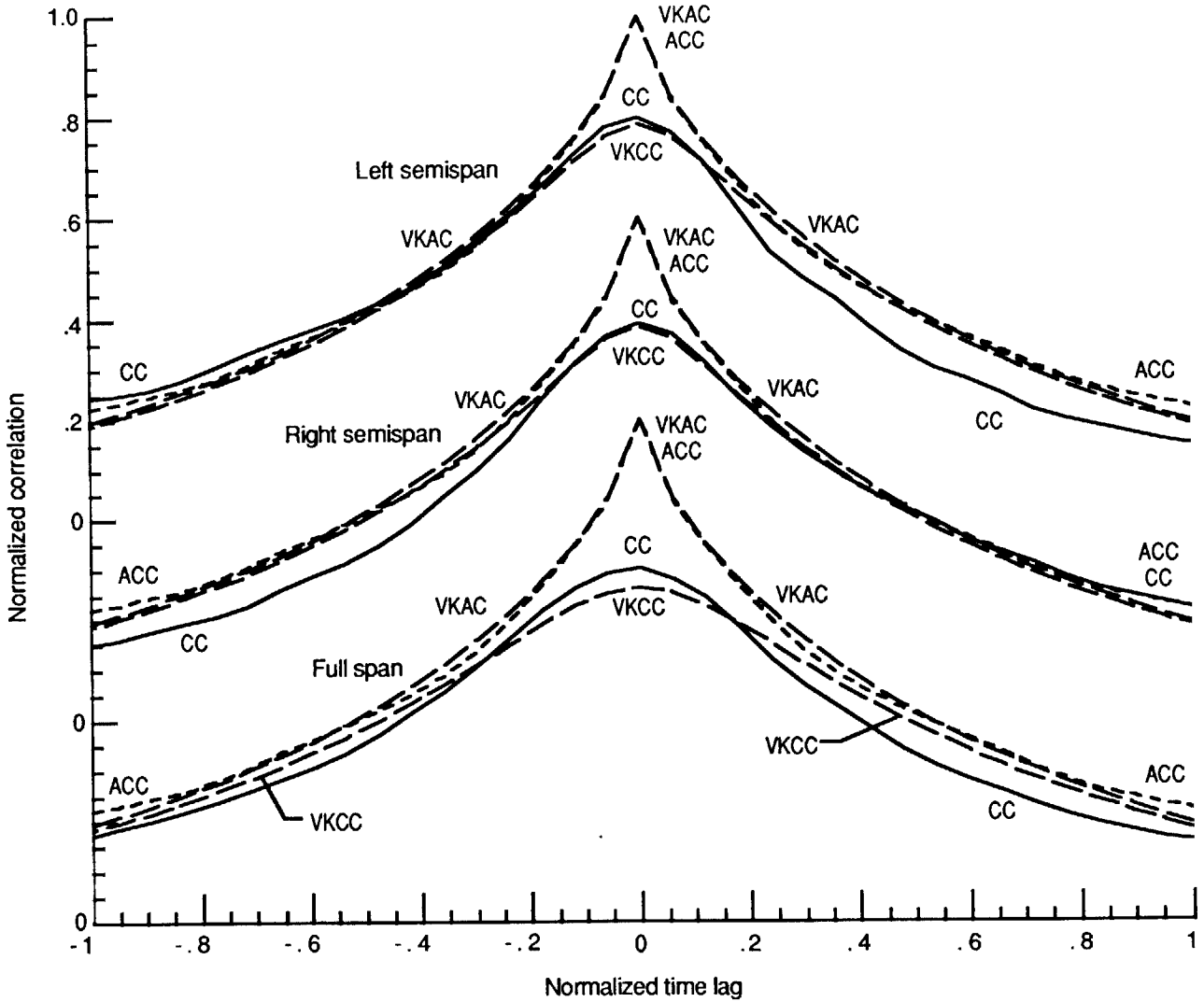

(c) Enlarged view of auto- and cross-correlation estimates and functions.

Figure 29. Concluded.

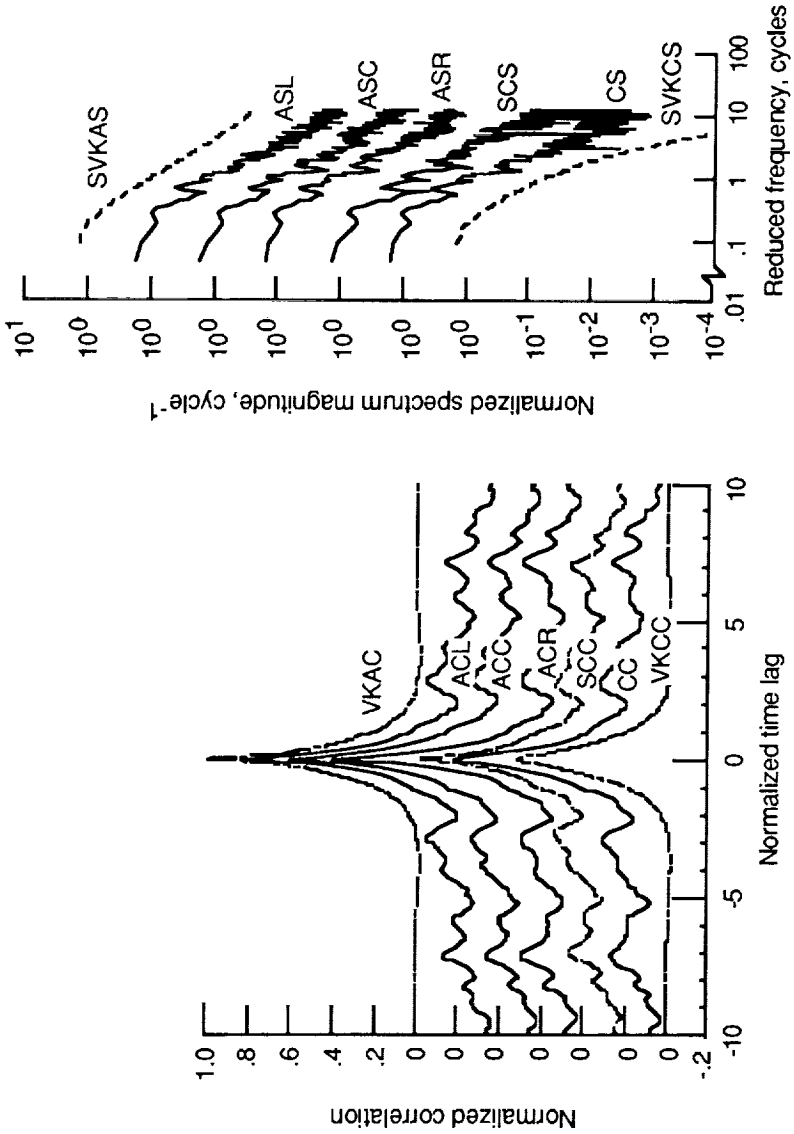

Figure 30. Measured estimates and theoretical functions of correlations and spectrum magnitudes for run 2619.

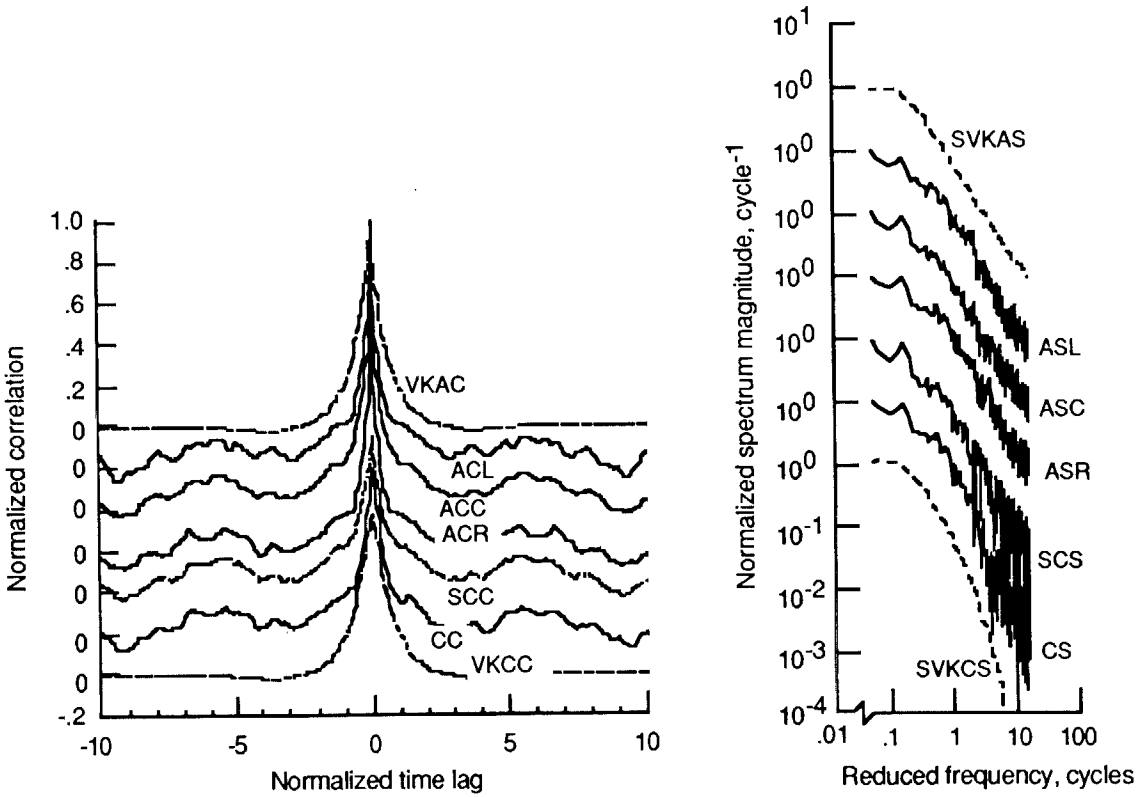

Figure 31. Measured estimates and theoretical functions of correlations and spectrum magnitudes for run 3113.

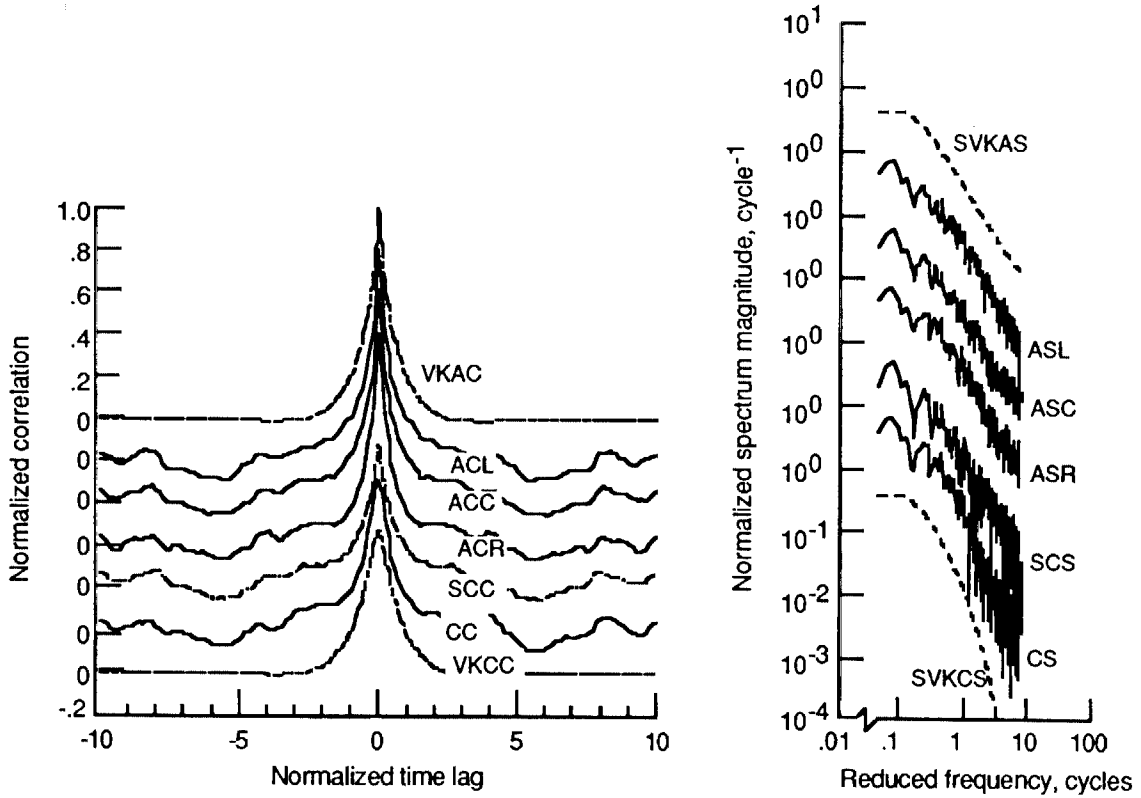

Figure 32. Measured estimates and theoretical functions of correlations and spectrum magnitudes for run 7105.

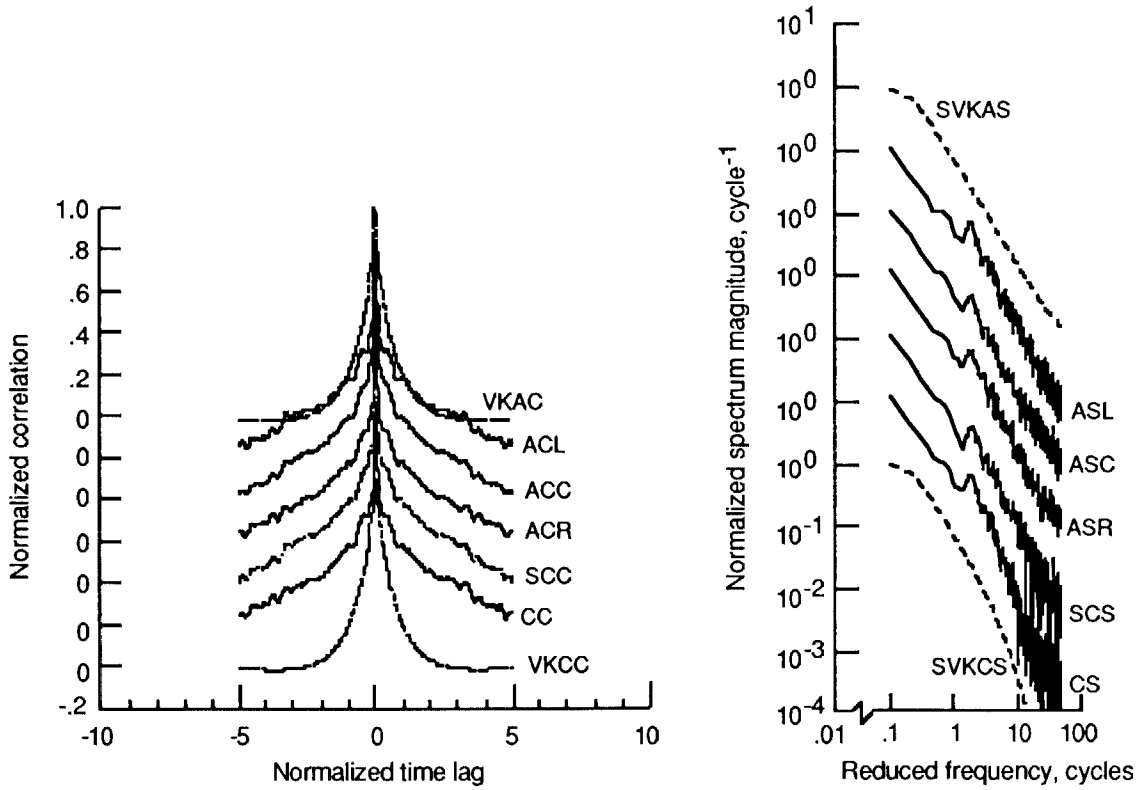

Figure 33. Measured estimates and theoretical functions of correlations and spectrum magnitudes for run 7108.

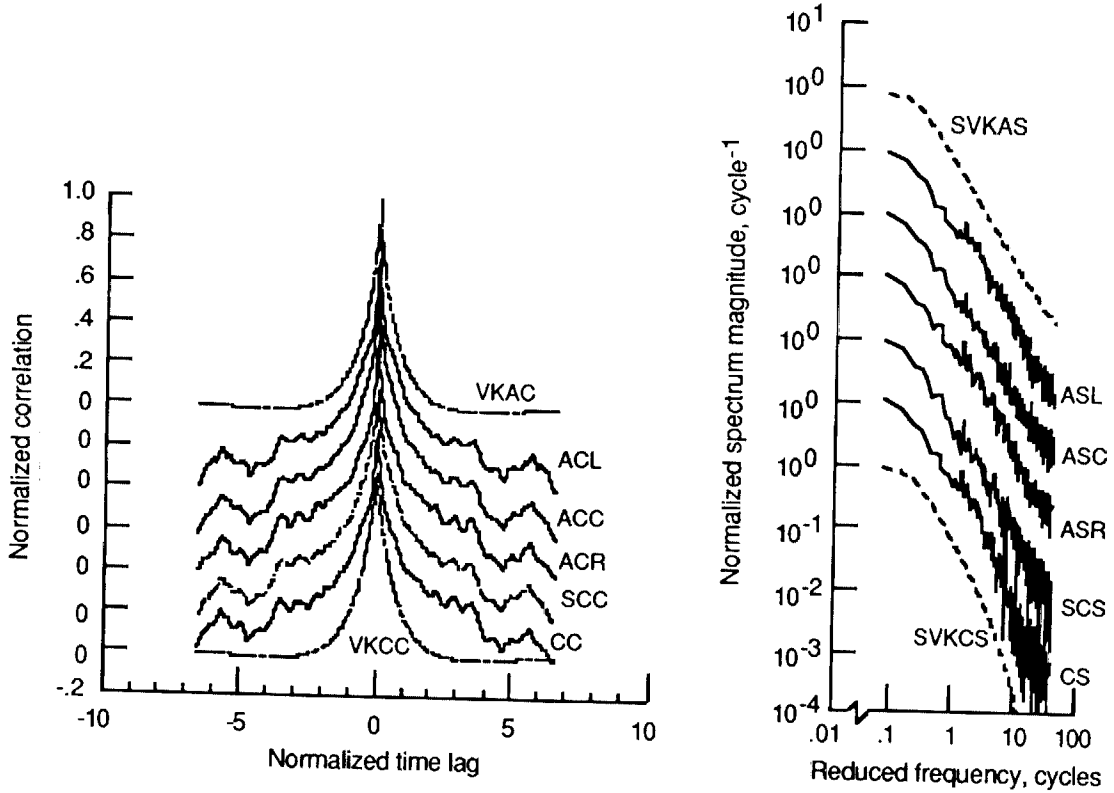

Figure 34. Measured estimates and theoretical functions of correlations and spectrum magnitudes for run 7109.

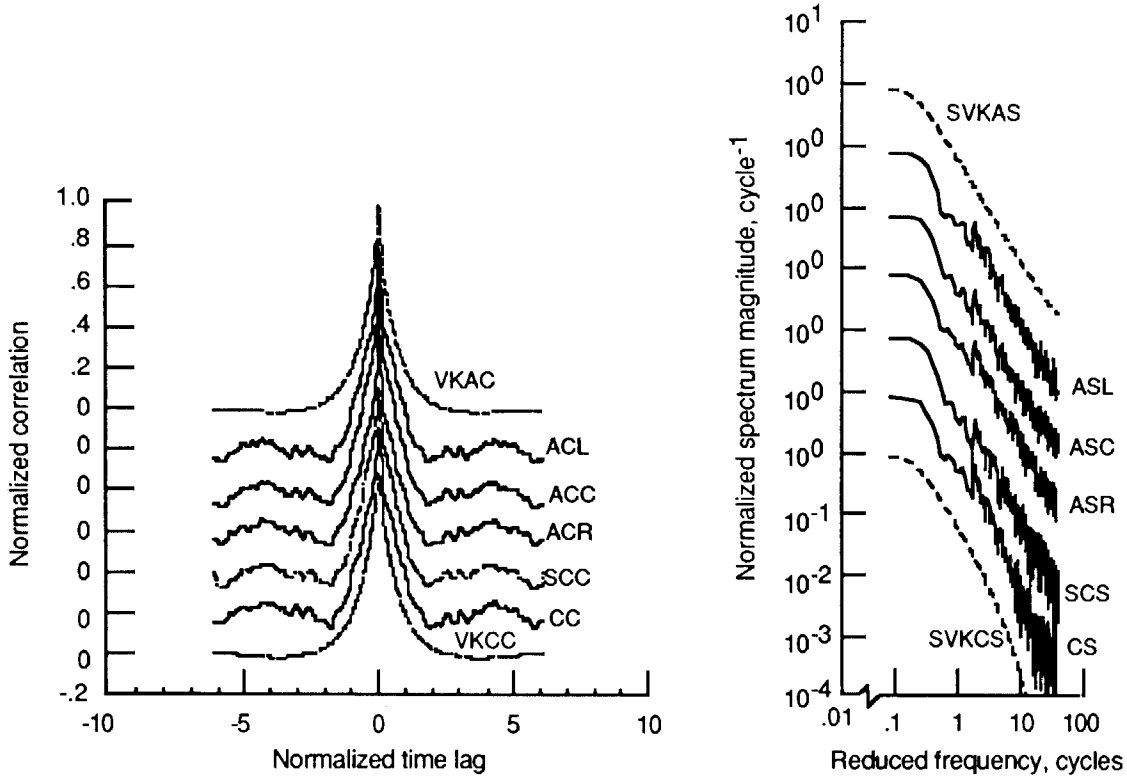

Figure 35. Measured estimates and theoretical functions of correlations and spectrum magnitudes for run 7111.

NASA
National Aeronautics and Space Administration

Report Documentation Page

1. Report No.	2. Government Accession No.	3. Recipient's Catalog No.
NASA TP-2963		

4. Title and Subtitle	5. Report Date
Spanwise Measurements of Vertical Components of Atmospheric Turbulence	April 1990
	6. Performing Organization Code
7. Author(s)	8. Performing Organization Report No.
Robert K. Sleeper	L-16550
9. Performing Organization Name and Address	10. Work Unit No.
NASA Langley Research Center Hampton, VA 23665-5225	505-63-21-04
	11. Contract or Grant No.
12. Sponsoring Agency Name and Address	13. Type of Report and Period Covered
National Aeronautics and Space Administration Washington, DC 20546-0001	Technical Paper
	14. Sponsoring Agency Code

15. Supplementary Notes

16. Abstract

Correlation and spectrum magnitude estimates are computed for vertical gust velocity measurements at the nose and wingtips of the NASA B-57B airplane for six level-flight, low-speed, and low-altitude runs and are compared with those of the Von Kármán atmospheric turbulence model extended for spanwise relationships. The distance between the wingtips was 62.6 ft. Airspeeds ranged from about 330 to 400 ft/sec, heights above the ground ranged from near ground level to about 5250 ft, and gust velocity standard deviations ranged from 4.10 to 8.86 ft/sec. Integral scale lengths, determined by matching measured auto-correlation estimates with those of the model, ranged from 410 to 2050 ft. Digital signals derived from piezoelectric sensors provided continuous pressure and airspeed measurements. Some directional acceleration sensitivity of the sensors was eliminated by sensor orientation, and their performance was spectrally verified for the higher frequencies with supplemental onboard piezoresistive sensors. The model appeared to satisfactorily predict the trends of the measured cross-correlations and cross-spectrum magnitudes, particularly between the nose and wingtips. However, the measured magnitude estimates of the cross-spectra between the wingtips exceeded the predicted levels at the higher frequencies. Causes for the additional power across the wingtips were investigated. Vertical gust velocity components evaluated along and lateral to the flight path implied that the frozen-turbulence-field assumption is a suitable approximation.

17. Key Words (Suggested by Authors(s))	18. Distribution Statement
Atmospheric turbulence Auto- and cross-correlations Auto- and cross-spectra	Unclassified—Unlimited Subject Category 47

19. Security Classif. (of this report)	20. Security Classif. (of this page)	21. No. of Pages	22. Price
Unclassified	Unclassified	66	A04

NASA FORM 1626 OCT 86

NASA-Langley, 1990

For sale by the National Technical Information Service, Springfield, Virginia 22161-2171